Max-Planck-Institut für Meteorologie
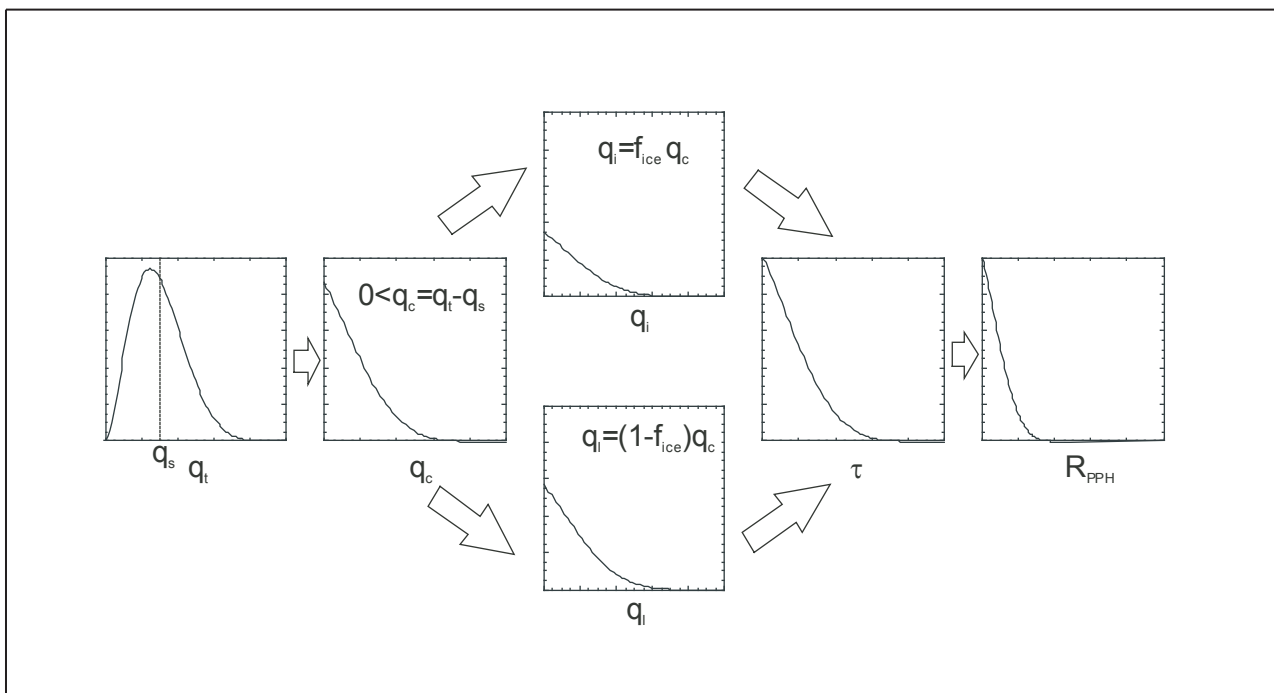*Max Planck Institute for Meteorology*

Examensarbeit Nr. 89

Influence of Sub-Grid Scale Variability of Clouds on the Solar
Radiative Transfer Computations in the ECHAM5 Climate Model

von

Georg Bäuml

Hamburg, Dezember 2002

Dissertation zur Erlangung des Doktorgrades

Autor:

Georg Bäuml   Max-Planck-Institut für Meteorologie

Max-Planck-Institut für Meteorologie
Bundesstrasse 55
D - 20146 Hamburg
Germany

Tel.:   +49-(0)40-4 11 73-0
Fax: +49-(0)40-4 11 73-298
e-mail: <name>@dkrz.de
Web: www.mpimet.mpg.de

Influence of the Sub-Grid Scale Variability of Clouds
on the Solar Radiative Transfer Computations
in the ECHAM5 Climate Model

Dissertation

zur Erlangung des Doktorgrades

der Naturwissenschaften im Fachbereich

Geowissenschaften

der Universität Hamburg

vorgelegt von

Georg Bäuml

aus

Neustadt an der Waldnaab

Hamburg

2002

Als Dissertation angenommen
vom Fachbereich Geowissenschaften der Universität Hamburg
auf Grund der Gutachten von Herrn Dr. Erich Roeckner
und Herrn Prof. Dr. Hartmut Graßl

Hamburg, den 9. Dezember 2002

Prof. Dr. U. Bismayer

Dekan

des Fachbereichs Geowissenschaften

Abstract

Most numerical climate models use the plane parallel homogeneous (PPH) approximation when computing the interactions of radiation and clouds. The latter actually means that clouds are seen as boxes stretching over the complete vertical extension of a model layer and horizontally cover an area according to their cloud fraction. Ice and liquid water content within the cloud are constant. This is of course in contrast to real clouds revealing structures on scales much smaller than the typical grid size of a climate model. It can be shown that neglecting this sub-grid scale variability leads to a systematic error, such that the reflectivity (transmissivity) of clouds is overestimated (underestimated). This is called PPH-bias.

Two different correction approaches are tested in this study: The effective thickness approach (ETA) and the statistical approach of weighted two-stream approximation. In the former, empirical reduction factors $\chi < 1$ are determined such that the effective optical thickness of clouds becomes $\tau_{\mathrm{eff}} = \chi\overline{\tau}$, where $\overline{\tau}$ is the mean cloud optical thickness in a single level of a model grid cell. When the sub-grid scale statistics of the distributions of cloud liquid and ice water and therefrom of optical thickness are known, expressed by the probability distribution function $p(\tau)$, the reflectivities and transmissivities may be computed by weighting the standard two-stream formulas with p. When this approach is to be applied to multiple layers, one has to account for the correlation of the PDFs in adjacent layers.

In order to test the correction approaches, spatially highly resolved data from two large eddy simulations are used: A nocturnal stratocumulus and a shallow trade wind cumulus. By taking the independent column approximation (ICA) as reference and comparing the ICA fluxes to the PPH analogues, the PPH-bias can clearly be identified. It is relatively small for the stratus cloud ($\sim 5\%$), while it is tremendous for the trade wind cumulus (up to 100%). The ETA shows good agreement with the ICA calculation with $\chi = 0.9$ for the stratus cloud and $\chi = 0.4$ for the trade wind cumulus. Clearly, the reduction factor is no unique constant, but rather crucially depends on the cloud type and thus variability. For the statistical approach, Gamma distributions are fitted to the cloud data and the

Gamma-weighted two-stream approximation is applied. In both cloud cases, the GWTSA including a correlation correction remarkably underestimates the reflectivity. This is in contrast to other studies and is likely to be due to misfits of the distributions in the small model domains. The effect of correlation is of similar order as purely weighting the two-stream functions with the PDF.

Finally, the two correction approaches are also implemented into the ECHAM5 climate model. The ETA is realized in various fashions: using a single reduction factor $\chi = 0.7$ for all clouds or only for liquid clouds, while ice clouds remain unchanged, applying $\chi_{\text{conv}} = 0.4$ to convective clouds and $\chi = 0.9$ to stratiform clouds and disinguishing between ice clouds ($\chi_{\text{ice}} = 0.9$) and liquid clouds ($0.4 \leq \chi_{\text{liq}} \leq 1.$, depending on liquid water path), where thick clouds are assumed to be more variable and thus a smaller reduction factor has to be used. The latter is the standard scheme of the ECHAM5 model. A statistical approach is realized as a Beta-weighted two-stream approximation (BWTSA), making use of the Beta-shaped distribution of total water mixing ratio as it is supplied by the cloud cover scheme. The effect of correlation is not accounted for. Comparing the various schemes, one can identify the huge impact of ice clouds, when a small reduction factor as $\chi = 0.7$ is applied to them. Their influence is remarkably reduced by using $\chi = 0.9$, as it has been deduced empirically. The albedo correction patterns of the BWTSA and the ECHAM5 standard ETA are very similar, but the BWTSA corrections are only half that of this ETA variant. Including the correlation effect into the BWTSA will increase the corresponding corrections, but is unlikely to reach the values of the ETA. Due to the lack of suitable observational data, the albedo corrections cannot be validated yet. It should be noted that the BWTSA does not introduce any empirical parameterizations like the distinction between ice and liquid clouds in the ETA, but treats clouds consistently with the cloud cover scheme.

Contents

Acronyms

AGCM	Atmospheric General Circulation Model
ANN	annual
ASTEX	Atlantic Stratocumulus Transition Experiment
ATEX	Atlantic Trade Wind Experiment
BWTSA	Beta Weighted Two-Stream Approximation
BS	Bäuml Scaling — experiment identifier (see Table 5.3)
BW	Beta Weighted — experiment identifier (see Table 5.6)
CAPE	Convective Available Potential Energy
CFC	Chlorofluorocarbons
CK	Changed K — experiment identifier (see Table 5.6)
CRF	Cloud Radiative Forcing
CRM	Cloud Resolving Model
CS	Cahalan Scaling — experiment identifier (see Table 5.3)
DJF	December–January–February
DS	— experiment identifier (see Table 5.6)
ECHAM	European Centre Hamburg Model
ECMWF	European Centre for Medium Range Weather Forecasting
EHCA	Equivalent Homogeneous Cloud Approximation
ERBE	Earth Radiation Budget Experiment
ETA	Effective Thickness Approximation
EUCREM	European Cloud-Resolving Modelling
FT	Fixed Time — experiment identifier (see Table 5.6)
GCM	General Circulation Model
GCSS-WG1	GEWEX Cloud System Studies Working Group 1
GEWEX	Global Water and Energy Experiment
GWRT	Gamma Weighted Radiative Transfer Scheme
GWTSA	Gamma Weighted Two-Stream Approximation
HR	High Resolution — experiment identifier (see Table 5.6)

ICA	Independent Column Approximation
IPA	Independent Pixel Approximation
IPCC	Intergovernmental Panel on Climate Change
ISCCP	International Satellite Cloud Climatology Project
ITCZ	Inter Tropical Convergence Zone
IWC	Ice Water Content
IWP	Ice Water Path
JJA	June–July–August
LW	longwave
LWC	Liquid Water Content
LWP	Liquid Water Path
LES	Large Eddy Simulation
MAM	March–April–May
MLE	Maximum Likelihood Estimate
MOM	Method of Moments
NIPA	non-local Independent Pixel Approximation
NO	no correction — experiment identifier (see Table 5.3)
OLR	Outgoing Longwave Radiation
PDF	Probability Distribution Function
PPH	Plane Parallel Homogenous
TOA	Top of the Atmosphere
RS	Roeckner Scaling — experiment identifier (see Table 5.3)
SHDOM	Spherical Harmonics Discrete Ordinate Model
SON	September–October–November
SPCZ	South Pacific Convergence Zone
SW	shortwave
TS	Tiedtke Scaling — experiment identifier (see Table 5.3)

Chapter 1

Introduction

Solar radiation reaching the earth is the major energy source for the climate system. Part of it gets reflected back to space, the remainder is absorbed within the atmosphere or at the surface. At the same time the earth emits thermal radiation according to its blackbody temperature, thus balancing the global energy budget. The net energy gain is temporally and spatially highly variable with large input in the tropics and losses in the polar regions. General circulation redistributes the energy. Figure 1.1 gives an overview of the global mean values of the various energy fluxes involved. Clouds play a dominant role, both for the hydrological cycle (and the connected fluxes of latent heat) and by modulating the radiative transfer: In the solar spectral range by reflecting and absorbing the incoming light, and in the thermal range by changing the emission temperature according to the cloud's emissivity and temperature (see e.g. Ramanathan et al., 1989; Hartmann, 2002; Wielicki et al., 2002). The importance of the cloud-radiative interaction and the need for improving our knowledge of these processes have been underlined by the Intergovernmental Panel on Climate Change in its previous report: "The main uncertainties in climate model simulations arise from the difficulties in adequately representing clouds and their radiative properties..." (Houghton et al., 1996).

Currently most climate models predict the cloud water content and the fractional cloud cover for each grid cell. For a typical model resolution these cells span some $100 \times 100 \, \text{km}^2$ in the horizontal, while the vertical extent is of the order of a few $100 \, \text{m}$ (Roeckner et al., 1996; McFarlane et al., 1992). The interaction of radiation with clouds is computed by treating the clouds as homogeneous boxes, that vertically extend over the height of the grid cell, and horizontally cover a fractional area of the cell. The cloud condensate is distributed uniformly within this box. This is called the *plane parallel homogenous (PPH)* approximation. Cloud albedo is a convex function of optical thickness, which in turn depends on cloud water amount (cf. Figure 1.2). Thus, given a constant increment in optical thickness, the change in albedo is larger for thin clouds than for thick clouds (Pincus et al., 1999). This means a model grid cell exhibiting any internal horizontal
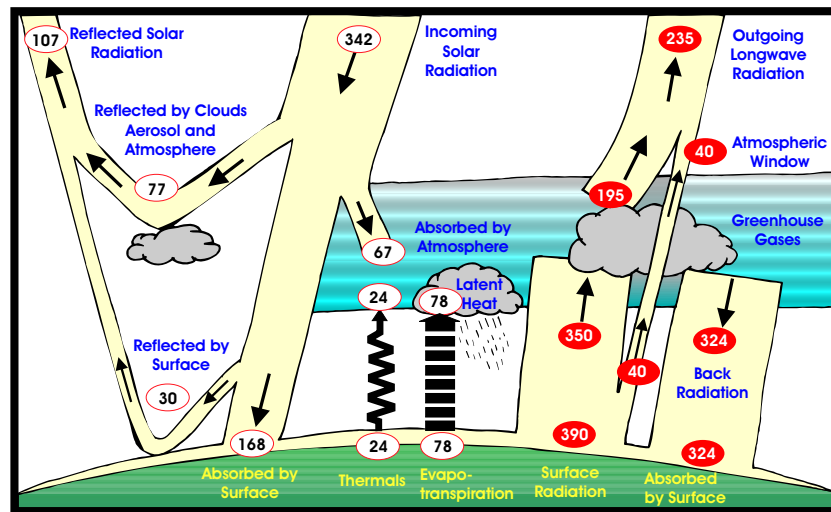
Figure 1.1: Observed annual global energy budget. (Adapted from Kiehl and Trenberth (1997))

variability within its cloudy part will always be less reflective than a uniform grid cell of the same average optical thickness. This follows from Jensen's inequality (Jensen, 1906). The systematic overestimation of the cloud albedo by models using the PPH assumption is called *PPH-bias*. It is sketched in Figure 1.2 for the simple example of two realizations of a cloud with mean optical thickness $\overline{\tau}$: The solid lines mark the albedo one obtains for a uniform cloud with $\tau \equiv \overline{\tau}$, whereas the dashed lines correspond to a cloud that has $\tau = \tau_1$ and $\tau = \tau_2$ for the two halfs. Both yield the same mean optical thickness value $\overline{\tau} = (\tau_1 + \tau_2)/2$. The average albedo value $\overline{R} = (R(\tau_1) + R(\tau_2))/2$ is smaller than the reflectivity for the uniform cloud $R(\overline{\tau})$. Generally, all physical parameterizations (like many cloud microphysical processes) that depend non-linearly on a property exhibiting sub-grid scale variability are prone to such systematic biases (Pincus and Klein, 2000).

The albedo problem has already been recognized by Harshvardhan and Randall (1985), and Stephens (1985), and has been investigated theoretically (Stephens, 1988b,a), describing the so called "albedo paradox" (Wiscombe et al., 1984). Stated simply, the albedo
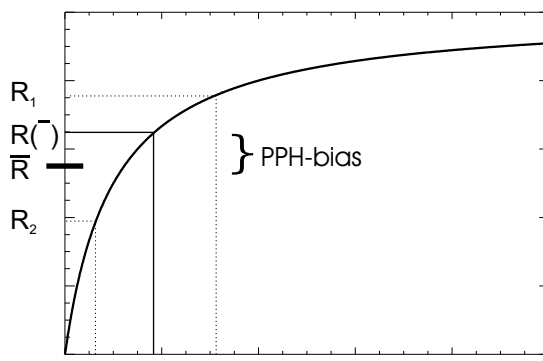

Figure 1.2: Cloud reflectivity as a function of cloud optical thickness. The solid and dashed lines show the derivation of reflectivity for a uniform and an inhomogeneous cloud, respectively.

paradox refers to the observation that optical depths computed from seemingly reasonable liquid water profiles turn out to be larger than those, deduced from the observed global albedo and cloud fraction — the simulated albedo is too high. From satellite measurements (e.g. Oreopoulos and Davies, 1998a,b) and cloud model data (e.g. Cahalan et al., 1994; Davis et al., 1990) the PPH-bias has been quantified to result in a relative error of up to $\sim 15\%$.

The radiative balance determines the global mean temperature. Proper simulation of the planetary albedo and thermal emission is therefore crucial for climate models, and is achieved by tuning the cloud parameterizations such that the radiative fluxes at the top of the atmosphere (TOA) are in agreement with satellite data. This implies that any error in the radiative transfer computation is artificially balanced by introducing compensating errors in other model components. Remote sensing faces the same problem: Errors in modeling the cloud-radiation interactions result in erroneously derived cloud properties. The PPH-bias leads to an underestimated liquid water path (Chambers et al., 2001). Various studies have been conducted in order to quantify and correct for the deviations due to cloud variability (Chambers et al., 1997; von Bremen, 2001).

For climate models two main correction approaches have evolved:

- Defining an effective optical thickness, which is smaller than the true mean optical thickness in a given model grid box and thus balances the overestimation of reflectivity (Cahalan et al., 1994).

- Determining the probability distribution function of optical thickness from satellite data (Oreopoulos and Davies, 1998b) or cloud resolving model data (Tompkins, 2002) and using this information for computing the reflectivity (Barker, 1996; Barker et al., 1996).

This study evaluates these two methods:

1. The applicability of both methods is tested for cloud data from a cloud resolving model and parameter settings are derived to be used in a climate model.

2. Several realizations of the two correction approaches are implemented into the climate model *ECHAM5* and are compared to each other and to the PPH computations. For the first time sub-grid scale statistical information about cloud variability, prognosed by the cloud parameterization package, is used consistently in the radiation scheme.

Chapter 2 gives an introduction to the radiative transfer problem and introduces the approximations used in climate modeling, emphasizing the scheme implemented in the ECHAM5 model. The approaches for correcting the PPH-bias are derived in Chapter 3. In Chapter 4 the results for the cloud resolving model data are described. They are used to develop various parameterizations for the climate model. These are presented in Chapter 5.

Chapter 2

Shortwave Radiative Transfer Computation

Understanding the transfer of radiation through the atmosphere (both for cloudy and clear sky conditions) is of great importance for modeling the climate. Also, remote sensing of atmospheric profiles as well as of celestial objects relies crucially on understanding the processes of scattering, absorption and, in the case of thermal radiation, emission. A huge variety of different approaches to deal with the radiative transfer problem exist, because of the different needs in efficiency and accuracy (see e.g. Liou, 1980; Lenoble, 1985; Goody and Yung, 1989). In this chapter some theoretical background will be provided by introducing the transfer problem and its general solution. We will then focus on a widely used approximation, the so called two-stream approximation, which is also implemented in the radiation scheme of the ECHAM5 climate model. Finally some methods for investigating the radiative properties of high spatial resolution cloud data are explained, stressing the various assumptions made and their limits.

2.1   Theoretical Background

There are two contributions to the extinction of solar radiation on its way through the atmosphere: scattering and absorption. Here we will formulate the basic equations of the transfer problem and sketch approximations for the scattering part (two-stream and Eddington approximation) and the absorption part (distribution of photon path length and absorber amount). The two processes are strongly interconnected, since for the shortwave part of the spectrum, scattering and absorption occur simultaneously. For example, the particles in a smoke plume absorb part of the incident radiation, but they also enhance scattering and thereby lengthen the mean path a photon travels through the plume, which in turn results in increased absorption.
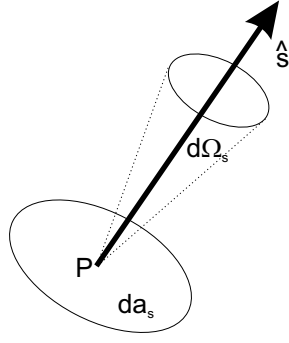
Figure 2.1: Sketch for definition of radiance.

First, a few basic radiative properties will be defined (see e.g. Goody and Yung, 1989) together with the symbols that will be used throughout this work.

Radiance: Let P be a point and da_s be a piece of area perpendicular to the direction $\hat{s}$ around P (cf. Figure 2.1). The bundle of rays originating from da_s, and contained within the solid angle $d\Omega_s$ in the direction of $\hat{s}$, transport in a time dt and in a frequency range $[\nu, \nu + d\nu]$, the energy

$$E_\nu = L_\nu(P, \hat{s})\, da_s\, d\Omega_s\, d\nu\, dt, \tag{2.1}$$

where $L_\nu(P, \hat{s})$ is the *specific intensity of radiation* or *radiance*, i.e. the flux of energy in a given direction per unit time per unit frequency range per unit solid angle per unit area perpendicular to the given direction $\hat{s}$. The intensity I is the integral over a piece of solid angle

$$I_\nu(P, \hat{s}) = \int_\Omega L_\nu\, d\Omega_s. \tag{2.2}$$

Flux: The flux in direction $\hat{d}$ at point P is defined as the total energy flowing across a unit area perpendicular to $\hat{d}$ per unit frequency interval,

$$F_{\nu,\hat{d}}(P) = \int_{\Omega_s} L_\nu(P, \hat{s}) \cos(\hat{d}, \hat{s})\, d\Omega_s. \tag{2.3}$$

(Mass) extinction coefficient: The attenuation of a ray traveling a distance ds through a homogeneous medium of density ρ and *spectral extinction coefficient* k_ν is given by

$$dL_\nu = -L_\nu k_\nu \rho\, ds. \tag{2.4}$$

Extinction is caused by the two processes *scattering* and *absorption*, with $k_\nu = k_{s\nu} + k_{a\nu}$, where $k_{s\nu}$ and $k_{a\nu}$ are the scattering and absorption coefficients, respectively. The absorption coefficient depends on temperature and pressure, according to the modifications of the molecular vibration and rotation frequencies. In the following, we will omit the index ν.

Extinction cross section: The *extinction cross section* or *molecular extinction coefficient* is defined as
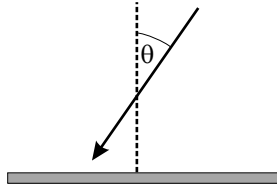
$$\sigma = k\rho_m, \tag{2.5}$$

Figure 2.2: Definition of the zenith angle θ.

with ρ_m the molecular density. It has the units of area and it conveys a valuable picture of the extinction process in terms of the collision cross section between a photon and a single absorbing molecule. Analogously, cross sections for the individual extinction processes scattering (σ_s) and absorption (σ_a) may be defined.

Single scattering albedo: The ratio of the scattering cross section σ_s to the extinction (scattering plus absorption) cross section σ is called *single scattering albedo*

$$\tilde{\omega} = \frac{\sigma_s}{\sigma_s + \sigma_a}. \tag{2.6}$$

It describes the fraction of the total extinction caused by scattering. Hence, $\tilde{\omega} = 1$ means conservative scattering, where nothing is absorbed and the energy remains completely in the radiation field.

Optical thickness: For a layer of density ρ the *optical thickness* between two points 1 and 2 is defined as

$$\tau(1,2) = \int_1^2 k\rho \, ds \tag{2.7}$$

Most often τ stands for the optical thickness along a specific path, namely along the z–direction, thus,

$$\tau = \int_z^{z_{\text{TOA}}} k(z')\rho(z') \, dz'. \tag{2.8}$$

Since k is a function of pressure and temperature, which in turn vary with height, it can be expressed as a function of z. The above definition is also called *normal optical depth*. The latter may serve as the vertical coordinate instead of z.

Solar zenith angle: The angle θ of a ray relative to the zenith direction is called *zenith angle* (see Figure 2.2). Important for the transfer computations is the cosine of the zenith angle, which is abbreviated by

$$\mu = \cos\theta. \tag{2.9}$$

The cosine of the *solar zenith angle* of the incident solar radiation is denoted by μ_0. The term solar zenith angle is often used for both, the angle itself and its cosine.

Figure 2.3: Scattering geometry: Incident beam with direction (μ', ϕ') gets scattered into the new direction (μ, ϕ). Θ is the scattering angle between the incoming and outgoing beam.
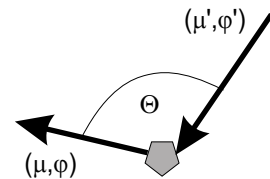
Scattering phase function: Scattering of radiation by a particle may be described by the *scattering phase function* $P(\mu, \phi; \mu', \phi')$, which gives the fraction of radiation coming from direction (μ', ϕ') being scattered into the direction (μ, ϕ), as sketched in Figure 2.3. It fulfills the norm

$$\frac{1}{4\pi} \int_0^{2\pi} \int_{-1}^1 P(\mu, \phi; \mu', \phi') \, d\mu' \, d\phi' = 1. \tag{2.10}$$

The direction of the fluxes are given with their zenith and azimuth angles (μ, ϕ). Downward directions are indicated by negative μ.

2.1.1   Radiative Transfer Equation

According to the definitions made above, for downward radiation $\mu < 0$ and $d\tau > 0$ (cf. (2.8)) and correspondingly $\mu > 0$ and $d\tau < 0$ for upward radiation. Here we use the normal optical thickness as the vertical coordinate, taking advantage of (2.8). The general radiative transfer equation in its differential form may then be written as

$$\mu \frac{dL(\tau, \mu, \phi)}{d\tau} = L(\tau, \mu, \phi) - J(\tau, \mu, \phi), \tag{2.11}$$

where L is the radiance and J the source function. The latter has three contributions $J = J_{em} + J_{abs} + J_{scatt}$, namely emission ($> 0$), absorption ($< 0$) and scattering (both signs possible). Due to the low surface temperature of the earth compared to that of the sun and considering Wien's law we can neglect the thermal emission of radiation by the earth and atmosphere for the solar spectrum.

We will now first examine the most important part of J, the scattering. The latter may be divided into two components, which stem from multiple scattering of diffuse radiation and the single scattering of the direct solar beam, respectively, such that $J_{scatt} = J_{diff} + J_{dir}$. In the diffuse part we collect radiation from all directions (μ', ϕ') coming not directly from the sun, which are scattered into the direction (μ, ϕ)

$$J_{diff}(\tau, \mu, \phi) = \frac{\tilde{\omega}}{4\pi} \int_0^{2\pi} \int_{-1}^1 L(\tau, \mu', \phi') P(\mu, \phi; \mu', \phi') \, d\mu' \, d\phi'. \tag{2.12}$$

For a given optical density τ the radiation coming directly from the sun is reduced to $F_\odot \exp(-\tau/\mu_0)$, when $F_\odot$ is the solar flux at the TOA. We compute the fraction that is scattered into the (μ, ϕ)–direction as

$$J_{dir}(\tau, \mu, \phi) = \frac{\tilde{\omega}}{4\pi} F_\odot P(\mu, \phi, -\mu_0, \phi_0) e^{-\tau/\mu_0}. \tag{2.13}$$

Substituting (2.12) and (2.13) into (2.11) we get the radiative transfer equation for solar radiation

$$\mu \frac{dL(\tau, \mu, \phi)}{d\tau} = L(\tau, \mu, \phi) - \frac{\tilde{\omega}}{4\pi} \int_0^{2\pi} \int_{-1}^1 L(\tau, \mu', \phi') P(\mu, \phi; \mu', \phi') \, d\mu' \, d\phi'$$
$$- \frac{\tilde{\omega}}{4\pi} F_\odot P(\mu, \phi; -\mu_0, \phi_0) e^{-\tau/\mu_0}. \tag{2.14}$$

The phase function $P(\mu, \phi; \mu', \phi')$ strongly depends on the size and shape of the scattering particle. We may express it as a function of the scattering angle Θ (i.e., the angle between (μ, ϕ) and (μ', ϕ'), see Figure 2.3) by a series of Legendre polynomials P_l (Bronstein and Semendjajew, 1991)

$$P(\cos \Theta) = \sum_{l=0}^{N} \tilde{\omega}_l P_l(\cos \Theta), \tag{2.15}$$

or as a function of the angles of incoming and outgoing radiation using the associated Legendre polynomials P_l^m

$$P(\mu, \phi; \mu', \phi') = \sum_{m=0}^{N} \sum_{l=m}^{N} \tilde{\omega}_l^m P_l^m(\mu) P_l^m(\mu') \cos\big(m(\phi' - \phi)\big). \tag{2.16}$$

The sum over l with $m = 0$ gives the fraction which is independent of the azimuth angle ϕ.

2.1.2 Two-Stream Approximations

Climate and numerical weather prediction models need fast and accurate radiative transfer algorithms, which of course means that a compromise between speed and precision has to be found. Nearly all models use one or the other variant of a two-stream approximation, which we will derive in the following section. The Delta-Eddington approach will be emphasized, since this is implemented in the ECHAM model. All schemes neglect the azimuthal dependency of the phase function, since only the fluxes integrated over all azimuthal directions are of interest. A comprehensive comparison of the various schemes is given by King and Harshvardhan (1986).

Two-Stream Approximation

In order to find an exact solution of the radiative transfer equation (2.14) we can discretize the latter into a set of first order differential equations. This method is called the *discrete ordinate method*. We get

$$\mu_i \frac{dL(\tau, \mu_i)}{d\tau} = L(\tau, \mu_i) - \frac{\tilde{\omega}}{2} \sum_{j=-n}^{n} L(\tau, \mu_j) P(\mu_i, \mu_j) a_j - \frac{\tilde{\omega}}{4\pi} F_\odot P(\mu_i, \mu_0) e^{-\tau/\mu_0},$$
$$i = -n, \ldots, n \quad (2.17)$$

We can choose the interpolation nodes μ_i such that $\mu_{-i} = \mu_i$ and $a_{-j} = a_j$ ($\sum_j a_j = 2$), where a_j are the weighting factors. Furthermore we can use the phase function in its form (2.16), regarding only the azimuth independent part, and define the coefficients

$$c_{i,j} = \frac{\tilde{\omega}}{2} a_j P(\mu_i, \mu_j) = \frac{\tilde{\omega}}{2} a_j \sum_{l=0}^{N} \tilde{\omega}_l P_l(\mu_i) P_l(\mu_j), \quad j = -n, \ldots, n,$$
$$c_{-0} = \frac{\tilde{\omega}}{4\pi} P(\mu_i, \mu_0) \tag{2.18}$$

Substituting (2.16) and (2.18) into (2.17) we get the simplified expression

$$\mu_i \frac{dL(\tau, \mu_i)}{d\tau} = L(\tau, \mu_j) - \sum_{j=-n}^{n} c_{i,j} L(\tau, \mu_i) - c_{-0} L(\tau, -\mu_0), \tag{2.19}$$

where $L(\tau, -\mu_0)$ stands for the downward direct radiation at τ.

The set of differential equations (2.17) is an exact representation of (2.11) for $n \to \infty$. A crude approximation is to set $n = 1$, i.e. we will only use two interpolation nodes, which we set according to the Gaussian quadrature to $\pm\mu_1 = \pm 1/\sqrt{3}$. Furthermore we expand the phase function in (2.16) only to the first order. As a result we get two coupled differential equations of first order for the upward and downward directed fluxes $F^\uparrow := L_1 = L(\tau, \mu_1)$ and $F^\downarrow := L_{-1} = L(\tau, -\mu_1)$, respectively. Therefore this method is called *two-stream approximation*. The equations to solve are

$$\mu_1 \frac{dF^\uparrow}{d\tau} = F^\uparrow - \frac{\tilde{\omega}(1+g)}{2} F^\uparrow - \frac{\tilde{\omega}(1-g)}{2} F^\downarrow - \frac{\tilde{\omega}(1 - 3g\mu_1\mu_0)}{4\pi} F_\odot e^{-\tau/\mu_0} \tag{2.20a}$$

$$-\mu_1 \frac{dF^\downarrow}{d\tau} = F^\downarrow - \frac{\tilde{\omega}(1+g)}{2} F^\downarrow - \frac{\tilde{\omega}(1-g)}{2} F^\uparrow - \frac{\tilde{\omega}(1 + 3g\mu_1\mu_0)}{4\pi} F_\odot e^{-\tau/\mu_0} \tag{2.20b}$$

Here we have introduced the *asymmetry factor* g, which is defined as the first moment of the scattering phase function

$$g = \frac{\tilde{\omega}_1}{3} = \frac{1}{2} \int_{-1}^{1} P(\cos\Theta) \cos\Theta \, d\cos\Theta, \tag{2.21}$$

with scattering angle Θ. The terms in (2.20) with coefficients $(1 - g)/2$ and $(1 + g)/2$ may be interpreted as the backward and forward scattered part of the multiply scattered radiation. The asymmetry factor itself expresses the fraction of the forward scattered radiation in a single scattering event. For isotropic scattering, like Rayleigh scattering, $g = 0$, whereas for scattering functions with a dominating peak in the forward direction g approaches 1. Mie scattering typically yields asymmetry factors around 0.86.

Eddington Approximation

Very similar to the just derived two-stream approximation is the *Eddington approximation*. Returning to the original radiative transfer function (2.11), we expand both radiance L and scattering phase function $P(\mu, \mu')$ into series of Legendre polynomials

$$L(\tau, \mu) = \sum_{l=0}^{N} L_l(\tau) P_l(\mu), \tag{2.22}$$

$$P(\mu, \mu') = \sum_{l=0}^{N} \tilde{\omega}_l P_l(\mu) P_l(\mu'). \tag{2.23}$$

With (2.22) and (2.23) we may write the transfer equation as a set of $N + 1$ first order coupled differential equations. This is also called *spherical harmonic method*. The Eddington approximation is to simply cut the series at $N = 1$. The expansions (2.22) and (2.23) become to

$$P(\mu, \mu') = 1 + 3g\mu\mu', \tag{2.24}$$

and

$$L(\tau, \mu) = L_0(\tau) + L_1(\tau)\mu, \tag{2.25}$$

respectively. We get the two coupled differential equations for the first expansion coefficients L_0 and L_1

$$\frac{dL_1}{d\tau} = 3(1 - \tilde{\omega})L_0 - \frac{3\tilde{\omega}}{4\pi}F_\odot e^{-\tau/\mu_0}, \tag{2.26a}$$

$$\frac{dL_0}{d\tau} = (1 - \tilde{\omega}g)L_1 + \frac{3\tilde{\omega}}{4\pi}g\mu_0 F_\odot e^{-\tau/\mu_0}. \tag{2.26b}$$

The solution can be done by standard methods with integration constants, which are determined by the boundary conditions. The upward and downward directed fluxes can then be written as

$$F^{\uparrow/\downarrow}(\tau) = 2\pi \int_0^{\pm 1} (L_0 + \mu L_1)\mu \, d\mu = \pi \left(L_0 \pm \frac{2}{3}L_1 \right). \tag{2.27}$$

General Two-Stream Formulation

As we have seen in the derivation of (2.20) and (2.26) there are a number of similarities between the two-stream and the Eddington approximation. Actually, both can be unified to a *general two-stream approximation* (see e.g. Meador and Weaver, 1980). Its derivation starts by formulating differential equations for the up- and downward directed fluxes $F^{\uparrow/\downarrow}$. It is then assumed that the diffuse scattering can be described as a linear combination of up- and downward directed fluxes:

$$\frac{dF^\uparrow(\tau)}{d\tau} = \gamma_1 F^\uparrow(\tau) - \gamma_2 F^\downarrow(\tau) - \gamma_3 \tilde{\omega} F_\odot e^{-\tau/\mu_0} \tag{2.28a}$$

$$\frac{dF^\downarrow(\tau)}{d\tau} = \gamma_2 F^\uparrow(\tau) - \gamma_1 F^\downarrow(\tau) + (1 - \gamma_3)\tilde{\omega} F_\odot e^{-\tau/\mu_0}. \tag{2.28b}$$

If we now compare the latter equations with (2.20) and (2.26)–(2.27) we can derive the coefficients γ_i for these two approximations, which are summarized in Table 2.1.

We can solve the differential equations of the general two-stream approximation (2.28) for a plane parallel layer with the boundary condition $F^\uparrow(\tau) = 0$ and $F^\downarrow(0) = 0$, i.e. radiation enters the layer from above and there is no source at the ground (for an underlying layer with non zero reflectivity R^-, which is the general case, the boundary condition would have been $F^\uparrow(\tau) = R^- F^\downarrow(\tau)$) (Meador and Weaver, 1980). The reflectivity $R = F^\uparrow(0)/(\pi F_\odot \mu_0)$ and transmissivity $T = \exp[-\tau/\mu_0] + F^\downarrow(\tau)/(\pi F_\odot \mu_0)$ can then

approximation	γ_1	γ_2	γ_3
two-stream	$\dfrac{2 - \tilde{\omega}(1 + g)}{2\mu_1}$	$\dfrac{\tilde{\omega}(1 - g)}{2\mu_1}$	$\dfrac{1 - 3g\mu_1\mu_0}{2}$
Eddington	$\dfrac{7 - \tilde{\omega}(4 + 3g)}{4}$	$-\dfrac{1 - \tilde{\omega}(4 - 3g)}{4}$	$\dfrac{2 - 3g\mu_0}{4}$

Table 2.1: Coefficients for the two-stream and Eddington approximation in the formulation of the general two-stream approximation in (2.28).

be written as (Barker, 1996)

$$R = \frac{\tilde{\omega}}{a} \frac{r_+ e^{k\tau} - r_- e^{-k\tau} - r e^{-\tau/\mu_0}}{e^{k\tau} - \beta e^{-k\tau}} \tag{2.29a}$$

$$T = e^{-\tau/\mu_0} \left(1 - \frac{\tilde{\omega}}{a} \frac{t_+ e^{k\tau} - t_- e^{k\tau} - t_- e^{-k\tau} - t e^{\tau/\mu_0}}{e^{k\tau} - \beta e^{-k\tau}}\right), \tag{2.29b}$$

using

$$r_\pm = (1 \mp k\mu_0)(\gamma_1\gamma_3 + \gamma_2(1 - \gamma_3) \pm k\gamma_3 \tag{2.30a}$$

$$r = 2k[\gamma_3 + (\gamma_1\gamma_3 + \gamma_2(1 - \gamma_3))\mu_0 \tag{2.30b}$$

$$t_\pm = (1 \pm k\mu_0)(\gamma_1\gamma_4 + \gamma_2\gamma_3 \pm k(1 - \gamma_3)) \tag{2.30c}$$

$$t = 2k[(1 - \gamma_3) + (\gamma_1(1 - \gamma_3) + \gamma_2\gamma_3)\mu_0] \tag{2.30d}$$

$$a = [1 - (k\mu_0)^2](k + \gamma_1) \tag{2.30e}$$

$$k = \sqrt{\gamma_1^2 - \gamma_2^2} \tag{2.30f}$$

$$\beta = -\frac{k - \gamma_1}{k + \gamma_1} \tag{2.30g}$$

2.1.3 Similarity Principle

The expansion of the phase function into a series of Legendre polynomials up to the first degree is exact only for isotropic functions. In the case of Mie scattering by cloud droplets or aerosol particles, P, has a large delta-shaped peak in the forward direction. We can separate this peak, which contains a fraction f of the energy, and describe only the remaining part via a Legendre series. We define the *scaled asymmetry factor g^** as

$$g^* = \frac{g - f}{1 - f}. \tag{2.31}$$

The azimuth independent phase function then becomes

$$P(\mu, \mu') = 2f\delta(\mu - \mu') + (1 - f)(1 + 3g'\mu\mu') \tag{2.32}$$

and we may write the radiative transfer equation for diffuse radiation (see (2.14))

$$\mu\frac{dL(\tau, \mu)}{d\tau} = L(\tau, \mu)(1 - \tilde{\omega}f) - \frac{\tilde{\omega}(1 - f)}{2}\int_{-1}^{1}(1 + 3g'\mu\mu')L(\tau, \mu')\,d\mu'. \tag{2.33}$$

By defining the scaled properties

$$\tau^* = (1 - \tilde{\omega}f)\tau, \tag{2.34}$$

$$\tilde{\omega}^* = \frac{(1 - f)\tilde{\omega}}{1 - \tilde{\omega}f}, \tag{2.35}$$

$$P^*(\mu, \mu') = 1 + 3g^*\mu\mu' \tag{2.36}$$

we can formulate (2.33) analogously to the original equation (2.14)

$$\mu\frac{dL(\tau^*, \mu)}{d\tau^*} = L(\tau^*, \mu) - \frac{\tilde{\omega}}{2}\int_{-1}^{1}L(\tau^*, \mu')P^*(\mu, \mu')\,d\mu'. \tag{2.37}$$

The scaling in (2.31) and (2.34)–(2.36) is called *similarity principle*.

2.1.4   Absorption

Till now we have only dealt with the case of conservative scattering, i.e. we have calculated the part J_{scatt} of the source function in (2.11). In this section we will sketch an approach to compute the absorption part, J_{abs}.

Path Length Distribution

As already stated above, in the shortwave spectrum absorption and scattering occur simultaneously. The method of *distribution of photon path length* nevertheless determines the two quantities separately. We therefore first compute the fluxes of a conservative atmosphere F_c. Then we work out the probability distribution function of the optical path length, $p(\Lambda)$, which the photons have traveled. The optical path in a homogeneous layer is

$$\Lambda = k_s l, \tag{2.38}$$

where k_s is the scattering coefficient and l the geometrical path length. The transmission through a layer of absorbing atmosphere with absorption coefficient k_a is

$$t = \exp(-k_a l) = \exp\left(-k_a\frac{\Lambda}{k_s}\right) \tag{2.39}$$

Together with F_c and $p(\Lambda)$ we can thus write the flux F transmitted through an absorbing atmosphere as

$$F = F_c\int_0^{\infty}p(\Lambda)\exp\left(-k_a\frac{\Lambda}{k_s}\right)d\Lambda. \tag{2.40}$$

In order to be able to use (2.40) we have to know F_c and $p(\Lambda)$. While we can determine the former by some standard method like the ones derived in the previous section, the latter is more complicated. However, there are a number of approaches for doing this. We will use the inverse Laplace transformation.

The fraction $Y = F/F_c$ written as a function of $y = k_a/k_s$ is, following (2.40),

$$Y(y) = \frac{F}{F_c} = \int_0^\infty p(\Lambda) \exp(-y\Lambda)\, d\Lambda = \mathcal{L}[p(\Lambda)], \tag{2.41}$$

where $\mathcal{L}$ is the Laplace transform. Thus, once we know $Y(y)$, we also know

$$p(\Lambda) = \mathcal{L}^{-1}[Y(y)] \tag{2.42}$$

from the inverse Laplace transformation. Numerically (2.42) can be solved by discretizing $Y(y)$ at $2N$ points, i.e. to perform $2N$ monochromatic computations with fixed absorption coefficient k_a and deduce from them the fraction Y_i. The details can be seen in Bakan and Quenzel (1976) or Fouquart (1974).

Distribution of Absorber Amount

When we set $\Lambda = k_s l$ in (2.38) we implicitly assume that the atmosphere is homogeneous with respect to absorption. For a real atmosphere pressure, p, and temperature, T, vary with height and so does the absorption coefficient. Goody (1964) developed the *scaling approximation* to account for this vertical stratification by defining a scaled absorber amount u^* such that the optical path can be written as $\tau = k_a(p_r, T_r)u^*$ with the reference pressure p_r and the reference temperature T_r. He finds

$$u^* = \int_u \left(\frac{p}{p_r}\right)^n \left(\frac{T_r}{T}\right)^m du, \tag{2.43}$$

where u is the original absorber mass. The constants n and m depend on the absorber type and the spectral range. Analogously to the previous section, we may introduce the frequency distribution $p(u^*)$, describing the probability for a ray to traverse a scaled absorber amount u^*, and get (cf. (2.40))

$$F = F_c \int_0^\infty p(u^*) \exp(-k_a u^*)\, du^*. \tag{2.44}$$

The same procedure as for the distribution of photon paths can be applied in order to determine $p(u^*)$. The problem can be simplified by using the dependency of the absorption A on the absorber amount in the limits of weak and strong absorption,

$$A \propto \begin{cases} \overline{u^*} = \int_0^\infty p(u^*)u^* du^*, & \text{for weak absorption} \\ \overline{\sqrt{u^*}} = \int_0^\infty p(u^*)\sqrt{u^*} du^*, & \text{for strong absorption.} \end{cases} \tag{2.45}$$

We will use an *effective absorber amount* u_e between $\sqrt{\overline{u^*}}$ and $\overline{u^*}$. From the result of the Laplace transformation it follows that $\overline{u^*} = -(d(\ln F(k_a))/dk_a)_{k_a=0}$. Hence, we define

$$u_e = -\frac{\ln F(k_1) - \ln F(k_2)}{k_1 - k_2}, \tag{2.46}$$

where k_1 and k_2 are typical absorption coefficients in the current spectral band for low and high absorptive spectral regions. This means the transmission function over the whole solar spectrum, t_{sol}, may be approximated by the exponential series (also called the *exponential sum fitting method*)

$$t_{sol}(u) = a_1 \exp(-k_1(p_r, T_r)u_e) + a_2 \exp(-k_2(p_r, T_r)u_e). \tag{2.47}$$

$F(k)$ in (2.46) denotes up- or downward fluxes computed for the given absorption coefficient k.

If there is a cloudy layer with high reflectivity, a large fraction of the incoming radiation will not reach the layers below the cloud. The concentration of water vapor and other absorbing quantities increases in lower altitudes. Therefore the probability functions for radiation traversing the cloudy layer and getting reflected at a lower layer or the surface, p_i, is different from that of the directly reflected, p_1. To be precise we would have to introduce a probability distribution function for each reflection height. But, since the probability distribution has already become very broad after the first cloudy layer, it suffices to divide the fluxes into directly reflected, F_1, and those (eventually multiply) reflected in lower layers, F_2. Thus, we get for the upward fluxes

$$F^{\uparrow} \approx F_1^{\uparrow} t(u_{e1}) + F_2^{\uparrow} t(u_{e2}), \tag{2.48}$$

where u_{e1} and u_{e2} are the effective absorber amounts encountered by the radiation corresponding to F_1 and F_2, and t is the transmissivity.

2.2   Fouquart Scheme

The ECHAM5 model uses the solar radiation scheme developed by Fouquart and Bonnel (1980) for the computation of the shortwave radiative transfer in the version, which is implemented in the ECMWF model (Morcrette, 1989a,b, 1991; Gregory et al., 1998). It uses a Delta-Eddington approximation for the cloudy layers. The optical properties of ice and liquid water clouds are parameterized according to Rockel et al. (1991) and Francis et al. (1994). For partly cloudy layers maximum-random overlap is assumed (Geleyn and Hollingsworth, 1979; Morcrette and Jakob, 2000). Apart from cloud and gaseous absorption five climatological and 11 transported aerosols are accounted for, using the methods of scaled absorber amount and photon path length distribution. From spectrally highly resolved line-by-line computations, absorption coefficient for spectral bands,

	ECHAM4	
band	1	2
wavelength range in μm	0.25–0.68	0.68–4.00

	ECHAM5			
band	1	2	3	4
wavelength range in μm	0.25–0.69	0.69–1.19	1.19–2.38	2.38–4.00

Table 2.2: Spectral bands of the ECHAM4 and ECHAM5 shortwave radiative transfer schemes.

covering many individual absorption lines, have been developed. This crude simplification is necessary in order to reduce the computational efforts. The wavelength ranges of the four bands are given in Table 2.2. In the older version the solar spectrum was only divided into two bands, which are also listed in Table 2.2. The simulations in Chapter 4 are performed with this older version. The main effect of the update to four bands is an improved absorption (see e.g. Wild et al., 1997). All properties are computed separately for each spectral band and added up to yield the total flux.

The following is a brief description of the computational scheme:

1. Cloud optical properties

   (a) The optical properties of clouds are computed for each spectral interval (Roeckner, 1995). First the effective radii of liquid and ice cloud particles have to be determined. For liquid water we use (Johnson, 1993)

   $$r_{el} = \left(\frac{3m_l}{4\pi\rho_{H_2O}N} \right)^{1/3}, \tag{2.49}$$

   with m_l the liquid water content N and the droplet density, which is prescribed as a function of altitude and surface type (ground or ocean). The effective radius is of the order of magnitude of $10\,\mu$m.

   The effective ice crystal size is parameterized according to McFarlane et al. (1992) as

   $$r_{ei} = c_0(c_1 \sum_{i=0}^{3} \delta_i(\log(m_i))^i)^\kappa, \tag{2.50}$$

   with m_i the ice water content. The constants are given in Roeckner et al. (1996). Typical values for r_{ei} are around $100\,\mu$m.

   The optical depth, single scattering albedo and asymmetry factor are computed for all spectral intervals. First the contribution of the liquid and the ice fraction are calculated separately and then combined to yield the final shortwave cloud

optical properties. The optical depth is computed according to

$$\tau = a_0 r_e \text{XWP}, \tag{2.51}$$

where the constant a_0 depends on both, spectral interval and species (ice or liquid water). r_e stands for the effective radius of ice particles or cloud droplets and XWP for ice or liquid water path, respectively. For single scattering albedo and asymmetry factor the following parameterizations are used

$$\tilde{\omega} = \sum_{i=0}^{3} b_i (\log r_e)^i \tag{2.52}$$

$$g = \sum_{i=0}^{4} c_i (\log r_e)^i \tag{2.53}$$

The coefficients are listed in Roeckner et al. (1996).

For a partly cloudy layer j the effective cloudiness $A_{c,j}^{eff}$ is computed using the maximum-random overlap assumption ($j = 0$ means surface)

$$A_{c,j}^{eff} = \begin{cases} 1 - (1 - A_{c,j}) \left(\frac{1 - A_{c,j}}{1 - A_{c,j+1}^{eff}} \right) & \text{if } A_{c,j} > A_{c,j+1}^{eff}, \\ 1 - (1 - A_{cj}) & \text{else.} \end{cases} \tag{2.54}$$

$A_{c,j}$ is the cloud fraction of the j-th layer. The radiative transfer computations are then done separately for clear sky and cloudy sky fraction in each layer. In the ECHAM5 version not only each layer, but additionally even the total column is divided into a completely cloud free and a cloudy part. For the cloudy part the scheme developed above is applied with a new cloud fraction relative to the cloudy part of the column A_c^{tot}

$$\tilde{A}_c^{eff} = \frac{A_c^{eff}}{A_c^{tot}}. \tag{2.55}$$

The corresponding fluxes are summed weighted by their area fraction.

(b) The scaled absorber amounts (cf. (2.46)) for water vapor and uniformly mixed gases (CO_2) are computed.

2. Pure scattering ($k_a = 0$)

(a) The optical depth for Rayleigh scattering is calculated for a layer of thickness Δp (in pressure coordinates) as a series

$$\frac{\tau_R}{\Delta p} = \sum_{i=0}^{6} c_i^{ray} \mu_i. \tag{2.56}$$

Since Rayleigh scattering is conservative and isotropic the single scattering albedo $\tilde{\omega}_R \equiv 1$ and asymmetry factor $g_R \equiv 0$.

(b) The continuum scattering (i.e., only uniformly mixed gases and particles are taken into account, but not clouds) is calculated. Therefore the optical properties of the aerosols (five climatologically prescribed and 11 transported) are summed up together with Rayleigh scattering according to

$$\tau_{cs}^+ = \tau_R + \tau_a(1 - \tilde{\omega}_a g_a^2) \tag{2.57}$$

$$\tilde{\omega}_{cs}^+ = \frac{\tau_R}{\tau_R + \tau_a} + \left(1 - \frac{\tau_R}{\tau_R + \tau_a}\right) \frac{\tilde{\omega}_a(1 - g_a^2)}{1 - \tilde{\omega}_a g_a^2} \tag{2.58}$$

$$\tau_{cs}^+ = \frac{g_a}{1 + g_a}\left(1 - \frac{\tau_R}{\tau_R + \tau_a}\right). \tag{2.59}$$

Thus, we get the complete clear sky optical properties.

(c) The *effective solar zenith angle* μ_{eff} accounts for decreasing direct and increasing diffuse radiation

$$\frac{1}{\mu_{eff}} = \frac{1 - A_c^{eff}}{\mu_0} + r A_c^{eff}, \tag{2.60}$$

where $r = 1.66$ is the diffusivity factor. Its inverse can be interpreted as the averaged cosine of the solar zenith angle over all directions, since diffuse radiation is assumed to be isotropic.

(d) Reflectivities and transmissivities for the individual layers are computed following the thin layer approach of Coakley Jr and Chylek (1975), for the two different boundary conditions: reflecting and non-reflecting lower layer.

(e) For the clouds first the delta-modified parameters are computed as given by (2.31), (2.34) and (2.35).

(f) Reflectivities and transmissivities for reflecting and non-reflecting underlying layer are computed following the Delta-Eddington approximation, i.e. the Eddington approach including the similarity principle. It is implemented following the scheme of Joseph et al. (1976).

(g) The combined transfer properties of cloudy and clear sky parts are calculated. This is done by simply weighting the reflectivities and transmissivities from the clear sky and cloudy sky computation according to the effective cloudiness

$$\tilde{R}_j = \tilde{A}_c^{eff} R_j^{cd} + (1 - \tilde{A}_c^{eff}) R_j^{cs} \tag{2.61a}$$

$$\tilde{T}_j = \tilde{A}_c^{eff} T_j^{cd} + (1 - \tilde{A}_c^{eff}) T_j^{cs} \tag{2.61b}$$

(h) Using the latter the pseudo fluxes $\hat{F}_j^c = F_j^c/F_\odot$ in the cloudy part and $\hat{F}_j^f = F_j^f/F_\odot$ in the clear-sky part can be computed, i.e. the fluxes relative to the incoming flux at the TOA. This is done by computing the downward fluxes from top to bottom, such that the downward directed pseudo flux in the j-th layer is $\hat{F}_j^c = \prod_{i=1}^{j-1} \tilde{T}_i$ or $\hat{F}_j^f = \prod_{i=1}^{i-1} T_i^{cs}$, respectively. The upward pseudo fluxes are worked out from bottom to top, adding up the reflections from each layer, taking into account the transmissivities for the layers above.

3. Absorbing atmosphere

   (a) For bands with $\lambda > 0.68\,\mu$m the same calculations as in the purely scattering case are done, but with an increased optical thickness due to absorption of either water vapor or carbon dioxide.

   (b) From the pseudo fluxes for the conservative case and the ones including an absorber, the effective absorber amount is determined following (2.46).

4. Absorption

   (a) The pseudo-fluxes $\hat{F}_j^c$ and $\hat{F}_j^f$ (the latter is computed for the completely cloud free column) are multiplied by the transmission functions corresponding to the effective absorber amount.

   (b) The absorption by ozone is accounted for by simply multiplying the fluxes by the transmission functions of the accumulated absorber amounts. That means the interaction between scattering and absorption is neglected. This is possible, because ozone is at such high altitudes that there is only little scattering due to the small air density and aerosol loading. For the first band, water vapor absorption is also accounted for in the same manner.

5. Finally the fluxes in the cloudy and total cloud free column are added according to

$$\hat{F}_j = A_c^{tot} \hat{F}_j^c + (1 - A_c)^{tot} \hat{F}_j^f \qquad (2.62)$$

2.3   Radiation Schemes for Spatially Highly Resolved Data

The two-stream approximation is currently used in general circulation models (GCM), because it offers a good compromise between precision and computational cost. However, in order to investigate the radiation fields of highly resolved satellite observations or cloud model simulations, higher accuracy is needed. The reference method for a fully three dimensional radiation computation has become the Monte Carlo simulation technique, which is briefly described. With respect to GCMs or satellite retrieval algorithms, the independent column approximation is a straightforward enhancement of the 1D code. This approximation is also applied in this study. In the second section its principle and limitations are discussed. Finally, some other methods are briefly mentioned.

2.3.1   Monte Carlo

The general idea of the Monte Carlo method is to simulate the paths of individual photons. When this is done for a sufficiently large number of photons, averaging over all the photons reaching a certain area from a selected direction gives the corresponding intensity. Comprehensive descriptions can be found in (Mayer, 1999) or (Scheirer, 2000, 2001).

Photons impinge at the TOA and travel from one scattering event to the next. The distance between two consecutive scattering events is determined by the scattering coefficient, from which the optical depth and, via Lambert-Beer's law, the probability for scattering is computed. The scattering phase function gives the probability distribution for the scattering direction. Random number generators are applied in order to translate these probability functions into actual path lengths and directions for an individual photon. The average over many photons resembles the distributions in a statistical manner. Absorption is treated similarly by summing up the probability for each photon to be absorbed along its way before it leaves the model domain either at the top or by reaching the ground. Cyclic boundary conditions are often applied, so loss through the sides is not possible.

There are no physical approximations in this scheme as long as the number of photons is large enough to ensure statistical significance (typically some 10^6 photons are used (Scheirer, 2001)). Nevertheless there are of course approximations implicitly introduced by the phase functions and scattering and absorption coefficients. They have to be deduced from cloud or atmospheric data and assumptions (e.g., about the shape and orientation of ice crystals) have to be made (see e.g. Macke et al., 1996).

In many studies the Monte Carlo technique is used as reference in order to identify effects of cloud inhomogeneities (Los and Duynkerke, 2000; Titov et al., 1997; Levkov et al., 1998; Barker and Fu, 1999; Coley and Jonas, 1997; Fu et al., 2000b; Cahalan et al., 1994; Cahalan et al., 1994; Marshak et al., 1998; O'Hirok and Gautier, 1997, 1998; Várnai, 2000; Scheirer and Macke, 2002) or cloud geometry (Podgorny et al., 1998; Liou and Rao, 1996; Barker et al., 1998, 1999), because in the limit of an infinite number of photons the fluxes should approach the real values, given a correct description of the optical properties.

2.3.2 Independent Column Approximation

Satellite measurements have gained more and more importance in the field of geophysics and meteorology, because they can supply continuous data of global coverage. Nevertheless, in contrast to direct local observation, the only measurable quantity is radiance at various wavelengths. From this the physical property of interest has to be deduced. In the case of cloud optical thickness this means basically to invert the methods described in Section 2.1, where we solved the equation of radiative transfer for reflectivity, transmissivity and absorptivity for known cloud optical properties. The measured reflectivity (in most cases only in the zenith direction $\mu = 0$) can then be inverted with (2.29a) to yield τ. Some additional assumptions about the vertical structure of the atmosphere and the cloud particle size distribution have to made in order to determine the single scattering albedo and asymmetry factor. The two-stream approximation we developed in Section 2.1.2 is very useful, because on the one hand, we obtain the desired quantity, namely upward directed radiation, and on the other hand, it is computationally fast, so that the huge
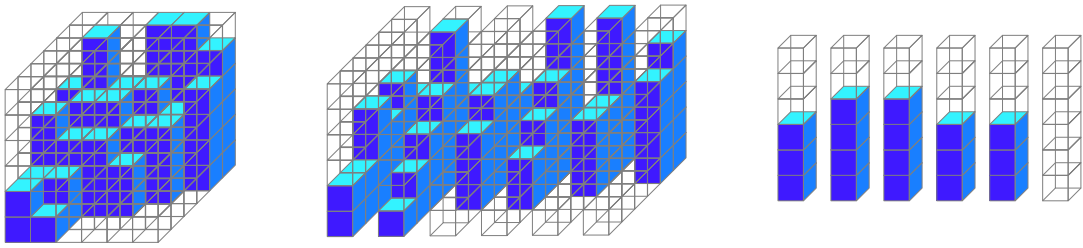
Figure 2.4: Hierarchical levels of accuracy of radiative transfer algorithms (Chambers et al., 1997): Full 3D information, 2D layers and individual columns.

data amounts of highly resolved satellite images can be processed with reasonable effort. It is therefore straightforward to apply the two-stream approximation to each reflectivity value of a single pixel in order to deduce the corresponding optical thickness (or any other property of interest) and thus transform the reflectivity image into a map of optical depth. Since no interactions between any two pixel values are accounted for, i.e. they are assumed to be independent, this approach is called the *independent pixel approximation (IPA)*. In short it simply assumes that each observation (satellite pixel or surface instrument observation point) can be treated as if it were, in fact, a horizontally homogeneous cloud, thereby ignoring the horizontal photon transport between pixels, but capturing the nonlinear relationship between cloud optical depth and cloud albedo for the whole scene (Chambers et al., 1997).

Returning to the initial problem of determining the radiation fluxes through a cloud, we can use the same idea underlying the IPA for spatially highly resolved cloud data e.g. from a cloud resolving model: First, the fluxes for each vertical column are computed separately using standard two-stream techniques, and then they are averaged over the scene of interest. Since one no longer deals with the *pixels* of an image, but with the *columns* of data this approach has been named the *independent column approximation (ICA)* (Oreopoulos and Barker, 1999). Both, IPA and ICA, are used interchangeably in the literature. In this work we will follow Oreopoulos and Barker (1999) and use IPA for satellite retrieval and ICA for determining fluxes from cloud data. The ICA can be positioned within hierarchical levels of accuracy as shown in Figure 2.4 (Chambers et al., 1997): The full information about the radiation field can only be revealed by accounting for the complete 3D structure. In 2D models, no interactions between neighboring layers are allowed. RADAR or LIDAR measurements produce such 2D data sets. The ICA further reduces the number of interactions by separating individual columns. Finally, in the PPH approximation information about the vertical structure and horizontal variability are additionally lost.

As stated above one major shortcoming of the ICA compared to a full three dimensional method like the Monte Carlo calculation is that photons are assumed to remain in the same column during all scattering processes. Simple geometric considerations reveal that

this cannot be generally true. When the sun stands low most photons will not stay in the same column that they entered at the TOA. This error is the more pronounced the smaller the columns and the smaller μ_0. Várnai and Davies (1996) introduced the *tilted IPA (TIPA)*, where they take intersects parallel to the direction of incident sun instead of vertical columns, thus reducing this error.

One can relax the assumption made above (either by applying the TIPA or using large enough columns or high sun elevations) as follows. The ICA assumes that the net horizontal photon transport is zero, i.e. there are as many photons leaving a column as entering it through its sides. For individual columns this assumption of zero net horizontal transport has been shown to be completely wrong. Titov and Kasjanov (1996) found that the net horizontal flux entering a single column can be of comparable magnitude as the absorbed flux. This means that an additional term H enters the energy budget equation for a single column, stating $A + R + T = 1 + H$. The horizontal fluxes H are a source or sink term. Marshak et al. (1995) have shown that the field of optical thickness that one would deduce from satellite data using the IPA is less variable than the one found with in situ aircraft measurements. On the other hand, the reflectivity computed from cloud data via the ICA is more inhomogeneous than the one typically observed from the TOA. They attribute this to the neglect of horizontal fluxes, which smooth the radiation field above the cloud. This *radiative smoothing* effect may be accounted for by allowing the neighboring pixels to influence the computation of the current pixel in the so called *non-local IPA (NIPA)* (Marshak et al., 1995; Marshak et al., 1996).

Nevertheless both effects are of minor importance, when the scene average is under investigation. For non-absorbing wavelengths horizontal fluxes average to zero, while there may be small residuals of either sign, when absorption is accounted for (Scheirer and Macke, 2002). A large number of studies deals with this topic. For overcast marine boundary clouds, comparisons between Monte Carlo and ICA computed fluxes show good agreement for averaging over scales smaller than about 5–6 km. The cloud data have been obtained from fractal cloud models (Cahalan et al., 1994; Titov and Kasjanov, 1996), RADAR (Zuidema and Evans, 1998) or LANDSAT images (Chambers et al., 1997). Similar results have been found for stratocumulus clouds with gaps (Marshak et al., 1997), broken clouds and trade cumulus (Chambers et al., 1997). In the latter study, only in the case of very inhomogeneous clouds, derived from LANDSAT data, the error of the IPA compared to a fully three dimensional computation, were of similar magnitude to the difference between PPH and IPA. For a cloud in the transition state from stratus to cumulus Fu et al. (2000b) have found averaging over 5 km to be sufficient, whereas for high rising tropical cumulus even 78 km are not enough. Only taking the mean over the complete scene, of 500 km range, reduces the influence of horizontal fluxes, such that they can be neglected. If the cloud sides are important as in the case of side illumination of high cumulus towers by a sun of low elevation, the ICA underestimates the cloud influence. Generally, for boundary layer clouds, scene averages over $\approx$ 5 km seem to be adequate,

whereas highly inhomogeneous tropical clouds can only be treated with the ICA when the domain is larger than some 100 km.

To conclude, the ICA has been shown to be a good tool for investigating the influence of horizontal variation of cloud properties from an energetic point of view. This means the average fluxes over a domain, which must have a minimum size depending on the inhomogeneity of the cloud, are correct, whereas the values for individual pixels may deviate substantially from the true fluxes due to horizontal fluxes. The applicability for satellite retrieval is thus considerably limited.

2.3.3   Other Methods

For completeness, two other methods used for studying the radiative transfer through clouds are briefly mentioned.

Spherical Harmonic Discrete Ordinate Method (SHDOM) This method has been developed by Evans (1998) and is often applied as a reference, in place or support of Monte Carlo results (Schulz, 1998; Duda and Spinhirne, 1997; Chambers, 1997; Chambers et al., 1997; Chambers et al., 2001). Its principle combines the elements of the Spherical Harmonic method (Zdunkowski and Korb, 1974) and the Discrete Ordinate method (Stamnes and Swanson, 1981). The three dimensional radiation field is computed directly from the three dimensional, inhomogeneous atmospheric input field, without introducing further assumptions.

Four-Stream Approximation In Section 2.1.2, the two-stream approximation was derived by simply approximating the integral over the phase function by its value at the first Gaussian quadrature points, i.e. figuratively choosing two streams. Taking into account the second Gaussian quadrature points yields the four-stream approximation. Higher order expansions are of course also possible (Kinne, 1996) and offer the possibility to achieve a better resolved radiation field, whereas from an energetically point of view they are not necessarily more precise (see e.g. Goody and Yung, 1989). Four-stream algorithms have also been applied for investigating the effect of inhomogeneous clouds on the radiative transfer (Fu et al., 2000b; Li and Fu, 2000).

Chapter 3

Correction Approaches

Physical parameterizations for climate models should be bias-free and as precise as possible, but at the same time they have to be computationally fast. Radiative transfer computations are therefore performed by some kind of two-stream approximation in most models. They include the plane parallel homogenous cloud approximation, which was shown to lead to a systematic error in Chapter 1. The idea to try to modify the highly optimized two-stream codes in order to correct for the effect due to the inhomogeneity of clouds suggests itself. Furthermore, many of the methods discussed in Section 2.3 are not adequate for large-scale models, because their input information is not supplied by the model. Currently, most climate models are not able to deal with any subgrid-scale information of clouds except fractional cloud cover, so it has to be empirically diagnosed, as is done in the effective thickness approach presented in Section 3.1. However, if the climate model supplies higher order moments of the cloud distribution, the latter can be exploited in the radiation computation, as is done in the statistical schemes sketched in Section 3.2.

3.1   Effective Thickness Approach

In Chapter 1 it was mentioned that the PPH-bias of the albedo is always positive, as can be directly concluded from Jensen's inequality, and so the true reflectivity of an inhomogeneous layer is lower than the one computed using the PPH approximation. In order to bring GCM fluxes at the TOA in accordance with satellite measurements the cloud and convection parameterizations have to be tuned such that an adequate amount of cloud condensate is generated. However, it is less than found in nature. Harshvardhan and Randall (1985) proposed, not to use the optical thickness as computed from the cloud properties directly, but a reduced value instead. They introduced a reduction factor χ such that the

reflectivity R of a cloudy layer with optical depth τ is

$$R(\tau) = R_{PP}(\chi\tau), \tag{3.1}$$

where R_{PP} is the reflectivity one obtains from the PPH computation without any correction for cloud variability. From global average values of albedo and cloud liquid water they estimated $\chi \approx 1/3$. In a numerical study with fractal cloud model data Davis et al. (1990) defined a *packaging factor* similar to (3.1) and found values on the order of magnitude of 0.1. These empirical approaches have been put onto a more physical basis by Cahalan et al. (1994). In the following section the concept of an *effective thickness approach (ETA)* similar to the one by Harshvardhan and Randall (1985) will be re-examined.

Visible optical thickness τ of a cloudy layer is a function of the liquid water path W,

$$\tau = \frac{3}{2}\rho_l \frac{W}{r_{\text{eff}}}, \tag{3.2}$$

with ρ_l the density of water and r_{eff} the effective droplet radius. The latter is not constant, but for stratocumulus clouds it can be set to a typical value of $r_{\text{eff}} = 10\,\mu\text{m}$ in good agreement with measurements (see e.g. Houze, 1993; Minnis et al., 1992).

Cahalan et al. (1994) claim that the cloud structure simulated by a bounded cascade model, a fractal cloud model, depicts the true variability in stratocumulus clouds. From the model characteristics the following relation between the mean of the logarithm of the liquid water path over the whole cloud model area, $\overline{\log(W)}$, and the logarithm of the mean, $\log(\overline{W})$, can be deduced as

$$\overline{\log(W)} = \log(\zeta(f)\overline{W}), \tag{3.3}$$

where f is the variance parameter, the only free parameter of the cloud model, which has to be ascertained empirically and held constant during a model run. Combining (3.2) and (3.3) yields the corresponding equality for optical thickness

$$\overline{\log(\tau)} = \log(\zeta\overline{\tau}). \tag{3.4}$$

If we now consider reflectivity, R, as a function of $\log(\tau)$, we may perform a Taylor expansion for any column i in the cloud domain with optical thickness τ_i about the value of $R(\log(\zeta\tau))$, such that

$$R_i(\log(\tau_i)) \approx R(\log(\zeta\overline{\tau})) + (\log(\tau) - \log(\zeta\overline{\tau}))R'(\zeta\overline{\tau}) + \frac{1}{2}(\log(\tau) - \log(\zeta\overline{\tau}))^2 R''(\zeta\overline{\tau}) + \cdots. \tag{3.5}$$

The reflectivity of the whole cloud scene, $\overline{R}$, is obtained by averaging over all columns i to get

$$\overline{R} = \frac{1}{n}\sum_{i=1}^{n} R_i = R(\log(\zeta\overline{\tau})) + \frac{1}{2}\text{var}(\log(\tau))R''(\zeta\overline{\tau}) + \cdots, \tag{3.6}$$

where $\text{var}(\log(\tau))$ is the variance of $\log(\tau)$. The second term on the right hand side of (3.5) cancels out because of (3.4). When we work out the domain reflectivity as in
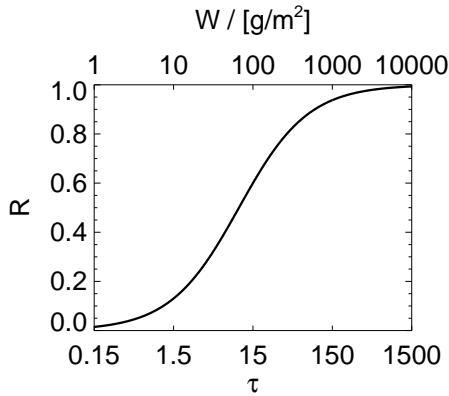
W / [g/m^2]

Figure 3.1: Reflectivity R of a layer as a function of its optical thickness τ or equivalently its liquid water path W on a logarithmic scale using (3.7). For intermediate optical thicknesses the curve is nearly linear, which is exploited in (3.8).

(3.6) we implicitly assume the independent column approximation to hold true (see also Section 2.3.2), since we assume the reflection of each column to be independent of its neighbors. Re-sorting the index i does not influence the average $\overline{R}$. In order to estimate the relevance of the R'' contribution in (3.6), we plot the reflectivity versus $\log(\tau)$ in Figure 3.1. Here we use the highly simplified reflection function

$$R(\tau) = \frac{\gamma\tau}{1 + \gamma\tau}, \tag{3.7}$$

with $\gamma \approx 0.1$ (King and Harshvardhan, 1986). For intermediate optical thicknesses in the range of 1.5 to 15 the curve is nearly linear, which means that R'' is small. Therefore, we can neglect this term in the Taylor series (3.6) and obtain

$$\overline{R} = R(\zeta\overline{\tau}). \tag{3.8}$$

Expanding $R(\log(\tau))$ instead of $R(\tau)$ directly thus has the advantage that the first order term cancels out and the second order term may be neglected for intermediate optical thicknesses. For small (large) values of τ the reflectivity according to (3.8) is too low (high). The cloud resolving model, from which (3.3) has been deduced, has originally been designed to simulate stratocumulus clouds, which have typically optical thicknesses in the range, where (3.8) is a good approximation.

When we compare (3.8) and (3.1) we can obviously establish a link to the reduction factor of Harshvardhan and Randall (1985) and set $\zeta = \chi$. The pre-factor ζ which results from the properties of the cloud model and the reflection function is basically the reduction factor of Harshvardhan and Randall (1985), but here it is defined for a single cloud realization instead of representing a global parameter.

We can rewrite (3.8) a little further by introducing the effective optical thickness τ_{eff}

$$\tau_{eff} = \chi\overline{\tau}. \tag{3.9}$$

Using the notation of (3.1) we can write the basic statement of the effective thickness approach as

$$R(\tau) = R_{PP}(\tau_{eff}), \tag{3.10}$$

i.e., the reflectivity of a cloudy layer with inhomogeneous horizontal optical thickness can be calculated by using the reflection function for a plane parallel homogeneous layer with the effective optical thickness instead of the actual. Jensen's inequality for the convex reflection function thus has been rewritten to an equality using the reduction factor $\chi < 1$.

If one wants to apply (3.10) in a GCM's radiation code, the actual value of χ has to be known. Cahalan et al. (1994) derive it from the bounded cascade model, where ζ, and therefore χ, is a function of the variance parameter f. From measurements he deduces $f = 0.5$ for marine stratocumulus clouds, which results in $\zeta = \chi = 0.7$. This means that for this cloud type the mean optical thickness has to be reduced by 0.7 when using the standard PPH radiation schemes. However, one cannot expect this factor to have the same value for all conditions.

1. The linear approximation of $R(\log(\tau))$ that have lead to (3.8) is only good for intermediate optical thicknesses. For stratocumulus clouds this is a reasonable assumption (Minnis et al., 1992), while for optically thick convective cumulus towers or thin cirrus clouds one leaves the linear range. However, this can be compensated by using smaller and higher reduction factors, respectively (see Figure 3.1).

2. For cloud types other than marine stratocumulus the variance parameter of the fractal model is different. Highly turbulent convective cloud result in larger f and therefore smaller χ. The inverse is true for more homogeneous clouds than the ones present during the FIRE measurement campaign. Consequently, a separate reduction factor each cloud type needs to be determined.

The need for different reduction factors is also shown by Szczap et al. (2000a,c), who extend the ETA to the *equivalent homogeneous cloud approximation (EHCA)*. They use a fractal cloud model and apply a Monte Carlo radiation scheme in order to determine the radiative fluxes. By comparing the PPH fluxes with the 3D Monte Carlo simulation they deduce effective optical thickness values for reflectivity and transmissivity separately. For large enough cloud areas they find that the two effective optical thicknesses are the same. Furthermore, they extract an empirical fit function for the dependence of the effective thickness, τ_{eff}, on the mean optical thickness and the relative cloud inhomogeneity $\sigma/\overline{\tau}$. For $\tau = 13$ they find $\tau_{eff}/\overline{\tau} = 0.7$, but for smaller τ this ratio is higher by up to 20%, for larger τ lower by up to 10%. In an accompanying paper Szczap et al. (2000b) further enhance the EHCA and define an effective single scattering albedo for absorbing clouds. The latter is smaller than the mean value. They again derive empirical relationships between the effective values of τ and $\tilde{\omega}$ and their means and standard deviations.

If the GCM provides not only the mean liquid and ice water path, but also the logarithmic mean, (3.3) could be used to determine χ. Otherwise, one could use fixed reduction factors for various typical weather situations. The main disadvantage of this approach is that interactions between external forcings like aerosol loading cannot be directly accounted for (Barker, 2000). However, until some measure of the sub-grid variability is

calculated by the GCM, this is the most practical method. Some studies for determining the appropriate reduction factor to use in GCMs will be presented in Section 5.4, along with different approaches for implementing them into the ECHAM5 GCM.

3.2   Statistical Schemes

The effective thickness approach we introduced in the previous section has some limitations. It only holds for a rather narrow range of optical depths and solar zenith angles, as we have seen earlier and is discussed in more detail by Cahalan et al. (1994) and Barker (1996). Furthermore, adjusting the optical thickness such that the reflectance is computed correctly could have undesirable effects on the estimate of cloud absorptance (Barker, 1996), since changes in optical thickness influence all radiative properties. In the following section we will develop another approach based on the following two assumptions:

1. The ICA is applicable. This was also assumed in the derivation of the ETA. We will especially make use of the consequence that the columns of the cloudy scene may be re-sorted without changing the result of the radiation computation, since they are all independent.

2. The frequency distribution of optical depth can be described by an analytical function. From satellite measurements various functions have been proposed, like Gamma- (Barker et al., 1996) , Beta- or log-normal-distribution (Oreopoulos and Davies, 1998b). We will concentrate on the Gamma and a variant of the Beta-distribution.

The general idea is to re-formulate the basic ICA approach presented in Section 2.3.2,

$$R = \frac{1}{N} \sum_{i=1}^{N} R_{PP}(\tau_i),$$

by substituting the sum by an integral over the probability distribution function (PDF), $p(\tau)$, of optical thickness, which has norm of 1,

$$\int_0^\infty p(\tau) \, d\tau = 1. \tag{3.11}$$

When p is known, reflectivity and transmissivity can be written as (Stephens, 1988b)

$$R = \int_0^\infty p(\tau) R_{PP}(\tau) \, d\tau \tag{3.12a}$$

$$T = \int_0^\infty p(\tau) T_{PP}(\tau) \, d\tau. \tag{3.12b}$$

In contrast to the ETA, there is no inherent limitation on the range over which this approach is valid, as long as p is an adequate description of the probability distribution. Different shapes for p have been proposed like Gamma-, Beta- or log-normal-distributions.

They are all empirical fits to either cloud observations or high resolution model output. The shape of the distribution cannot be deduced from basic cloud microphysical mechanisms. The actual choice mostly is made for practical reasons, like simple mathematics. The Gamma-distribution allows for an analytical expression in (3.12) and therefore has been chosen by Barker (1996). Tompkins (2002) favors the Beta-distribution, because both positive and negative skewed distributions can be realized, and the distribution is bounded above and below, avoiding unphysical negative or infinite values for water mixing ratio.

Generally, when the PDF is deduced from satellite data, as is done in most studies (Barker et al., 1996; Oreopoulos and Davies, 1998b), it only accounts for horizontal variations of the vertically integrated cloud water. In climate models, the atmosphere is divided into vertical layers with layer depths depending on the altitude (Roeckner et al., 1996), so that a cloud could be sliced into two (or more) contiguous layers. Usually, two-stream approximations account for this by assuming a vertical structure of the cloudy and clear sky fractions of each layer such that cloudy parts in adjacent layers are assumed to have maximum overlap, whereas cloudy layers separated by one or more clear sky regions are randomly overlapped. This is important, since the direct flux impinging on a layer residing under a cloudy layer are reduced. In total a shaded cloud has less radiative effect than an unshaded cloud. Similarly, if we look at a cloud with a known PDF, $p(\tau)$, which is sliced into two layers (cf. Figure 3.2), using only the effective reflection and transmission values (3.12) in each layer, is equivalent to homogeneous illumination. The real situation is depicted on the right side of Figure 3.2, where the impinging radiation in the second layer depends on the optical thickness of the overlying layer. The incoming radiation is less (more) than average for columns with thick (thin) top layers. Slicing the cloud into N layers with $N \rightarrow \infty$ yields the PPH approximation (Stephens, 1988b; Oreopoulos and Barker, 1999). This error becomes more pronounced if the thickness of the atmosphere model layers is decreased. In the next section, we will deduce a correction for this multilayer problem.

3.2.1   Gamma Weighted Two-Stream Approximation

In a series of two papers, Barker (1996) and Barker et al. (1996) are successful in fitting the distributions of optical thickness derived from LANDSAT measurements by Gamma-distributions,

$$p(\tau) = \frac{1}{\Gamma(\nu)} \left(\frac{\nu}{\overline{\tau}}\right)^{\nu} \tau^{\nu-1} e^{-\nu\tau/\overline{\tau}}, \tag{3.13}$$

where Γ is the Gamma function (Bronstein and Semendjajew, 1991) and ν is the shape parameter, which is defined as

$$\nu = \left(\frac{\overline{\tau}}{\sigma}\right)^{2}, \tag{3.14}$$

with σ the standard deviation of the distribution. Thus, ν is the inverse of the relative variance. Low values of ν mean high variability, and conversely, large ν indicates a homogeneous distribution. This follows an idea presented by Stephens et al. (1991), where radiative transfer through non-homogenous media is described using the PDF of the optical properties τ and $\tilde{\omega}$.

In a later study, Oreopoulos and Davies (1998b) also find that the Gamma-distribution could be used to represent the PDF of a large variety of cloud scenes. In contrast to Barker et al. (1996), they do not use the method of moments to determine ν from the satellite data (i.e. to compute $\overline{\tau}$ and σ and therefrom ν via (3.14)), but instead they applied the maximum likelihood estimate (MLE),

$$\frac{d\ln\Gamma(\nu)}{d\nu} + \ln\overline{\tau} - \ln\nu - \overline{\ln\tau} = 0, \tag{3.15}$$

which can be approximated by (Wilks, 1995)

$$\nu \approx \frac{1 + \sqrt{1 + 4(\ln\overline{\tau} - \overline{\ln\tau})/3}}{4(\ln\overline{\tau} - \overline{\ln(\tau)}}. \tag{3.16}$$

The latter approximation is especially advantageous for strongly skewed distributions with columns of high optical thickness, because the thick parts contribute less than in the method of moments.

Barker (1996) combines (3.13) and (3.12) with the reflectivities and transmissivities R_{PP} and T_{PP} from Meador and Weaver (1980) (see also Section 2.1.2, (2.29)–(2.30)). The Gamma-distribution has the advantage that (3.12) can be integrated analytically, yielding

$$T_{\Gamma} = \left(\frac{\nu}{\nu + \overline{\tau}\mu_0}\right)^{\nu} - \phi_1^{\nu}\frac{\tilde{\omega}}{a}[t_+\mathcal{F}(\beta,\nu,\phi_4) - t_-\mathcal{F}(\beta,\nu,\phi_6)] \tag{3.17a}$$

$$R_{\Gamma} = \phi_1^{\nu}\frac{\tilde{\omega}}{a}[r_+\mathcal{F}(\beta,\nu,\phi_1) - r_-\mathcal{F}(\beta,\nu,\phi_2) - r\mathcal{F}(\beta,\nu,\phi_3)], \tag{3.17b}$$

where

$$\mathcal{F}(\beta,\nu,\phi) = \sum_0^{\infty}\frac{\beta^n}{(\phi+n)^{\nu}}; \quad [|\beta| \le 1, \beta \ne 1, \nu > 0] \tag{3.18a}$$

$$\begin{aligned}
\phi_1 &= \frac{\nu}{2k\overline{\tau}}; & \phi_4 &= \phi_1 + \frac{1}{2k\mu_0} \\
\phi_2 &= \phi_1 + 1; & \phi_5 &= \phi_4 + 1 \\
\phi_3 &= \phi_4 + \frac{1}{2}; & \phi_6 &= \phi_1 + \frac{1}{2}
\end{aligned} \tag{3.18b}$$

The corresponding transmittance and reflectance properties for an isotropic diffuse-beam source are

$$t_{\Gamma} = \phi_1^{\nu}\frac{2k}{(k+\gamma_1)}\mathcal{F}(\beta,\nu,\phi_6) \tag{3.19a}$$

and

$$r_\Gamma = \phi_1^\nu \frac{\gamma_2}{(k+\gamma_1)}[\mathcal{F}(\beta,\nu,\phi_1) - \mathcal{F}(\beta,\nu,\phi_2)], \tag{3.19b}$$

respectively. In the case of conservative scattering, i.e. $\tilde{\omega} = 1$ (and hence $\beta = 1$), there is a removable singularity in the expressions for transmittance and reflectance of the direct (3.17) and diffuse beams (3.19). The corresponding formulas are (Barker, 1996)

$$T_\Gamma = \left(\frac{\nu}{\gamma_1\overline{\tau}}\right)^\nu \left[(\gamma_1\mu_0 + \gamma_4)\mathcal{G}\left(1-\nu, \frac{\nu}{\gamma_1\overline{\tau}}\right) - (\gamma_1\mu_0 - \gamma_3)\mathcal{G}\left(1-\nu, \frac{\nu\mu_0 + \overline{\tau}}{\gamma_1\mu_0\overline{\tau}}\right)\right] \tag{3.20a}$$

$$R_\Gamma = 1 - T_\Gamma \tag{3.20b}$$

for the direct beam and

$$t_\Gamma = \left(\frac{\nu}{\gamma_1\overline{\tau}}\right)^\nu \mathcal{G}\left(1-\nu, \frac{\nu}{\gamma_1\overline{\tau}}\right) \tag{3.21a}$$

$$r_\Gamma = 1 - t_\Gamma \tag{3.21b}$$

for the diffuse source. The function $\mathcal{G}$ is defined as

$$\mathcal{G}(1-\nu, x) = e^x \Gamma(1-\nu, x). \tag{3.22}$$

Any standard two-stream scheme, as described in Section 2.1.2, can be used by substituting the parameters γ_i, according to Table 2.1. The influence of any horizontal variations of optical depth within a single cloudy layer are accounted for by the transmission and albedo functions defined above. Since they have been obtained by weighting the general two-stream functions by the Gamma-distribution function this approach is called the *Gamma Weighted Two-Stream Approximation (GWTSA)*.

Strictly speaking, the Gamma-distribution only describes the optical depth distribution of clouds. Thus, if one wants to include clear sky properties, like Rayleigh scattering and aerosol effects, one can compute their contribution as τ_{clr} and obtains the total optical thickness as

$$\tau = \tau_{\text{clr}} + \tau_{\text{cld}}, \tag{3.23}$$

where τ_{cld} is given by the original PDF. Since the clear sky part is assumed to be horizontally homogeneous, we have to use a distinct shape parameter for the distribution of the total optical thickness, which can be approximated by

$$\nu = \left(\frac{\overline{\tau}_{\text{cld}} + \tau_{\text{clr}}}{\sigma}\right)^2 = \nu_{\text{cld}}\left(\frac{\overline{\tau}_{\text{cld}} + \tau_{\text{clr}}}{\overline{\tau}_{\text{cld}}}\right). \tag{3.24}$$

The integral in (3.12) has to be evaluated from τ_{clr} instead of from 0. This has only a minor effect on the result and makes an analytic solution impossible, so 0 is used.

As was already mentioned before, there is a problem when applying a statistical scheme like the GWTSA to multiple layers. In this case, the standard two-stream scheme treats
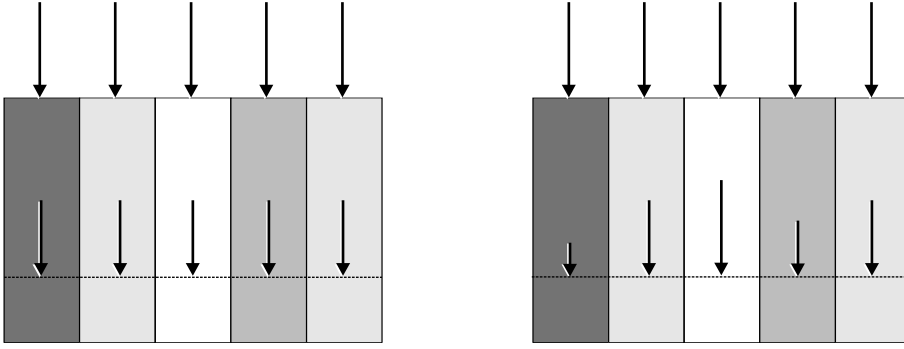
Figure 3.2: Radiative transfer through a multilayer cloud with horizontal inhomogeneity. The left sketch shows the case, where no correlation correction is applied, while on the right side the true situation is depicted, where thick elements reduce the transmitted light impinging on the underlying layer.

the optical depth distributions of the layers as being independent, which is generally not the case. Oreopoulos and Barker (1999) therefore develop a correction, assuming that the optical thickness distributions of a cloud in all layers can be described by the same shape parameter ν and the particular means τ_i. By further assuming that the distributions are perfectly correlated (see Figure 3.2), they find that for direct transmitted radiation the same formalism as described above can be used, but using an effective optical thickness, $\overline{\tau}_i^*$, as given by

$$\overline{\tau}_i^* = \frac{\nu \overline{\tau}_i}{\nu + \sum_{k=0}^{i-1} \overline{\tau}_k} \leq \overline{\tau}_i. \tag{3.25}$$

The GWTSA results using $\overline{\tau}_i$ approach the PPH solution as $N \to \infty$, while slicing does not change the result, when $\overline{\tau}_i$ is substituted by the effective thickness $\overline{\tau}_i^*$. In the case of diffuse radiation Oreopoulos and Barker (1999) develop an approximate solution, such that again only the optical thickness has to be rescaled. They find

$$\overline{\tau}_i^* = \frac{\nu \overline{\tau}_i}{\nu + \mathcal{D}(\mu_0) \sum_{k=0}^{i-1} \overline{\tau}_k/\mu_0}, \tag{3.26}$$

with

$$\mathcal{D}(\mu_0) = 0.063\mu_0(2 - \mu_0). \tag{3.27}$$

When implementing the GWTSA into a GCM, (3.26) can be applied for both direct and diffuse transmittance with only little influence on the result. The summation in (3.26) ranges from the cloud bottom to the cloud top layer. If cloudy layers are separated by clear sky, the GWTSA starts again from uncorrected $\overline{\tau}$ with the particular shape parameter ν_i, which is assumed to be constant throughout the contiguous cloudy layers.

The correction (3.26) is valid only for overcast skies. For partly cloudy layers, in which total radiative transfer is computed following (2.61), Oreopoulos and Barker (1999) give

the general corrected optical thickness

$$
\overline{\tau}_i^* = \begin{cases} \frac{A_{c,i-1}\overline{\tau}_i^{**} + (A_{c,i}-A_{c,i-1})\overline{\tau}_i)}{A_{c,i}}, & \text{for } A_{c,i-1} \leq A_{c,i} \\ \overline{\tau}_i^{**}, & \text{for } A_{c,i-1} > A_{c,i} \end{cases} \tag{3.28a}
$$

with

$$
\overline{\tau}_i^{**} = \frac{\nu_i \overline{\tau}_i}{\nu_i + \mathcal{D}(\mu_0) \sum_{k=k_{\text{top}}}^{i-1} \mathcal{A}_k \overline{\tau}_k / \mu_0}. \tag{3.28b}
$$

The parameter $\mathcal{A}_k$ has been introduced since it *"[. . .] was found to improve results relative to $\mathcal{A}_k = 1$ for a wide variety of experiments. In a crude way, this mimics the effects of maximum/random cloud overlap [. . .]"* (Oreopoulos and Barker, 1999). They found the empirical relation

$$
\mathcal{A}_k = \begin{cases} (1 - A_{c,k-1})^{-1}, & \text{for } A_{c,k} \leq 0.5 \\ A_{c,k}^{-1}, & \text{for } A_{c,k} > 0.5. \end{cases} \tag{3.29}
$$

We set this tuning parameter to 1, since the Fouquart scheme uses an effective cloudiness (see (2.54)), which already accounts for the overlap.

The underlying assumption for the derivation of the correction in (3.28) is that a single cloud is perfectly correlated throughout its vertical extent. This is not generally true, but the correlation is likely to decrease with larger vertical distance between two layers. The correction is therefore an upper limit, the "true" value for $\overline{\tau}^{**}$ will be larger than stated in (3.28). Till now, only limited observational data are available for describing the vertical structure of clouds — a problem, which is important for finding the correct overlap assumptions also (Collins, 2001). Radar measurements by Hogan and Illingworth (2001), the use of longterm rawinsonde datasets (Wang et al., 2000) or the upcoming space borne measurements on the CLOUDSAT satellite (Stephens et al., 2000) might be a good starting point for developing more sophisticated parameterization for cloud vertical structure. Lacking these observational data, perfect correlation nevertheless is a physically profound assumption, comparable to maximum overlap for adjacent layers.

The GWTSA has been shown to work quite successfully with cloud resolving model and satellite data (Barker et al., 1996; Oreopoulos and Davies, 1998b; Oreopoulos and Barker, 1999; Barker and Fu, 1999; Barker and Fu, 2000). It has also been implemented in a discrete ordinate two-stream scheme (Kato et al., 2001). Using a similar approach, Fu et al. (2000a) developed a radiation model for infrared radiation, which he called the *Gamma Weighted Radiative Transfer scheme (GWRT)*.

3.2.2 Beta Weighted Two-Stream Approximation

The same concept developed above for the GWTSA can be used for a different choice of PDF. The *Beta Weighted Two-Stream Approximation (BWTSA)* employs a Beta-shaped PDF instead the Gamma-distribution. Thus, it can be linked consistently to the cloud

scheme of the ECHAM5 model, where the PDF of the total water mixing ratio in each grid cell is expressed by means of a Beta-distribution (Tompkins, 2002). First the statistical cloud cover scheme, providing the distribution for the radiation computation, is briefly described. Then the implementation of the BWTSA in the ECHAM5 model is sketched.

Statistical Cloud Cover Scheme

Clouds are the most important modulator of the incoming and outgoing radiation and therefore have attracted a lot of modeling efforts. In the early stages of the development of GCMs, clouds were treated, as most other model variables, with only a single average number per grid cell, i.e., the cell was either overcast or cloud free. Looking at the typical grid spaces of those models of several $100\,\mathrm{km}$, this assumption is obviously far from being realistic. Since the radiative properties of clear and cloudy sky differ substantially, parameterizations have been developed in order to diagnose or prognose the area fraction in each cell that is covered by clouds. All relevant computations are then performed independently in both parts and the fluxes are averaged according to the fractional areas. By introducing fractional cloud cover one implicitly assumes that some of the model variables are inhomogeneous within a single grid cell, because otherwise clouds always form in the whole layer. A simple approach to account for this variability is to set the relative humidity threshold, where clouds start to form, to less than 100% and define a functional dependency of the cloud fraction based on the difference between mean grid humidity and the threshold (Sundqvist, 1978; Lohmann and Roeckner, 1996). Setting a fixed threshold is basically equivalent to defining a typical variability of water mixing ratio.

Alternatively one can explicitly describe the cloud water variability by specifying a probability distribution function, p, of the total water mixing ratio, $q_t = q_v + q_l + q_i$, for each layer, with the mixing ratios of water vapor, q_v, cloud liquid water, q_l, and cloud ice, q_i. Knowledge of $p(q)$ together with the saturation mixing ratio, q_s, enables the computation of condensate, q_c, and vapor mixing rates, q_v, and cloud cover, A_c,

$$q_t = \int_0^\infty p(q) q \, dq \tag{3.30}$$

$$q_v = \int_0^{q_s} p(q) q \, dq + \int_{q_s}^\infty p(q) q_s \, dq \tag{3.31}$$

$$q_c = \int_{q_s}^\infty p(q)(q - q_s) \, dq \tag{3.32}$$

$$A_c = \int_{q_s}^\infty p(q) \, dq. \tag{3.33}$$

From a variety of possible shapes for $p(q_t)$ Tompkins (2002) chooses the Beta-distribution (e.g. Johnson and Kotz, 1970; Essenwanger, 1967)

$$p(q) = \frac{1}{B(\tilde{u}, \tilde{v})} \frac{(q_t - q_a)^{\tilde{u}-1}(q_b - q_t)^{\tilde{v}-1}}{(q_b - q_a)^{\tilde{u}+\tilde{v}-1}} \qquad \text{for } q_a \leq q_t \leq q_b, \, p = 0 \text{ otherwise}, \tag{3.34}$$

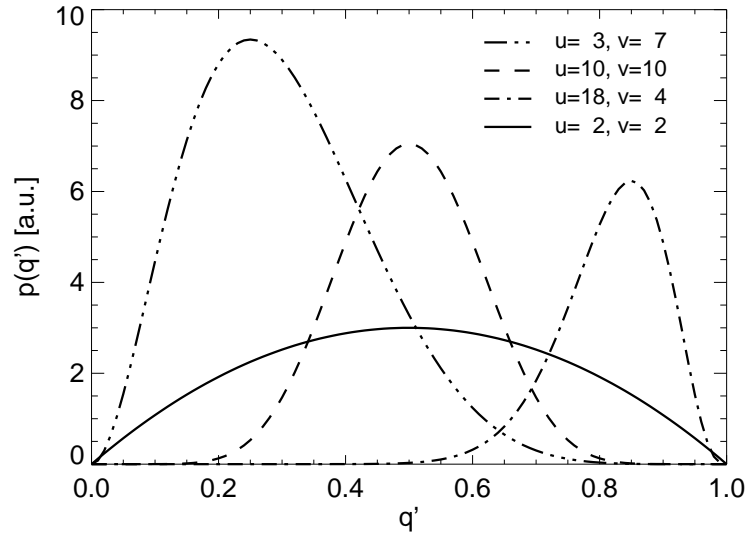**Figure 3.3:** Some examples of Beta distributions with different choices of the shape parameters $\tilde{u}$ and $\tilde{v}$. For $\tilde{u} < \tilde{v}$ the distributions are positively, for $\tilde{u} > \tilde{v}$ negatively skewed and symmetrical for $\tilde{u} = \tilde{v}$. (Not shown are the U-shaped distributions, which are generated for negative shape parameters, since they are not used in the scheme.)

where $B(\tilde{u}, \tilde{v})$ represents the beta function

$$B(\tilde{u}, \tilde{v}) = \frac{\Gamma(\tilde{u})\Gamma(\tilde{v})}{\Gamma(\tilde{u} + \tilde{v})}. \tag{3.35}$$

Its standard deviation is

$$\sigma = \frac{q_b - q_a}{\tilde{u} + \tilde{v}} \sqrt{\frac{\tilde{u}\tilde{v}}{\tilde{u} + \tilde{v} + 1}}. \tag{3.36}$$

Some examples of the beta distribution for various combinations of the shape defining parameters are shown in Figure 3.3. These examples may elucidate the reasons for choosing this distribution for the PDF of q_t:

- The distribution is bounded above and below. Other distributions like the lognormal- or Gamma-distribution are open, which means that there are infinite or negative values of q_t. Although the corresponding probability is usually negligible, such values are nevertheless unphysical.

- The skewness may by positive or negative, depending on the shape parameters $\tilde{u}$ and $\tilde{v}$: The distribution is symmetrical for $\tilde{u} = \tilde{v}$, positively skewed for $\tilde{u} < \tilde{v}$, and negatively skewed for $\tilde{u} > \tilde{v}$. Such a property is necessary, since both shapes have been observed and have been modeled in cloud resolving model simulations.

- Despite being quite flexible the Beta distribution is defined by only four parameters. Furthermore, these parameters are easily implemented into the cloud cover scheme. This will be sketched below.

Substituting (3.34) into (3.30)–(3.33) yields

$$q_t = (q_b - q_a)\frac{\tilde{u}}{\tilde{u} + \tilde{v}} + q_a \tag{3.37}$$

$$q_v = (q_b - q_a)\frac{\tilde{u}}{\tilde{u} + \tilde{v}}I_{(q_s-q_a)/(q_b-q_a)}(\tilde{u}+1, \tilde{v}) + (q_a - q_s)I_{(q_s-q_a)/(q_b-q_a)}(\tilde{u}, \tilde{v}) + q_s \tag{3.38}$$

$$q_c = (q_b - q_a)\frac{\tilde{u}}{\tilde{u} + \tilde{v}}[1 - I_{(q_s-q_a)/(q_b-q_a)}(\tilde{u}+1, \tilde{v})] + (q_a - q_s)[1 - I_{(q_s-q_a)/(q_b-q_a)}(\tilde{u}, \tilde{v})] \tag{3.39}$$

$$A_c = 1 - I_{(q_s-q_a)/(q_b-q_a)}(\tilde{u}, \tilde{v}), \tag{3.40}$$

where I_x is the incomplete Beta-function ratio, given by

$$I_x(\tilde{u}, \tilde{v}) = \frac{1}{B(\tilde{u}, \tilde{v})} \int_0^x q^{\tilde{u}-1}(1-q)^{\tilde{v}-1}\, dq. \tag{3.41}$$

An intuitive choice for a set of variables, which uniquely define the Beta-distribution, are the two limits and the two shape parameters. However, for the formulation of the cloud scheme Tompkins (2002) chooses the more convenient set q_t, q_c, $\tilde{u}$ and $\tilde{v}$, since the mixing ratios are more easily linked to the GCM. On the other hand, this set of variables is only independent for broken cloudiness. For $A_c = 1$ the total mixing ratio is $q_t = q_s + q_c$ and therefore a function of q_c, whereas for $A_c = 0$ there is no condensate, $q_c = 0$. In these cases, an additional variable $(q_b - q_a)$ is prognosed by the model. This variable is analyzed from q_t and q_c otherwise. It is therefore called a quasi-prognostic variable.

One shape parameter, $\tilde{u}$, is set to a constant value, which is arbitrarily chosen to be $\tilde{u} = \tilde{u}_0 \equiv 2$. Since currently only positively skewed shapes are used in order to make the formulation feasible, $\tilde{v} \geq \tilde{u}_0$. Future enhancements of the scheme may relax this limitation. Finally, the second shape parameter $\tilde{v}$ is determined prognosticly. Four physical mechanisms are taken into account:

Turbulence acts on both, distribution width (of course only in the cases of clear or overcast skies) and shape parameter. Mixing leads to homogenization of the variable fields of mixing ratios. It is parameterized as a Newtonian relaxation term

$$\frac{\partial \tilde{v}}{\partial t} = (\tilde{v}_0 - \tilde{v})\left(\frac{1}{t_v} + \frac{1}{t_h}\right), \tag{3.42}$$

where $\tilde{v}_0 = \tilde{u}_0$ is the initial value for $\tilde{v}$, and t_v and t_h are time constants connected with vertical and horizontal mixing, respectively. They are computed from the turbulent velocity scale and the wind shear. While the vertical part is only relevant in the planetary boundary layer, t_h is important higher up and is typically of the order of ten days. A similar formulation is also given for the width of the PDF, $(q_b - q_a)$, including some additional source terms.

Convection leads to detrainment of high mixing ratios of cloud condensate, which results in a significantly increased skewness of the PDF. This is accounted for in the scheme

by linking the shape parameter directly to the detrainment via

$$\frac{\partial \tilde{v}}{\partial t} = \frac{K}{\rho q_s} \frac{\partial}{\partial z}(M^{\text{cu}} q_c^{\text{cu}}), \tag{3.43}$$

where K is a dimensionless constant, M^{cu} the updraft mass flux and q_c^{cu} the mean cloud water in the convective updrafts. Again convection also influences the quasi-prognostic width $(q_b - q_a)$ by increasing q_b while q_a stays constant.

Large-scale condensation can change the condensate mixing ratio, which has to be taken into account in determining the PDF by an implicit update of the model variables.

Microphysics may also change the condensate amount through pathways between the various water categories, which are represented in the GCM cloud scheme. Similarly to the large scale condensation, this is treated as an implicit update of the condensate mixing ratio, resulting in a change $\Delta \tilde{v}^{\text{micro}}$.

Summarizing the above, we can write the prognostic tendency equation for $\tilde{v}$ as

$$\frac{\Delta \tilde{v}}{\Delta t} = \frac{K}{\rho q_s} \frac{\partial}{\partial z}(M^{\text{cu}} q_c^{\text{cu}}) + \frac{\tilde{v}^{\text{micro}}}{\Delta t} + (\tilde{v}_0 - \tilde{v})\left(\frac{1}{t_v} + \frac{1}{t_h}\right). \tag{3.44}$$

For further details and information about the performance of the scheme in the ECHAM5 general circulation model see (Tompkins, 2002).

Implementation into the Radiation Scheme

Following the principal idea of the statistical schemes stated in (3.12), the standard two-stream scheme of the ECHAM5 model is integrated, using weighting factors according to the probability function, which is supplied by the cloud cover scheme. The flow diagram is sketched in Figure 3.4. The PDF for the total water mixing ratios is defined by the four parameters: lower limit q_a, upper limit q_b and the shape parameters $\tilde{u}$ and $\tilde{v}$. From this PDF and the saturation mixing ratio, q_s, the PDF for the cloud condensate for cloudy layers is computed. It is the tail of the Beta-distribution (for partial cloud cover) or the complete Beta-distribution (for overcast skies), with the same shape parameters as the total water mixing ratio PDF, but with the new limits

$$q_{c,a} = \max(q_a - q_s, 0) \tag{3.45a}$$

and

$$q_{c,b} = q_b - q_s. \tag{3.45b}$$

The condensate is divided into the two aggregate states, liquid and ice, according to the corresponding fractions of the mixing ratio mean values. With the fraction of ice,

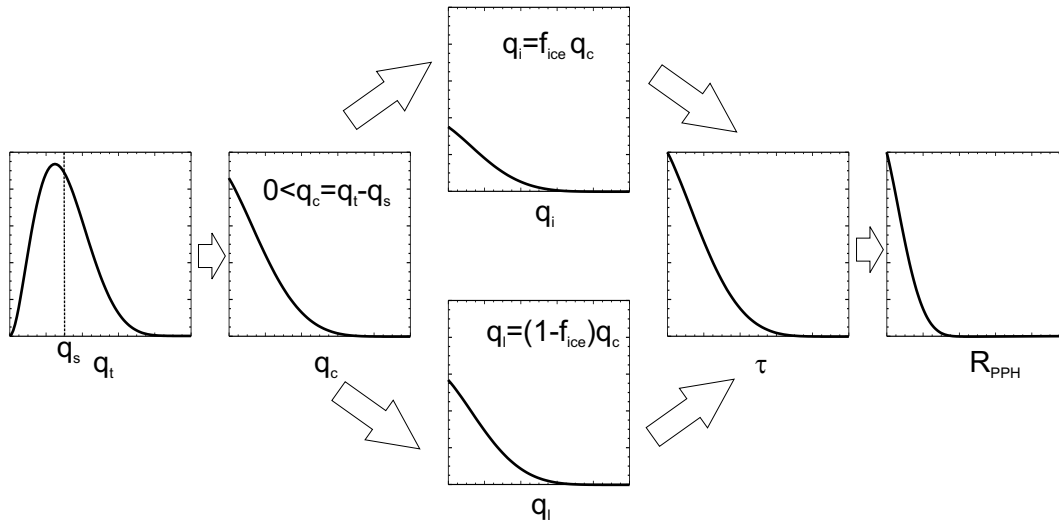$$f_{\text{ice}} = \frac{q_{ice}}{q_{ice} + q_{liq}}, \tag{3.46}$$

Figure 3.4: Flow diagram of the BWTSA approach: From the distribution of total water mixing ratios the condensate part is determined. Using the standard parameterization this can be transformed to a distribution of optical thicknesses which is finally passed to the statistical radiation scheme.

the PDFs for both are described by the shape parameters $\tilde{u}$ and $\tilde{v}$ and the limits $f_{ice}\, q_{c,a}$ and $f_{ice}\, q_{c,b}$ for ice, and $(1 - f_{ice})q_{c,a}$ and $(1 - f_{ice})q_{c,b}$ for liquid cloud water.

The integrals in (3.12) are calculated by Gaussian quadrature at five points, i.e., the shortwave code is called five times, passing different amounts of cloud liquid water and ice. The corresponding fluxes are then summed up after weighting according to the Gaussian algorithm. Besides numerical fluctuations, no additional approximations are introduced. In the case of thin clouds, however, the limited precision of the numerical integration may lead to an inconsistency in the Fouquart scheme when absorption is computed. As described in Section 2.2, the fluxes for a conservative atmosphere and then for a fixed absorption coefficient are determined. These two fluxes are subtracted in order to obtain the effective absorber amount. Numerical errors for small absorption may thus lead to negative absorption. These rare circumstances are corrected by setting the difference to zero if negative values occur. The overall fluxes are not affected substantially by this correction as one can easily test by performing the integration with more quadrature points, and thus higher precision. Five points were chosen as a compromise between precision and computational effort.

Chapter 4

Cloud Resolving Model Data Experiments

Cloud resolving models are the only way to systematically investigate the 3D properties of clouds. Satellites can only measure vertically integrated condensate amounts and the field of view of ground based devices like LIDAR and RADAR, which can resolve the vertical structure, is limited. Measurements during flight campaigns can gain valuable data sets for the development of parameterizations or model evaluations or to define boundary conditions for simulations, but it is not possible to obtain a snapshot of the full 3D structure of a cloud field.

In order to quantify the PPH-bias radiation computations using the ICA approach are compared to the corresponding PPH values. For the above mentioned reasons data from cloud simulations are chosen. After identifying the bias, the two correction approaches, ETA and GWTSA (see Chapter 3) are scrutinized. The latter is chosen as an example for a statistical scheme in favor of the BWTSA, because the Gamma-distribution yields better fits for the small domain size of the cloud simulations. While the Beta distribution was shown to be adequate for areas comparable to the GCM resolution, (Tompkins, 2002) it could not fit the cloud model data properly. Furthermore, a correlation correction is not available for the BWTSA, yet.

4.1 Cloud Data

Two simulations using a cloud resolving model developed at the Max-Planck-Institut für Meteorologie in Hamburg are employed in the following study: a nocturnal marine stratocumulus (ASTEX) and a trade wind cumuli (ATEX) simulation. First the cloud resolving model will be briefly introduced, followed by a short description of the model initializations and domains for the two cases.

4.1.1 Cloud Resolving Model

The Cloud Resolving Model (CRM) is based on the idea of Large Eddy Simulation (LES). LES means that all spatial scales, which represent the dominant large-scale motions, are explicitly resolved, while the effects of smaller scale turbulence on the averaged flow is parameterized. Therefore the dominant cloud structures are resolved. An extensive description of the LES model can be found in Chlond (1992, 1994) and Müller and Chlond (1996). Here only a brief summary, following Chlond and Wolkau (2000), is given.

For the prognostic equations of the wind velocity, the liquid water potential temperature and total water content the Boussinesq-approximation is applied. They are described on a Cartesian coordinate system, which is translated with the geostrophic wind to follow a trajectory of air in a Lagrangian manner. Infrared radiative cooling in cloudy conditions and the influence of large scale vertical motions is accounted for, while the sub-grid scale forcing is parameterized via the sub-grid scale turbulent energy closure. Microphysical processes such as condensation, evaporation, coagulation and sedimentation are modeled by bulk parameterization schemes.

4.1.2 Marine Stratocumulus (ASTEX)

The case study is based on a situation encountered during the *Atlantic Stratocumulus Transition Experiment (ASTEX)*. Flight RF06 took place to investigate a nighttime stratocumulus. From the data collected during this flight initial and boundary conditions for a 4-hour model simulation of the boundary layer have been derived as part of the European Cloud-Resolving Modelling (EUCREM) model intercomparison project. The details of the ASTEX experiment and especially the flight RF06 can be found in de Roode and Duynkerke (1997) and Duynkerke et al. (1999), respectively.

The flight path followed a stratocumulus cloud over the North Atlantic (37° N, 24° W) in its transition state. From an initially horizontally homogeneous cloud layer it developed into a decoupled boundary layer with cumulus penetrating the stratocumulus deck from below. The initial conditions for the simulation were derived as simplified vertical profiles of the two horizontal wind components, the liquid water potential temperature, and the total water content. These initial profiles were assumed to be horizontally homogeneous, except for the temperature field. In order to trigger convective instability, the initial temperature field was randomly perturbed. Figure 4.1 gives an impression of the evolving cloud field.

In their sensitivity study Chlond and Wolkau (2000) utilize different sub-grid scale parameterization schemes. The data used for the radiation computation in this work are labeled *REFERENCE* in their article. The first 30 min are neglected as LES model spin-up time. For the REFERENCE-case the model domain was $28.8 \times 3.2 \times 1.5\,\text{km}^3$ with a horizontal resolution of $\Delta x = \Delta y = 50\,\text{m}$ and a vertical level height of $\Delta z = 25\,\text{m}$. The time interval for model output was set to $3\,\text{min}$.
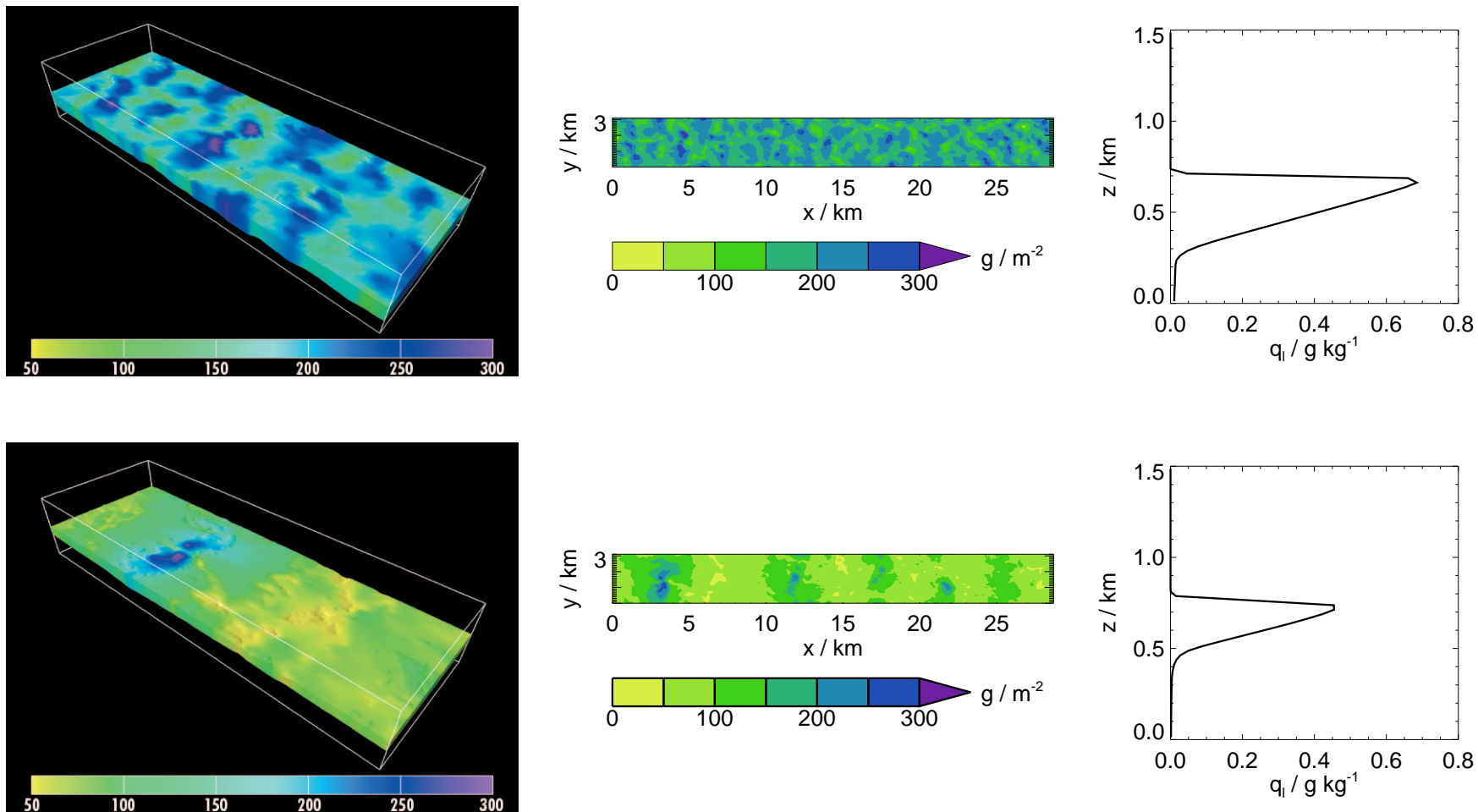
Figure 4.1: Snapshots of the ASTEX cloud simulation for 1 h (top panel) and 4 h (bottom panel) model time. Shown are volume surface plots (cut at $x = 10$ km), colored by the liquid water path (left), the liquid water path (center) and vertical profiles of the mean liquid water content (right)
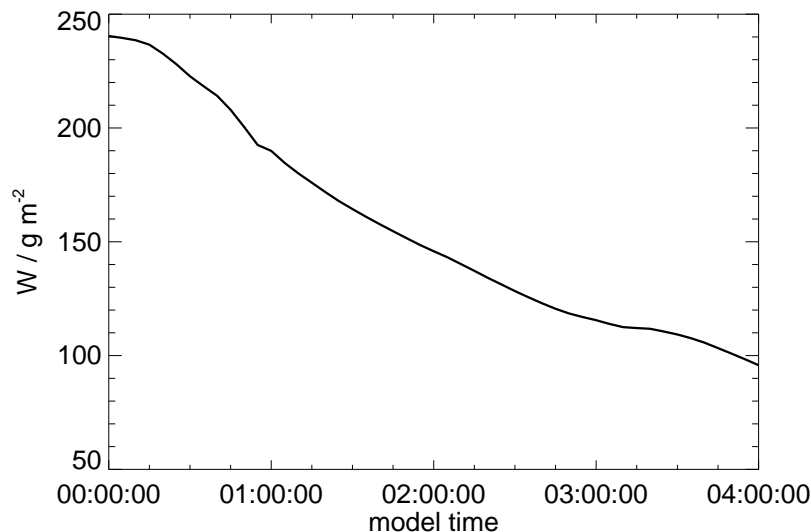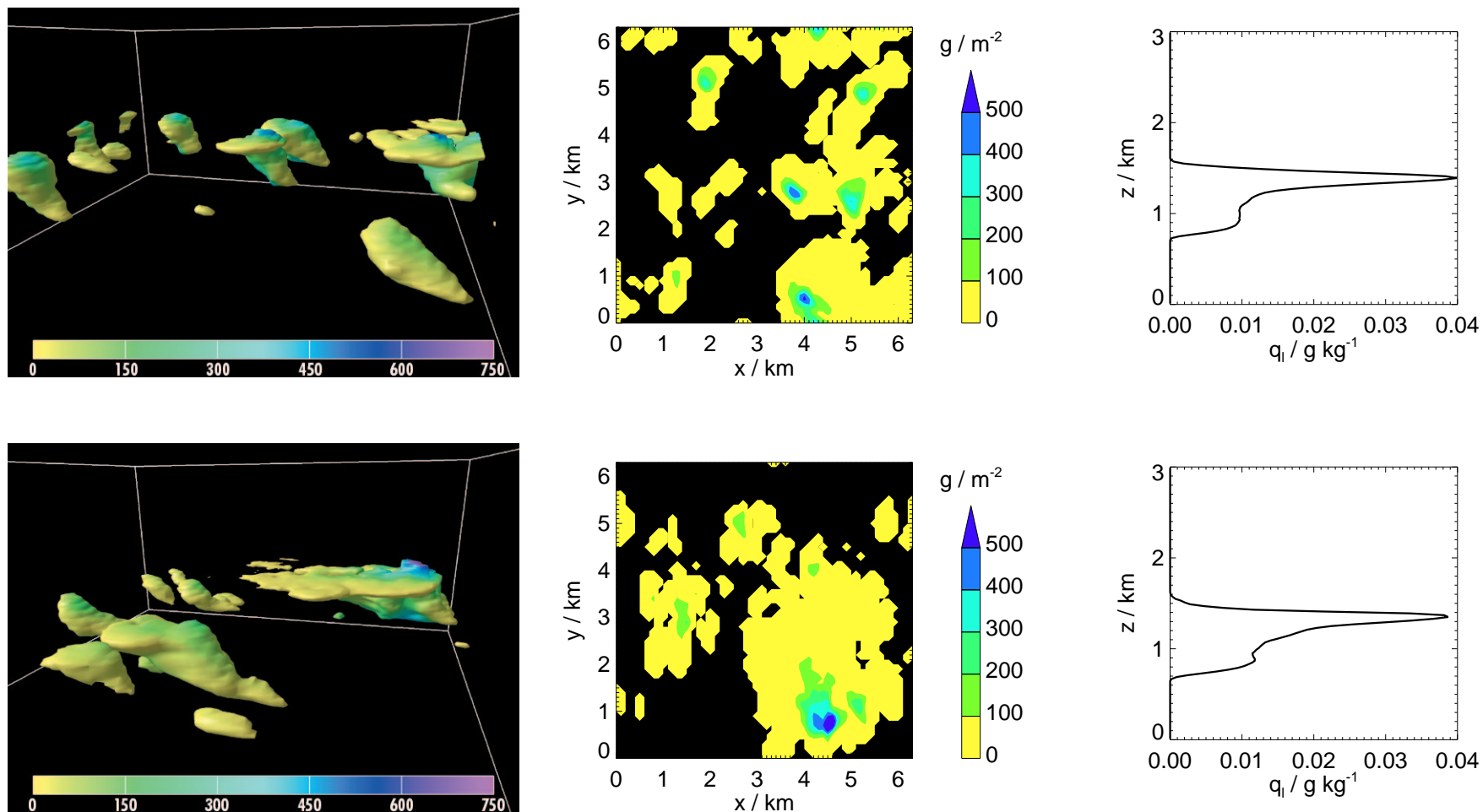
Figure 4.2: Evolution of the liquid water path of the ASTEX cloud simulation. The first 30 min are model spin-up and are therefore not used in the radiation computations. One can clearly see a drying out of the cloud, caused by entrainment of dry air.

The boundary-layer top rises from 705 m to 785 m, while the liquid water path decreases during the course of the model integration (see Figure 4.1.2). Nevertheless the cloud forms a solid deck with cloud cover $A_c \equiv 1$ throughout the whole simulation.

4.1.3   Trade Wind Cumuli (ATEX)

Another intercomparison study, set up by the Global Water and Energy Experiment (GEWEX) Cloud System Studies Working Group 1 (GCSS-WG1), was dedicated to the low-level trade wind regime (Stevens et al., 2001). Initial and boundary conditions for an 8 h-simulation were constructed from the data collected during the *Atlantic Trade Wind Experiment (ATEX)*, which took place in February 1969 (e.g. Brümmer et al., 1974). Three ships drifted in the Atlantic northeast trade wind region (near 12° N, 35° W) for nearly three weeks and measured atmospheric properties by deck-level observations, radiosondes and RADAR as well as supplemental buoys. The initial conditions for the model simulations were deduced from the first part of the experiment. Horizontally homogeneous fields of temperature and humidity were prescribed, according to the radiosonde soundings. Their equability was again disturbed by introducing pseudorandom fluctuations in the initialization of the temperature and this time also liquid water field without altering the domain averages. The initial winds and their geostrophic values were drawn from reanalysis. After a model spin-up, forcings associated with hypothetical large-scale processes and advective tendencies due to subsidence were imposed.

Figure 4.3 shows the general structure of the simulated cloud field (compare to Fig-

Figure 4.3: Snapshots of the ATEX cloud simulation for 2 h (top panel) and 7 h 30 min (bottom panel) model time. Shown are volume surface plots, colored by the liquid water path (left), the liquid water path (center) and vertical profiles of the mean liquid water content (right)
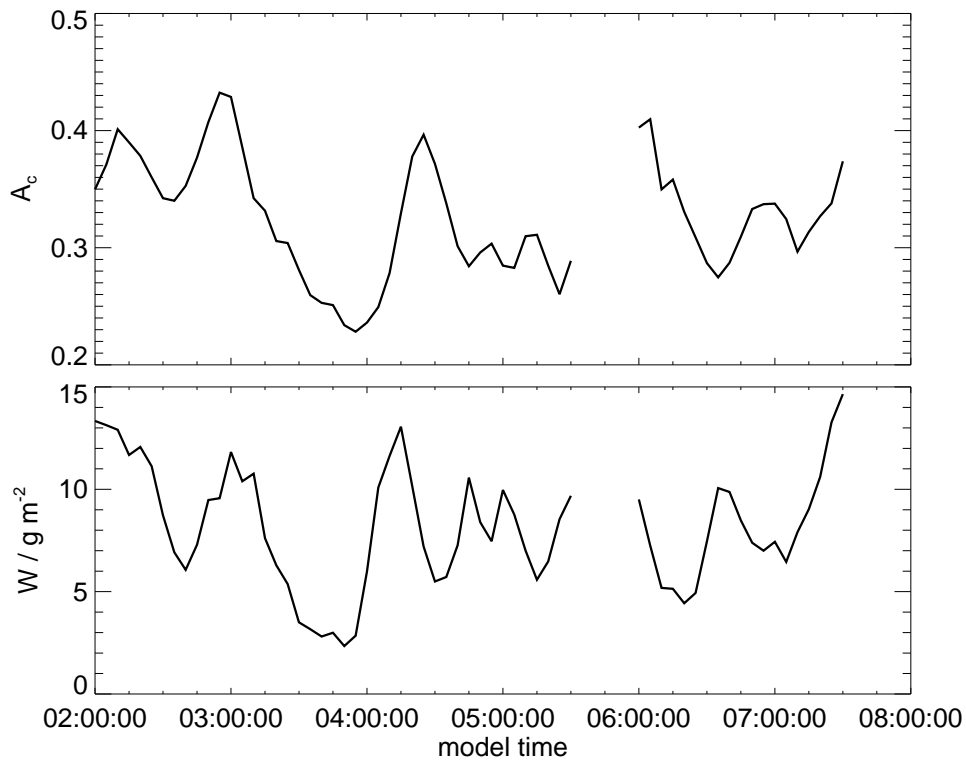
Figure 4.4: Evolution of total cloud cover and liquid water path of the ATEX cloud simulation. The first 2 h are model spin-up and are therefore not shown here. They are not used in the radiation computations, either. The data between 5 h 30 min and 6 h model time are corrupted as are the data for the last 30 min.

ure 4.1). The model domain for this integration is $6.4 \times 6.4 \times 3.0\,\mathrm{km}^3$, where the horizontal grid spacing is $\Delta x = \Delta y = 100\,\mathrm{m}$ and the vertical $\Delta z = 20\,\mathrm{m}$. Output is written every 5 min. The first two hours of model integration are discarded as model spin-up time. To get an impression of the time evolution Figure 4.4 shows the mean liquid water path and total fractional cloud cover.

4.2 Radiation Computations

In order to determine the optical properties of the cloud data described above, the short-wave radiation scheme of the ECHAM4 climate model has been extracted and rewritten as a standalone model for ICA and PPH computations. The details will be given in the next section, followed by the effects of the correction methods, which have been introduced in Chapter 3: Effective Thickness Approach and Gamma Weighted Two-Stream Approximation (uncorrected and corrected for correlation). All radiation model simulations shown below are performed assuming no aerosol loading and a standard concentration of carbon dioxide of $5.4 \cdot 10^{-4}\,\mathrm{kg/kg}$. Therefore clouds are the only scattering objects (apart from

Rayleigh scattering), which simplifies interpretation. If one wants to compare the modeled fluxes to measurements, of course also aerosols would have to be accounted for. The droplet number density is parameterized for maritime surface (see also Roeckner et al. (1996)) and the ground albedo is set to zero. There are no surface effects. The ocean albedo is low, so since both cloud simulations are for maritime cloud systems these parameter settings are consistent with the boundary conditions of the LES model.

4.2.1   Determination of the PPH-Bias

In the general introduction to this work in Chapter 1 we have seen that the non-linearity of reflectivity and transmissivity as functions of optical thickness leads to systematic deviations of the means for a field of cloudy pixels from corresponding values computed from the field's mean state. This straightforward implication of Jensen's inequality (Jensen, 1906) is proven empirically in the following section. The ICA computation serves as the reference method and comparison of the ICA-results to the corresponding PPH-values reveals the PPH-bias.

The ICA can be implemented quite easily: The data from the cloud resolving model, as described in the previous section, are read column by column. The cloud fraction for each pixel i is $A_c^i = 0$, when the liquid water mixing ratio is under a threshold value $q_l < q_l^{\text{thresh}}$, and $A_c^i = 1$, if $q_l > q_l^{\text{thresh}}$. For the following analysis this threshold has been set to $q_l^{\text{thresh}} = 10^{-3}$ g/kg in accordance with Petch and Edwards (1999). The effective radius r_{eff} and the optical properties τ, $\tilde{\omega}$ and g are computed as discussed in Section 2.2. Since r_{eff} is a function of the liquid water mixing ratio (see (2.49)) this means in particular that not only the liquid water content, but also the effective radius is horizontally inhomogeneous and both influence the variability of the optical thickness, single scattering albedo and asymmetry factor. A standard two-stream radiation computation is then performed for each column, as described in Section 2.1.2. Finally the fluxes for the individual columns are added up and divided by the number of columns to obtain the scene averages.

The plane parallel counterpart is constructed by reading in the data of each model layer and work out the algebraic mean of the atmospheric state variables. The cloud fraction is determined similarly as for the ICA experiment: All pixels with liquid water mixing ratio $q_l > q_l^{\text{thresh}}$ are counted as cloudy. The cloud fraction in level i then simply is $A_c^i = n_{\text{cd}}^i / n_{\text{tot}}$, where n_{cd}^i is the number of cloudy pixels in level i and n_{tot} is the total number of pixels per level. For partial cloudiness the maximum-random overlap assumption is applied. A single two-stream radiation computation, identically to the one performed for an individual column in the ICA, is carried out, immediately supplying the PPH fluxes.

The results for the ATEX and ASTEX clouds are presented in Figure 4.5 as functions of the solar zenith angle, represented by its cosine μ_0. Therefore the complete time series of the cloud experiment have been used, conducting separate ICA and PPH computations
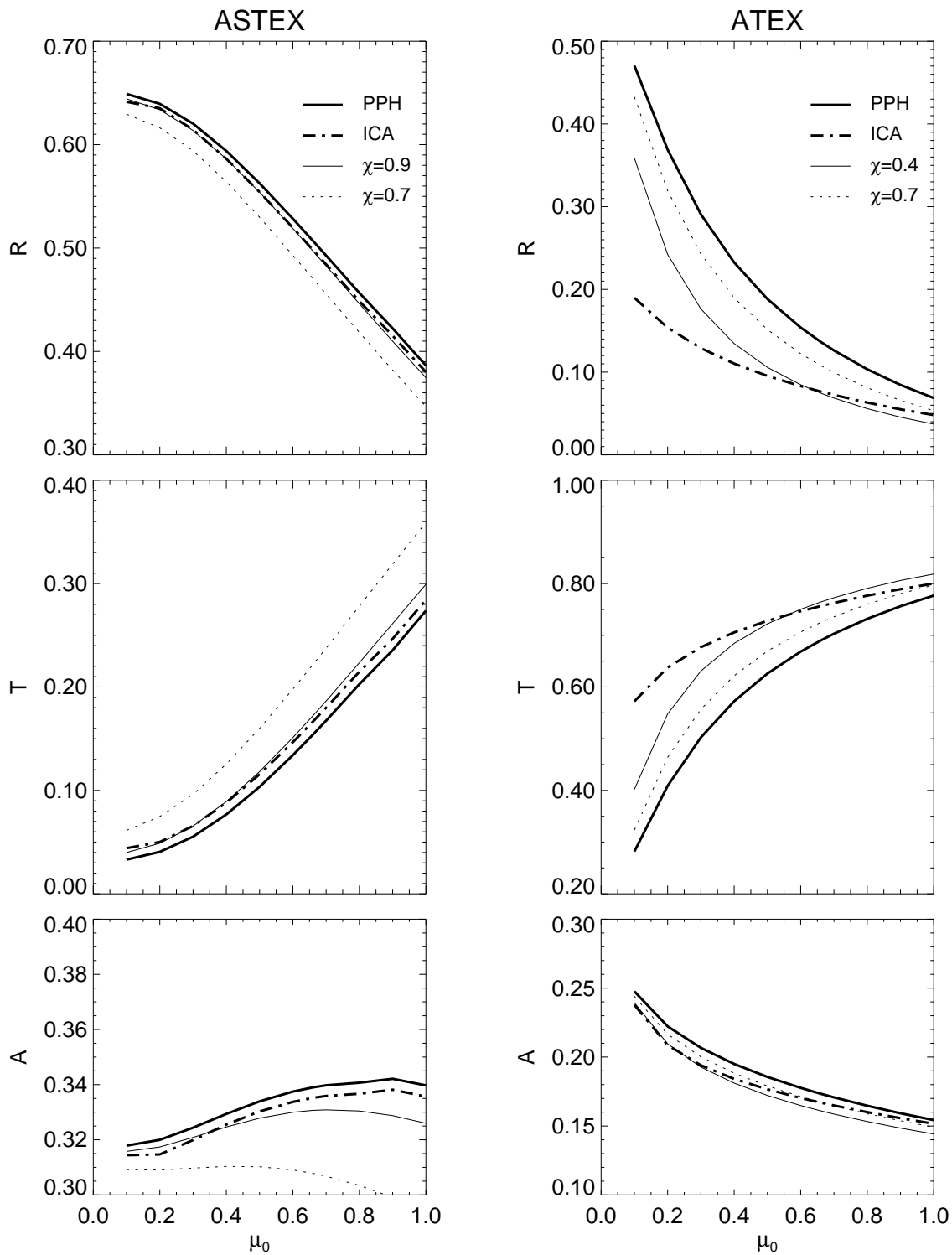
Figure 4.5: Reflectivity, transmissivity and absorptivity of the ASTEX (left) and ATEX (right) cloud simulations as functions of the cosine of the solar zenith angle. Standard PPH approximation and reference ICA calculation are plotted in thick solid and dashed-dotted, respectively. The curves computed by the ETA are shown in thin lines for various scaling factors χ.

for each time-step and averaging the fluxes afterwards. In both cases the reflectivity and absorptivity computed with the PPH approximation are always larger than the corresponding ICA value, while the transmissivity is smaller. This is exactly as expected from the general considerations in Chapter 1. Comparing the results for the trade wind cumuli of the ATEX simulation with the ones for the stratocumulus in ASTEX the PPH-bias is substantially larger in the inhomogeneous ATEX case than in the rather flat ASTEX cloud: The relative error defined as $(R_{\mathrm{PPH}} - R_{\mathrm{ICA}})/R_{\mathrm{ICA}}$ comes close to 100% for ATEX, while it is only around 5% in the ASTEX case. This could be expected qualitatively from the variability of the liquid water path in Figure 4.3, where the ASTEX cloud looks very much like a plane parallel homogenous slab of cloud, while the ATEX clouds are highly variable in shape and thickness with a much broader range of LWP-values.

In the description of the ICA method in Section 2.3.2 it was already mentioned that it is not adequate for oblique incidence. Therefore the values for low μ_0 in Figure 4.5 should be treated cautiously. In the following the discussion will concentrate on the results obtained at an intermediate solar zenith angle of $45°$ if not stated otherwise. This serves as an approximation of the mean results. If the explicit solar zenith angle dependency is needed, additional experiments are necessary. For our purpose of deriving a correction method for a GCM, the mean energetic correction is especially relevant. Furthermore, the ICA method is not applicable for low sun angles, so a different reference method such as Monte Carlo is required. The R, T and A values for ICA and PPH calculations are shown for each time-step in Figure 4.6. On the abscissa the mean optical thickness of the cloudy columns in that particular time-step is given. The relative PPH-bias remains approximately constant for all optical thicknesses. This is different from Figure 4.5, which may seem surprising at first sight: The cosine μ_0 enters the radiative transfer equation when computing the geometrical path length l from the layer thickness z as $l = z/\mu_0$. Reducing μ_0 therefore is synonymous with increasing z. However, there is a major difference: The incident solar zenith angle is only applicable for direct radiation, whereas for the diffuse part, i.e. radiation which has undergone at least one scattering event, an effective cosine of μ_{diff} is used (2.60).

An interesting feature is that the absorption as simulated by the ICA is smaller than its PPH counterpart. This stems from Jensen's inequality, since absorptivity is a non-linear function of optical thickness, and is also caused by the changes in the effective radius, which in turn affect the single scattering albedo and thus absorption. In recent years a discussion of the so called *'anomalous absorption'* or also *'enhanced absorption'* (Stephens and Tsay, 1990) has become very active again, triggered by the publication of Cess et al. (1995). They found that the absorption within clouds is substantially larger than simulated by current radiation schemes and postulated a "missing physics". A lot of debate has evolved discussing the existence and possible explanations of this difference. While some find similar results (Ramanathan et al., 1995; Pilewskie and Valero, 1995), others do not see any enhancement at all in their observations (Francis et al.,
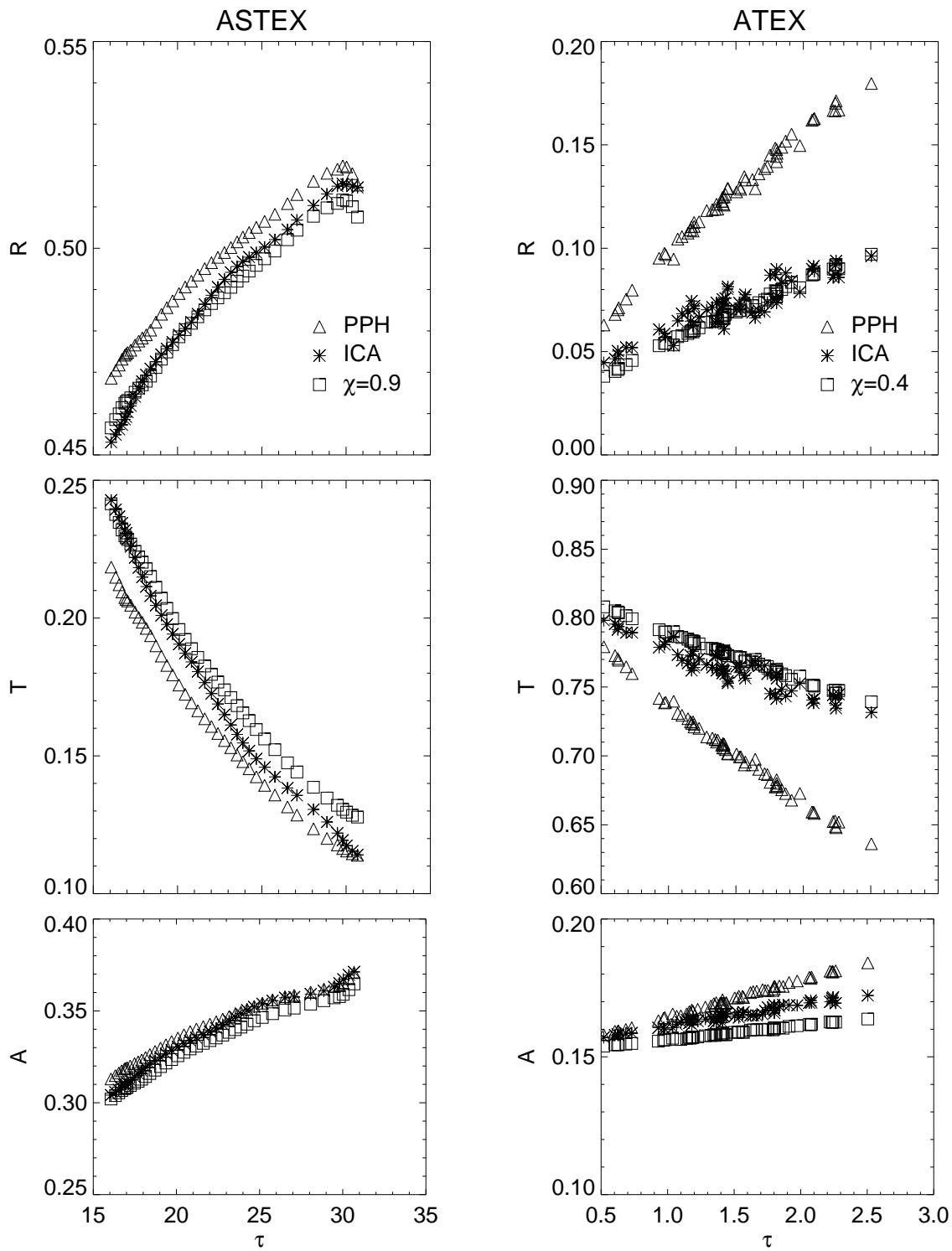
Figure 4.6: Reflectivity, transmissivity and absorptivity of the ASTEX (left) and ATEX (right) cloud simulations as functions of the mean optical thickness of the cloudy pixels. Standard PPH approximation and reference ICA calculation are plotted along with the best fit ETA with $\chi = 0.9$ (ASTEX) and $\chi = 0.4$ (ATEX).

1996, 1997) or interpret it as an aerosol effect (Li, 1997; Li et al., 1998) or a clear sky phenomenon (Arking et al., 1996; Arking, 1996; Li et al., 1998). Furthermore the measurement techniques and evaluation methods are suspected to generate an artificial absorption (Imre et al., 1996; Barker and Li, 1997). Repeatedly, 3D effects have been suggested as a possible explanation: Current radiation models underestimate the photon path length, because cloud variability is neglected (Byrne et al., 1996; Marshak et al., 1998; Kondratyev et al., 1998) or complex interaction of gaseous absorption, cloud droplet absorption, and the solar zenith angle are not correctly accounted for (O'Hirok and Gautier, 1998). These effects can however not be revealed by the experiments described in this section, since information about cloud geometry and real three-dimensional photon transport would be necessary. All correction approaches we will introduce below cannot be expected to account for such model errors, since they are developed with the ICA results as reference. Furthermore changes in absorption are relatively small. Accounting for any anomalous absorption feature would have to be done by another approach, e.g. scaling the single scattering albedo (Cairns et al., 2000).

4.2.2   Effective Thickness Approach

After we have identified the PPH-bias for the highly resolved cloud model data we will try to apply various correction approaches as they have been described in Chapter 3. To start with the simplest we try to find the appropriate reduction factor in the effective thickness approach, discussed in Section 3.1.

First we will test whether the universal reduction factor $\chi = 0.7$, as it has been derived by Cahalan et al. (1994), is applicable. The radiation code used for the PPH calculation has been modified such that the optical properties of the PPH averaged atmosphere are computed in the same manner as before. But instead of the original optical thickness, τ, the reduced, $\chi\tau$, is passed to the Delta-Eddington module. Asymmetry factor, g, and single scattering albedo, $\tilde{\omega}$, remain unchanged. For the ASTEX and ATEX model data the results are depicted in Figure 4.5 as long dashed curves. If we compare those to the PPH computations a reduction in reflectivity and absorption and an increase in transmissivity can clearly be seen. It is the immediate result of thinning the clouds by reducing τ. But there is an important difference between a cloud with smaller liquid water amount and scaling the optical thickness: The former would also have smaller droplet radii and therefore higher single scattering albedo, which additionally would influence the radiative properties, while the scaling *only* reduces optical thickness. Since the parameterizations for the effective radius (2.49) are empirical and furthermore reflect a physical, measurable property of the cloud, we only alter *one* attribute in order to make interpretation of the results easier.

By comparing the ICA and the ETA curves in Figure 4.5 it is obvious that the reduction factor of 0.7 is not adequate for either cloud: While the reflectivity is still too high in the

simulation	full res.	levels of single cloud layer interp.[m]
ATEX	20 m	20, 40, 500, 2980, 3000
ASTEX	25 m	25, 50, 500, 1475, 1500

Table 4.1: Level heights of the interpolated data sets with only a single cloud layer. The original resolution is given for comparison. The bottom and top levels remain unchanged in order to avoid inconsistencies at the boundaries.

ATEX case it has become too small in the ASTEX case and analogously for absorption and transmission (absorption too high in ATEX and too low in ASTEX, transmission too low in ATEX and too high in ASTEX). This is not surprising when we remember the limitations of the effective thickness approach as stated in Section 3.1: The ATEX cloud simulation is much more variable than the marine stratocumulus, which was investigated by Cahalan et al. (1994) when deriving the reduction factor $\chi = 0.7$. Therefore the factor for this cloud should be smaller. The converse is true for the very homogeneous nocturnal stratocumulus of the ASTEX case. More variability could be expected for a daytime simulation with solar radiation acting as an additional forcing for convective events as was the case in the measurements used by Cahalan et al. (1994). Hence, a reduction factor larger than 0.7 is reasonable. We will try to find the optimal reduction factors for these two cloud simulations.

The vertical resolution of current GCMs is much coarser than the one of the CRM simulations. In order to avoid this inconsistency the cloud data are interpolated to a new set of vertical levels such that the clouds reside completely in a single level. The new level heights are given in Table 4.1. The level thickness now is comparable to that of large scale models. Furthermore, the basic studies in Chapter 3 used single layer cloud data, either from a model or satellite, so the interpolated version is closer to their conditions.

For the ATEX cloud this interpolation does not change the radiation values for PPH and ICA as can be seen from Figure 4.8. The prefix "F" stands for "full" resolution of the LES model and "S" for single cloud layer. (For an overview of the experiments see Table 4.2.) In the ASTEX case, however, there are differences of up to 2% in reflectivity and up to 4% in transmissivity between the radiation computed for the original data set and the interpolated version. Contrary to the ATEX case for this stratocumulus cloud it is important to get the top boundary as precise as possible. Since fixed level heights were chosen, but the inversion level is sinking during the simulation (see data description in the previous section), the vertical extent of the interpolated cloud is much larger. Nevertheless the relation between ICA and PPH remains the same.

By the vertical interpolation any information about the vertical structure within the clouds are lost, which may be a reason for differences in the radiative fluxes. We will try to separate vertical and horizontal variability effects in the full resolution data set by homogenizing the clouds. This is sketched in Figure 4.9. For each layer i the mean liquid
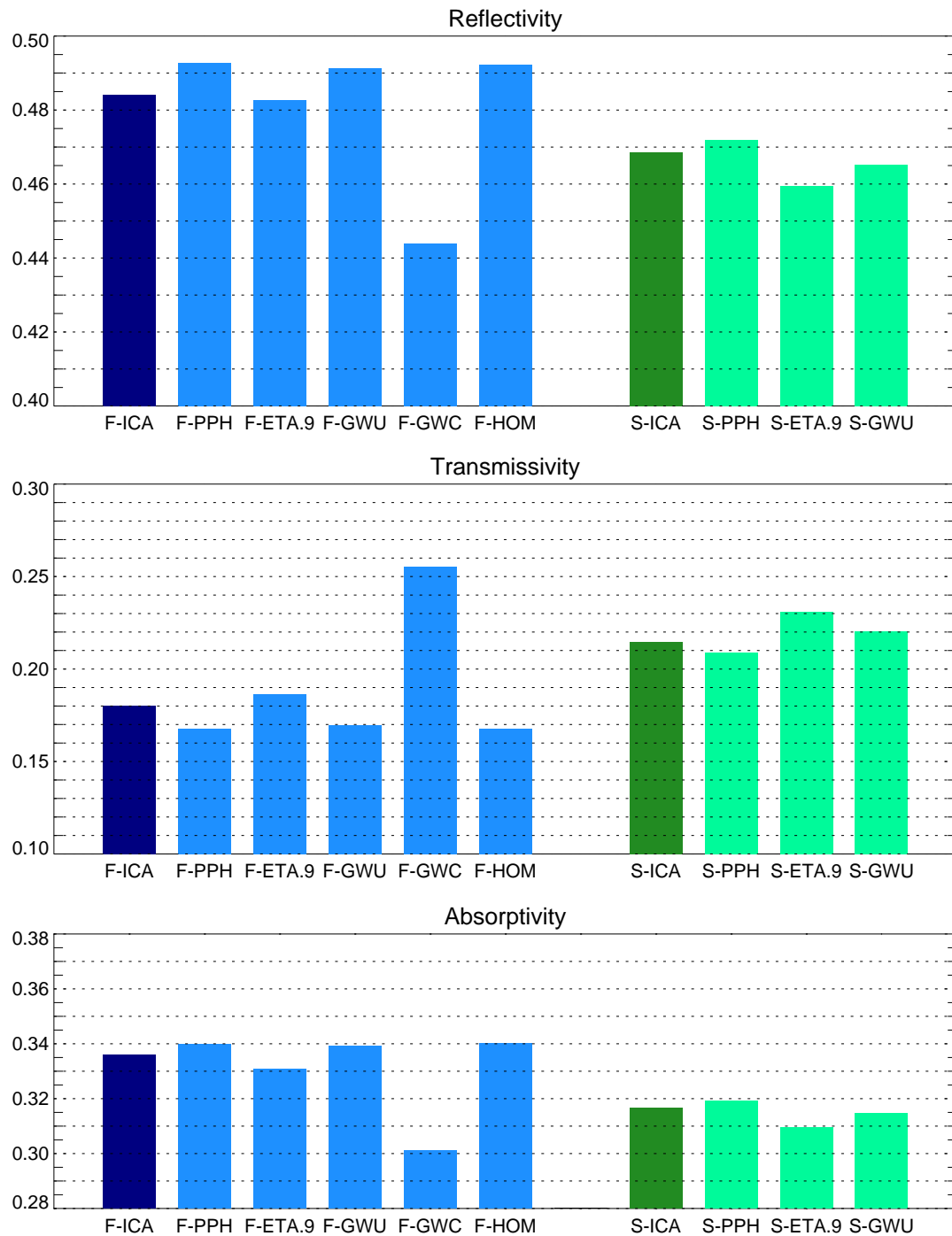
Figure 4.7: Reflectivity, transmissivity and absorptivity of the ASTEX cloud simulation using different techniques. All values are computed for an incident zenith angle of 45° and are averages over all time-steps. The labels are explained in Table 4.2.
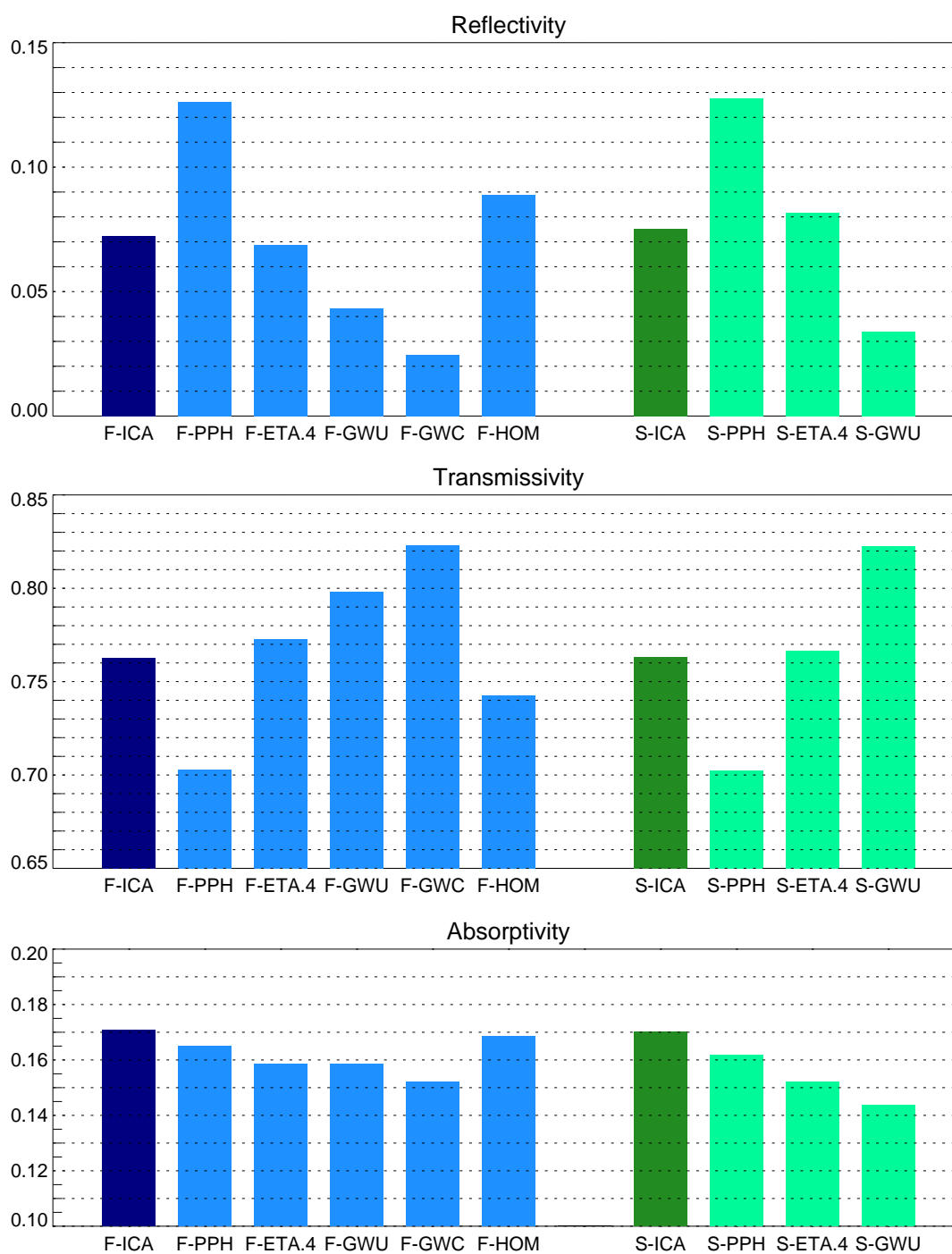
Figure 4.8: Reflectivity, transmissivity and absorptivity of the ATEX cloud simulation using different techniques. All values are computed for an incident zenith angle of 45° and are averages over all time-steps. The labels are explained in Table 4.2.

label	description
F-ICA	ICA computation; full vertical resolution
F-PPH	PPH computation; full vertical resolution
F-ETA.9	ETA computation; reduction factor $\chi = 0.9$; full vertical resolution
F-ETA.4	ETA computation; reduction factor $\chi = 0.4$; full vertical resolution
F-GWU	GWTSA computation; no correlation correction; full vertical resolution
F-GWC	GWTSA computation; correlation correction applied; full vertical resolution
F-HOM	ICA computation; levels homogenized; full vertical resolution
S-ICA	ICA computation; interpolation to single cloud layer
S-PPH	PPH computation; interpolation to single cloud layer
S-ETA.9	ETA computation; reduction factor $\chi = 0.9$; interpolation to single cloud layer
S-ETA.4	ETA computation; reduction factor $\chi = 0.4$; interpolation to single cloud layer
S-GWU	GWTSA computation; no correlation correction; interpolation to single cloud layer

Table 4.2: Overview of the radiation computations performed with the CRM datasets.
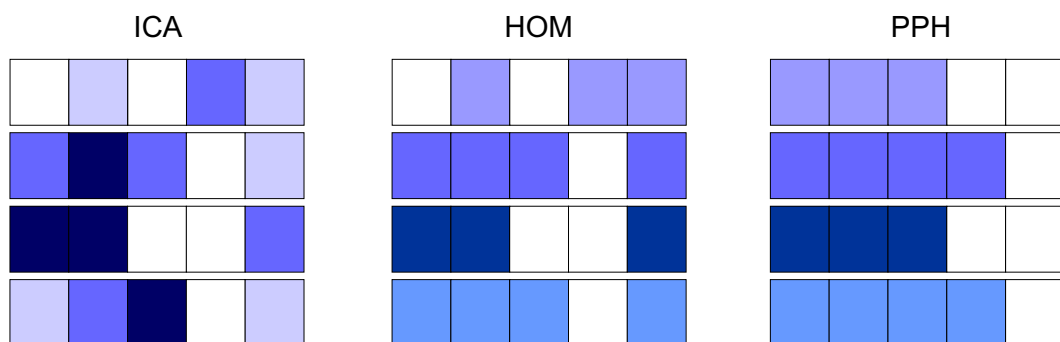
Figure 4.9: Sketch of homogenized cloud data (HOM) compared to the original data (ICA) and the plane parallel homogeneous equivalent (PPH). All cloudy pixels of the original dataset are in the HOM version defined with the mean value of liquid water mixing ratio of the corresponding layer.
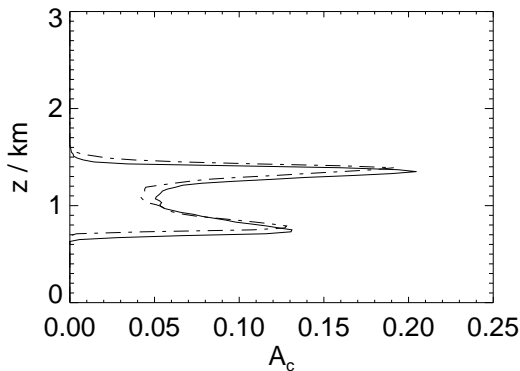
Figure 4.10: Profile of fractional cloud cover of the ATEX simulation for model time 2 h (solid) and 7 h 30 min (dashed). See also Figure 4.3.

water contents inside clouds $\overline{q}_{l,i}$ is computed. All cloudy pixels are then defined with this mean liquid water content, while all other atmospheric parameters remain unchanged. ICA computations may be performed for this rewritten dataset, where no horizontal variability within the cloudy part in any single layer is present while the vertical structure is preserved. The results are shown in Figure 4.7 and Figure 4.8 with label "HOM". In the ASTEX case the HOM computations are identical with the PPH, which means that the difference to the ICA stems completely from horizontal inhomogeneities. This could be expected, since the cloud cover of the ASTEX stratocumulus is either 1 or 0, therefore the cloud overlap assumption has no effect. The reverse is true for the ATEX cloud. From the cloud cover profiles in Figure 4.10 one can expect an influence of the assumptions about overlap and indeed the HOM results are quite different from the PPH computations. The maximum-random overlap seems to produce an overall cloud shape which is close to the vertically interpolated version — the differences between F-PPH and S-PPH are negligible — while the HOM method introduces more horizontal variability, when we look at the total liquid water path over the whole vertical extension of the cloud. Petch and Edwards (1999) and Petch et al. (1999) reported different results. They found that HOM reflectivities are larger than the ones for PPH calculation, when maximum-random overlap is applied. But their LES model domain extended up to 20 km with a vertical resolution of 300 m, so their levels represented distinct clouds and cloud types (like low lying shallow convection clouds, overlayed by thin cirrus). For the high resolution data of the current study the interpretation is not so straight forward, since the level boundaries cut through small turbulence elements, mixing the influence of vertical structure and horizontal inhomogeneity.

In order to determine the cloud specific reduction factors we try to use directly the relation between the mean logarithm of liquid water path, the mean of the logarithm and the reduction factor from (3.3), which can be rewritten as

$$\chi = \frac{\exp\left(\overline{\log W}\right)}{\overline{W}}. \tag{4.1}$$

For the ASTEX stratocumulus cloud this yields reduction factors between $\chi_i = 0.93$ and $\chi_i = 1.0$ for the individual time-steps with a mean of $\chi = 0.94$. If we take all time-steps
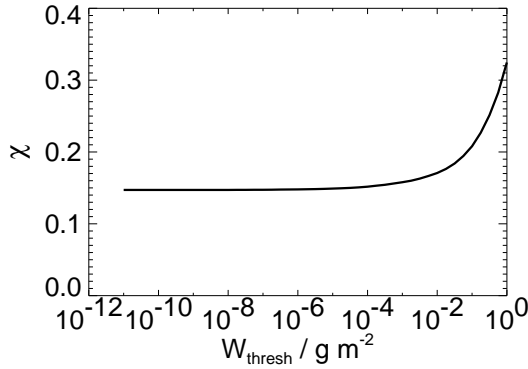
Figure 4.11: Scaling factor χ of the ETA computed for the ATEX cloud data using (4.1) vs. the threshold value W^{thresh} of the LWP. Pixels with $W < W^{\mathrm{thresh}}$ are regarded clear sky.

as representation of a bigger cloud field with different stages of a stratocumulus cloud at the same time, resulting in a virtual domain size of $28 \times 195\,\mathrm{km}^2$, we get $\chi = 0.90$, which is smaller than that for the individual time-steps since the overall variability is larger. Whatever value we choose, it is substantially higher than the 0.7 used before in accordance with Cahalan et al. (1994). Figure 4.5 (left panel) shows the reflectance, transmittance and absorptance of an ETA experiment with $\chi = 0.9$ as thin solid line. It is in quite good agreement for high μ_0. For lower cosine, i.e. low standing sun, the question is, whether the ETA fails or the ICA is no longer valid, so that the upper μ_0-range is more informative. Furthermore, it is most important from an energetic point of view, because the absolute energy correction is largest for high standing sun ($\mu_0 \sim 1$). Monte Carlo simulations or other methods as discussed in Section 2.3 would have to be applied to investigate the deviation at small μ_0. For a solar zenith angle of $45°$ the agreement is good for all optical thicknesses as can be seen in Figure 4.6 and the overview graph Figure 4.7 (left panel), where again both vertical resolutions are shown. For the single cloud layer version the reduction factor of $\chi = 0.9$ still seems to be too small, whereas for the full resolution it agrees quite well with the ICA computation, but the optical thickness is still slightly underestimated, thus, $0.9 < \chi < 1.0$.

For the ATEX case (4.1) cannot be applied directly: Because the $\log(W)$ at $W = 0$ is not defined, we have to set a threshold for the lowest liquid water path regarded as cloudy. Using the threshold value for liquid water content from the ICA computations $q_l^{\mathrm{thresh}} = 10^{-3}\,\mathrm{g/kg}$ results in a threshold for liquid water path of $W^{\mathrm{thresh}} = 22 \cdot 10^{-3}\,\mathrm{g/m}^2$ and thus finally leads to a reduction factor of $\chi = 0.16$, computed as the mean over all time-steps. Since W^{thresh} is not physically based, it is interesting to ensure that χ does not depend on the choice of this threshold value. Figure 4.11 shows the reduction factor (again mean over all time-steps). The reduction factor computed by (4.1) is far from being independent of W^{thresh}. For $W^{\mathrm{thresh}} < 10^{-4}\,\mathrm{g\,m}^{-2}$ the curve saturates at $\chi = 0.15$. The corresponding reflectivity can be seen in Figure 4.12. It is much too low, i.e. the reduction factor of 0.15 is too small. For broken clouds the relation (4.1), which was developed for overcast stratocumulus cloud decks, cannot be applied.

Despite this deficiency we still may try to apply the general idea of the ETA also to the

ATEX data. Since straightforward computation of χ via (4.1) fails, we will try to derive a reduction factor empirically by performing ETA computations using reduction factors from $\chi = 0.1$ to $\chi = 0.9$ ($\Delta\chi = 0.1$) and comparing the results to the ICA value. In Figure 4.12 the reflectivities for solar zenith angles of $0°$, $45°$ and $60°$ are plotted as functions of the reduction factor along with the reference reflectivities from the ICA computations. For $\theta = 45°$ we may deduce $\chi \approx 0.4$, but the range of χ extends from ≈ 0.3 at $\theta = 60°$ to ≈ 0.6 for $\theta = 0°$. Thus, $\chi = 0.4$ can only be regarded as an average value, which is reasonable for energetic considerations, but unsuitable for the comparison of model results to measurements. It is beyond the scope of this study to derive a zenith angle dependent parameterization for χ, because the latter certainly is influenced by the 3D cloud structure, so a larger set of cloud simulations is required and methods like Monte Carlo are more adequate for this kind of investigation. The radiative properties corresponding to the ETA computation with this reduction factor are plotted in Figure 4.5. Figure 4.8 shows the values for both the full and single cloud layer vertical resolution. For the deviations, especially for small cosines of zenith angle, the same arguments as for the ASTEX case apply. So the ETA appears to be a reasonable correction also for the broken clouds of the ATEX simulation using a reduction factor of $\chi \approx 0.4$. Similar results have been obtained by Kogan et al. (1995). They found a reduction factor of $\chi = 0.5$ for an LES simulated cumulus cloud field.

The absorption is of course smaller in the ETA computation than it is in the PPH case, because the clouds are virtually thinned out. It is even smaller than, but comparable to the ICA case. Returning to the discussion of anomalous absorption mentioned above, the ETA would make the situation even worse. Other correction methods need to be engaged if both the albedo bias and enhanced absorption should be accounted for, like modifying both, optical thickness *and* single scattering albedo (Cairns et al., 2000).

In summary, the effective thickness approach could be shown to be an adequate correction method for albedo and transmissivity. The reduction factor strongly depends on cloud type and has to be determined for each cloud separately: For the homogeneous nocturnal stratocumulus cloud deck of the ASTEX case $\chi = 0.9$ gives good results, whereas for the broken trade wind cumulus clouds in the ATEX simulation optical thickness may be corrected with a value of $\chi = 0.4$. Merely using an unique constant of $\chi = 0.7$ therefore is clearly a crude simplification, which is of course the only possibility if no additional information about the cloud is available. In Section 5.4 various attempts to deduce some cloud characteristics form large scale variables like convection type or cloud thickness are presented.

4.2.3   Gamma Weighted Two-Stream Approximation

The reduction factor of the ETA depends on cloud type, as we have seen in the previous section. Cahalan et al. (1994) express this as a function of the fractal parameter of the
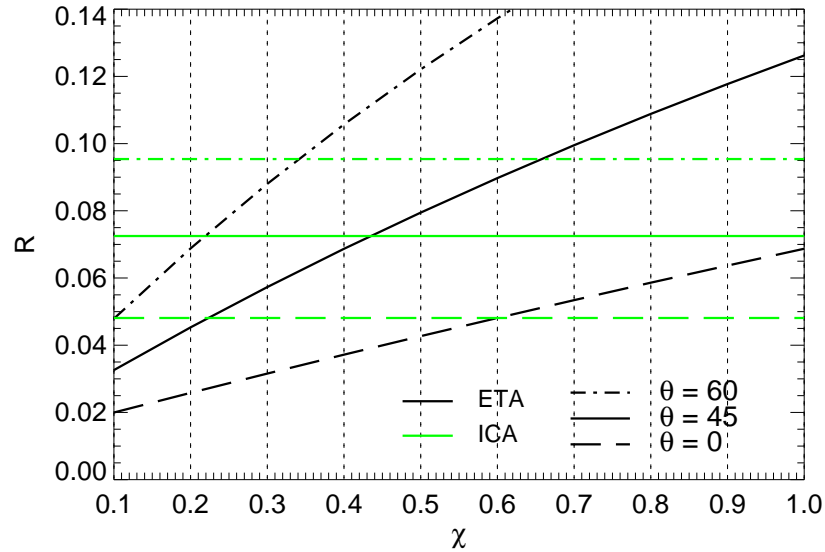
Figure 4.12: Reflectivity of the ATEX cloud data, averaged over all time-steps, as functions of the scaling factor χ for three solar zenith angles. The values of the reference ICA computations are marked by horizontal lines. From the intersection of the ICA line with the corresponding ETA curve the best fit scaling factors can be extracted.

bounded cascade cloud model. This means that the correction depends on some measure of variability, here the parameter f in (3.3). In the Gamma Weighted Two-Stream Approximation this additional information is introduced via the distribution width ν as defined in (3.14). It can be extracted directly from the cloud data. Therefore the mean liquid water path $\overline{W}$ and the variance $\text{var}(W)$ of one time-step of cloud data are diagnosed and $\nu = \overline{W}^2/\text{var}(W)$ is calculated from these first two moments of the distribution. This procedure is called the *Method of Moments (MOM)*. For the two time-steps used to introduce the data in Figure 4.1 the distributions and the fitted Gamma-distributions derived by the MOM are shown in Figure 4.13 and Figure 4.14 for the ASTEX and ATEX cases, respectively. Also noted are the corresponding values of ν. The distributions fit the general shape of the data, but show deviations especially for strongly peaked distributions. A striking difference between the two cloud simulations is that in the ASTEX case $\nu \geq 30$, which results in a nearly Gaussian shape, while for the ATEX clouds $\nu < 1$, corresponding to a strongly skewed distribution. For the latter the clear sky pixels have not been regarded. They would appear as a δ-like peak at $W = 0\,\text{g/m}^2$. Remembering the definition of ν in (3.14), small ν means high variability, whereas for $\nu \to \infty$ the distribution approaches δ-shape.

The value of ν computed by the MOM is passed to the GWTSA scheme. The reflectivities and transmissivities in the Fouquart scheme are no longer computed according to (2.29)–(2.30), the standard Eddington-approximation discussed in Section 2.1.2, but
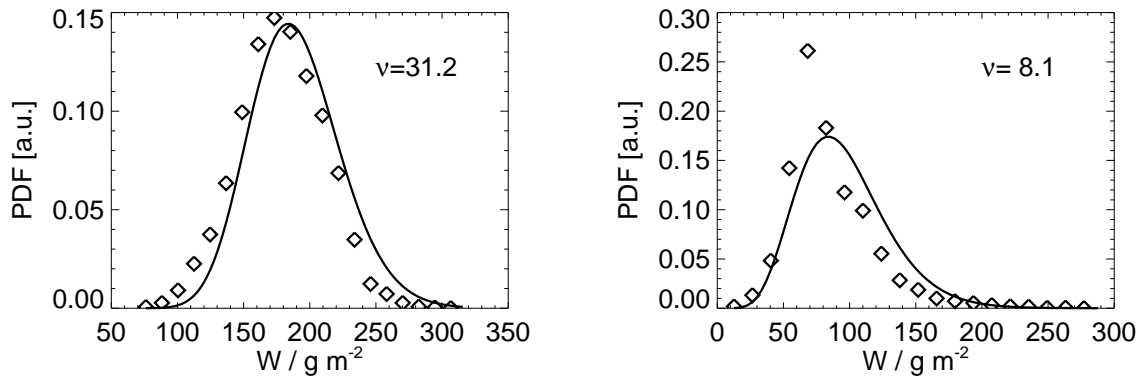
Figure 4.13: For the snapshots at model times 1 h (left) and 4 h (right) of the ASTEX simulation, which are shown in Figure 4.1, Gamma-distributions have been fitted to the probability distribution of the total liquid water path. The diamonds are extracted from the model data, the solid line is the Gamma-distribution fitted by the method of moments, using the width parameter ν as stated in each panel.

are substituted by (3.17)–(3.19), the corresponding formulas of the GWTSA. The results are again shown in Figure 4.7 and Figure 4.8 labeled "S-GWU". For both, ASTEX and ATEX, the GWTSA clearly reduces reflectivity and enhances transmissivity.

For the ASTEX cloud the GWTSA is nearly identical to the PPH for normal incidence and falls off below the ICA for low sun elevation. This may in part be attributed to the limited applicability of the ICA for small values of μ_0 and eventual deviations of the two-stream formulas used for the Delta-Eddington approach and the GWTSA. Nevertheless the GWTSA gives reasonable results for the homogeneous cloud, which is quite close to its PPH averaged counterpart.

In the highly variable ATEX case the correction introduced by the GWTSA is much higher. The reflectivity is even smaller than that of the reference ICA calculation. This implies that the fitted distribution is more inhomogeneous than the original cloud data, despite the reasonable fits shown in Figure 4.14, since there is no additional physical approximation introduced when going from ICA to GWTSA: Both assume that individual columns are independent, which means they can be resorted arbitrarily, e.g. according to their liquid water path. This is exactly what is done when plotting a histogram like in Figure 4.14. Deviations of the fit function are then immediately reflected in differences of the optical properties. Oreopoulos and Davies (1998b) discuss the problem of finding the best fit for a given cloud field and they use the Maximum Likelihood Estimate instead of the Method of Moments, which gives better results for the satellite data they investigated. On the other hand, Barker et al. (1999) find the distributions fitted by the Method of Moments to excellently agree with a different set of satellite retrievals. In the light of an eventual use of the GWTSA in a GCM it seems to be more appropriate to rely on the Method of Moments, since a climate model will not be able to model the details of a cloud
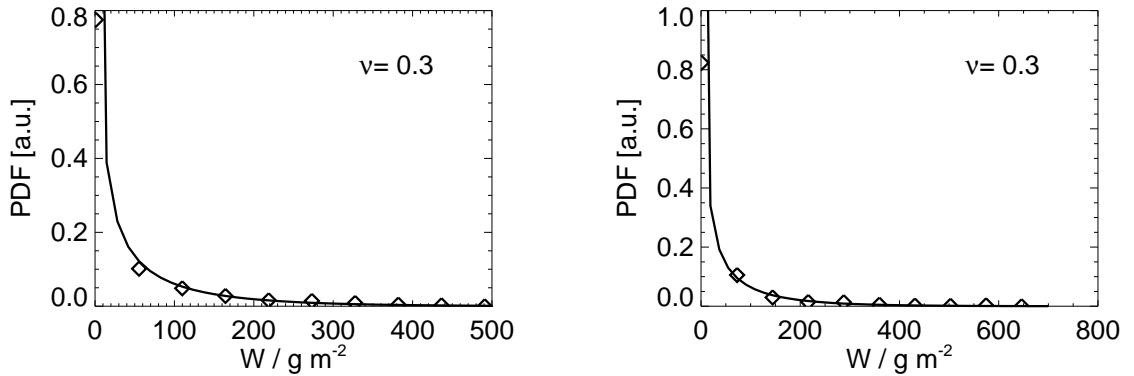
Figure 4.14: For the snapshots at model times 2 h (top) and 7 h (bottom) of the ATEX simulation, which are shown in Figure 4.3, Gamma-distributions have been fitted to the probability distribution of the total liquid water path. The diamonds are extracted from the model data, the solid line is the Gamma-distribution fitted by the method of moments, using the width parameter ν as stated in each panel.

field (as is done in a cloud resolving model), to which a distribution may be fitted, but can provide additional state variables, representing the higher order moments of the cloud water content within a grid cell. Therefore the question is, whether the Gamma-distribution is an adequate description for the probability distribution function of all cloud types. For the highly resolved cloud data of the ATEX simulation this is true only in parts: The fits look reasonable, nevertheless the deviations cause considerable errors in the radiation computation. Especially inconsistencies in the non-linear range of $R(\tau)$ lead to large discrepancies. This is in contrast to (Barker et al., 1996) and (Oreopoulos and Davies, 1998b), who find good agreement for the distribution of cloud optical thickness retrieved from satellite images.

In Section 3.2.1 an additional correction for multilayer clouds was described, which has been applied to the full resolution data set. The pure GWTSA gives similar results for both vertical resolutions, which can be seen by comparing the bars labeled "F-GWU" and "S-GWU" in Figure 4.7 and Figure 4.8. In the latter again the offset between the full resolution and single cloud layer version is present. This means that the Gamma-distribution also seems to be a good fit for individual cloud layers. For some arbitrary levels this is depicted in Figure 4.15 and Figure 4.16. It is interesting that for the ATEX case the variability parameter ν is smaller in the single cloud layer version (i.e. higher variability), which results in lower reflectivity. This is exactly what Oreopoulos and Barker (1999) have shown analytically. We may now implement the correction for the correlation of the water distributions in adjacent layers given by (3.28) with the parameter $\mathcal{A}_k \equiv 1$ and not as defined in (3.29), because this tuning is not necessary due to the implementation of the cloud overlap assumption in the Fouquart scheme. The results are also plotted in Figure 4.7 and Figure 4.8 and are labeled "F-GWC". The correction is even larger than in the
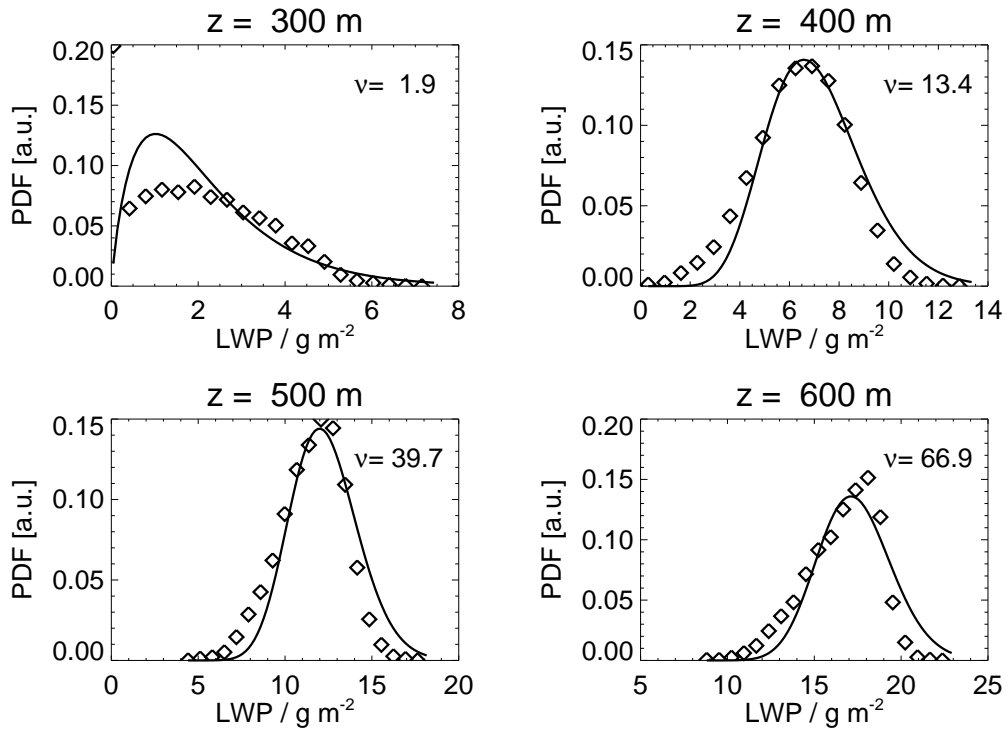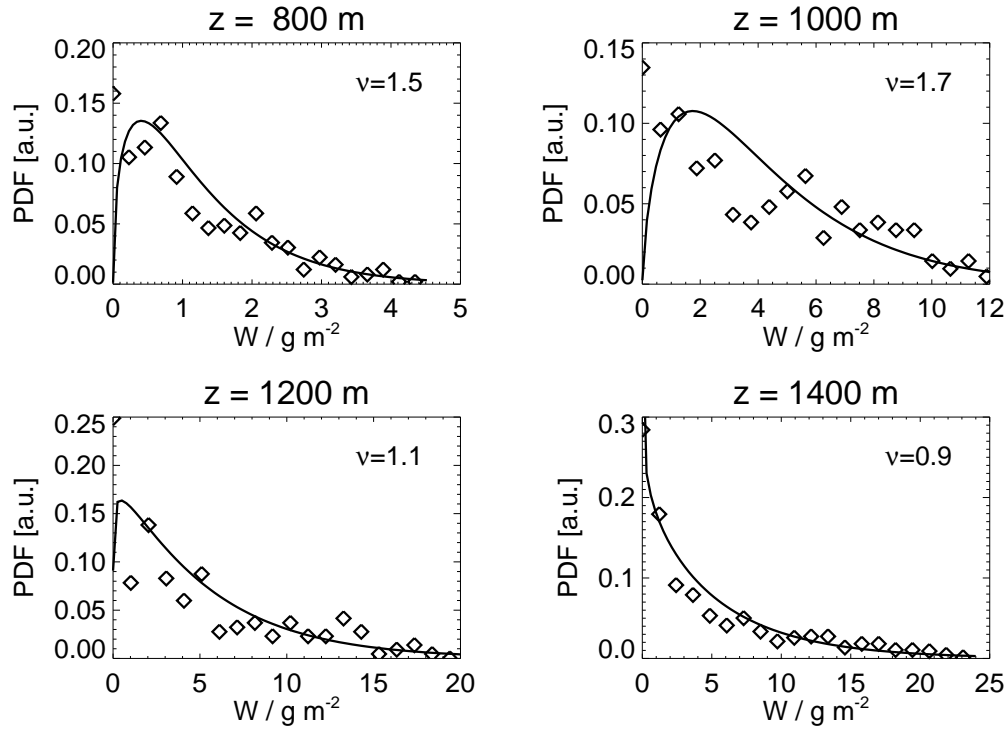
Figure 4.15: PDF of liquid water path for individual cloudy layers of the full resolution of the ASTEX simulation along with the fitted Gamma-distributions (2 h simulation time). The level heights and shape parameters are given for each plot.

GWU simulation, because the optical thickness of the lower layers is reduced, depending on the weakening of the incident radiation by the overlying layers according to (3.28). For the ASTEX case the effect is tremendous: The difference introduced by the correlation correction is several times larger than the initial GWTSA correction and drastically underestimates reflectivity and at the same time overestimated transmissivity. For the ATEX cloud, where the pure correction due to the Gamma-distribution was already quite substantial, the additional reduction in reflectivity (and the enhancement in transmissivity, respectively) caused by the scaled optical thickness is relatively smaller, but still relevant. It is even too strong in comparison to the S-GWU value. This result is important for all statistical schemes in a multilayer model, because the problem connected with correlation of optical thickness arises in all the schemes. The assumptions made in Section 3.2.1 which lead to (3.28), seem to be not completely adequate: First, the distribution width is not constant through all vertical levels as can clearly be seen from the ν-values given in Figure 4.15 and Figure 4.16. Second, the assumption of perfect correlation, as depicted in Figure 3.2 can be expected to be wrong as the clouds become vertically extended. Till now only a few studies have dealt with the vertical structure of clouds, since satellite based measurement techniques are not able to resolve the clouds vertically. Ground based instru-

Figure 4.16: PDF of liquid water path for individual cloudy layers of the full resolution of the ATEX simulation along with the fitted Gamma-distributions (1 h simulation time). The level heights and shape parameters are given for each plot.

ments like RADAR and LIDAR therefore have to be used, which have long time series, but on the other hand only have very limited fields of view. Nevertheless, from data like those presented by Hogan and Illingworth (2001) one might try to find a parameterization for the correlation issue. They show that even the cloud overlap problem, which is important on a much coarser scale, is badly represented by the maximum-random overlap assumption for growing distances of the cloudy layers. The correlation of the probability density functions can be expected to be smaller at longer distances. CRM data with larger domains and especially measurements of the cloud vertical structure are necessary to tackle this problem. Maybe the new discussion about cloud overlap assumption, which evolved recently in the literature, using new observational data (Wang et al., 2000; Stephens et al., 2000), testing the radiation fluxes one obtains by applying different overlap assumptions against observations (Petch and Edwards, 1999; Bergman and Hendon, 1998; Chou et al., 1998) or investigating the sensitivity of GCMs (Morcrette and Jakob, 2000; Collins, 2001), will help to solve the closely related correlation problem.

In summary, the GWTSA experiments using the highly resolved data from the cloud resolving model simulations showed that the statistical method in principle corrects the fluxes of the one dimensional radiation computation in the right direction. Its quantitative

performance, however, crucially depends on the correct shape of the probability distribution function. The results presented in this section did not substantiate the findings of Oreopoulos and Barker (1999), who used satellite data, in so far as the GWTSA computed reflectivity is too low when compared to the ICA (the uncorrected GWTSA-u was still too high in Oreopoulos and Barker (1999)) and the GWTSA-c simulations, which include an additional correction for the vertical correlation of probability functions in a multiple layers model, even further reduce reflectivity (and at the same time enhance transmissivity). It is interesting to note that the correction for correlation can have a significant contribution to the total correction of the PPH radiation fluxes, but on the other hand it therefore is important to find an adequate parameterization of this effect. Since the BWTSA is based on the same principle these results may directly be transfered.

4.3   Conclusions

If any information about the cloud variability like the standard deviation is known, statistical schemes like the GWTSA or the BWTSA, which we will further discuss in the following chapter, enable a consistent treatment of sub-grid scale inhomogeneity. The albedo modification of course depends on the choice of distribution. For individual cloud scenes, especially with small domain sizes, the distribution may deviate substantially from the observed or modeled one. Nevertheless, for a GCM with grid box sizes comparable to the satellite's field of view, the variability is described well enough in order to provide radiation correction of the right order of magnitude (Oreopoulos and Barker, 1999). The effect of correlated distributions in a multi-layer model are substantial. A treatment similar to that for the cloud overlap problem needs to be developed.

In the effective thickness approach reduction factors can be derived for each cloud scene such that the ETA fluxes agree very well with the reference computations. However, no unique value can be given, but the latter depends crucially on the internal variability of the cloud. A typical constant setting of $\chi = 0.7$ is appropriate only when no additional information about the cloud structure can be deduced. For some climate models this therefore serves as first order correction of the PPH-bias. Additional information about cloud inhomogeneity has to be supplied to the ETA scheme in order to adjust the reduction factor. This is synonymous to the statistical approaches. In principle, the GWTSA corrections can be expressed by an equivalent reduction factor. As long as only very coarse division of cloud characteristics is possible, e.g. convective vs. stratiform, the ETA is favorable, because it is easier to implement. Since parameterization of the distribution shape would then also be very crude, statistical schemes would merely reflect the uncertainty of determining the PDF.

Chapter 5

Climate Model Experiments

General circulation models (GCM) are one of the most important tools in climate research, since they offer the possibility to study the mechanisms of the climate system by conducting experiments with well defined boundary conditions. In contrast to numerical weather prediction models, climate models therefore have not only to well reproduce the current weather and climate, but have to rely as far as possible on fundamental physical processes. Otherwise conclusions drawn from model experiments for testing hypotheses are possibly artefacts of the chosen parameterization. The same is true for climate predictions with a changing mean climate, where parameterizations, which have been developed for present day climate, might collapse. The systematic error introduced by using the PPH approximation is usually balanced by introducing other compensating effects. This is done by tuning the convection and cloud schemes such that they produce the right amount of cloud water and fractional cloud cover in order to get the radiative fluxes, computed by the model, in agreement with satellite measurements (Barker et al., 2002). It is questionable whether such ad hoc corrections produce the correct results also in a changed climate, which is even more important in the light of the upcoming debate about cloud feedbacks, which might counteract the greenhouse effect (Lindzen et al., 2001).

Several correction approaches as discussed in Chapter 3 have been implemented into the ECHAM5 climate model in order to estimate their influence on the shortwave radiation fluxes. They are described in the following chapter after a short introduction of the ECHAM5 model. The experiments can be divided into two groups: First, the effective thickness approach can be used with different choices of reduction factors. Second, the results of the Beta Weighted Two-Stream Approximation are presented followed by some sensitivity studies.

5.1 Brief Model Description

The Atmospheric General Circulation Model (AGCM) ECHAM (Roeckner et al., 1992) has been developed at the Max-Planck-Institut für Meteorologie in Hamburg. It evolved from the model of the European Centre for Medium Range Weather Forecasting, Reading, and is currently released in its fifth version. Compared to the ECMWF model there are considerable differences in its parameterization for soil processes, local runoff, simple prognostic sea ice temperature, boundary layer physics, prognostic cloud liquid water and ice and cloud cover. The dynamical framework and basic equations are documented in DKRZ (1993) for the ECHAM3 version, additional information and performance of the ECHAM4 release have been reported by Roeckner et al. (1996), and similar reports for the ECHAM5 model, which is used in this work, are in preparation (Roeckner et al., 2003).

The prognostic dynamical variables, vorticity, divergence, temperature and logarithm of surface pressure, are represented as expansions in spherical harmonics with triangular truncation. In the vertical, hybrid σ-p levels are used extending from the surface to $10\,\mathrm{hPa}$. The finest resolution is used for the planetary boundary layer. The lowest model level is placed at $30\,\mathrm{m}$ above the surface, which roughly corresponds to the height of the surface layer. The remainder of the boundary layer is resolved by four additional levels reaching up to about $1.5\,\mathrm{km}$ height. The time integration uses a leap-frog scheme with a weak time filter. The time-step depends on the truncation of the spectral expansion. Since radiative transfer calculation is computationally expensive, this is performed once every $2\,\mathrm{h}$ and the solar heating rates are extrapolated in between these times. This implies that changes in the atmospheric conditions are only accounted for on this coarser temporal resolution.

Advection of the positive definite variables such as water vapor, cloud liquid water and ice, distribution moments of the cloud cover scheme (see Section 3.2.2) and optional tracers are treated by a flux-form semi-Lagrangian scheme (Lin and Rood, 1996).

Most land surface data are input as climatologies comprising of parameters such as orography, background albedo, roughness length, vegetation type and leaf area index (Hagemann, 2002). Soil water holding capacity, heat capacity and thermal conductivity are also prescribed.

Horizontal diffusion is scale-selective due to the use of a higher order scheme with a sponge zone in the lower stratosphere. Vertical turbulent exchange is parameterized by a 1.5 order turbulence closure with coefficients dependent on turbulent kinetic energy (Brinkop and Roeckner, 1995) for which turbulent transport, dissipation, wind shear and buoyancy flux are considered, but advection is neglected. Cloud-turbulence interactions comprise of vertical exchange of turbulent kinetic energy generated through radiative cooling at cloud top, turbulent flux of cloud water at cloud top, and the impact of cloud water on buoyancy flux. Monin-Obukhov similarity theory yields the turbulent surface fluxes. Gravity wave drag is parameterized after Lott and Miller (1997).

The Tiedtke (1989) mass flux scheme is the basis for the cumulus convection, but

subject to modifications following Nordeng (1994). Buoyancy determines organized entrainment, whereas organized detrainment occurs at the tops of clouds, which are treated as an ensemble. Convective available potential energy (CAPE) is used for the closure assumptions in deep cumulus. Stratiform clouds depend on microphysical processes involved in precipitation formation as well as phase changes and settling of ice crystals (Lohmann and Roeckner, 1996). Cloud cover is computed by a prognostic statistical scheme (Tompkins, 2002).

Radiation is treated as in the ECMWF numerical weather prediction model with minor changes, which will be discussed later. Two-stream approximations are used in the infrared (Mlawer et al., 1997) and solar part (Fouquart and Bonnel, 1980) of the spectrum. The latter is described in more detail in Section 2.2. The physical package is capable of a treatment of ozone as well as methane, nitrous oxide and several CFCs. The parameterization of the cloud optical properties is also presented in Section 2.2.

5.2   Experiment Setup

Except for the sensitivity studies in Section 5.5.2 all experiments are performed with the ECHAM5 model in T42 ($\approx 2.8°$) resolution with 19 vertical layers and an integration timestep of $1440\,\mathrm{s}$. The standard radiation scheme for which the model is tuned, is an Effective Thickness Approximation with a varying reduction factor. It is described in more detail in Section 5.4.3. The fluxes calculated by this scheme are passed to the dynamical part of the model, while alternative schemes are computed non-interactively along with it and their corresponding fluxes are stored as additional output. The radiation computations of the original, driving scheme and the new parameterizations are performed for the same timestep, so all atmospheric input parameters are identical. Therefore there are no feedbacks between these radiation schemes and the model dynamics, like e.g. changes in cloudiness, but they only produce diagnostic output. Differences in the albedo values are only due to the changed treatment of cloud inhomogeneities in the shortwave radiation code. If one wants to perform experiments allowing for full feedback of radiation onto the model one would have to tune the model for every radiation parameterization individually and separate the influence of the altered tuning from that of the revised radiation computation.

The model is integrated for two years in order to reach a balanced state. These data are not used for the analysis. Another five years are then simulated for generating the climatologies presented in the subsequent sections.

5.3   Cloud and Radiation Climatologies

Cloud-radiation interactions are influenced by various model variables. The most important ones are of course those describing the clouds itself, i.e. liquid and ice water path and
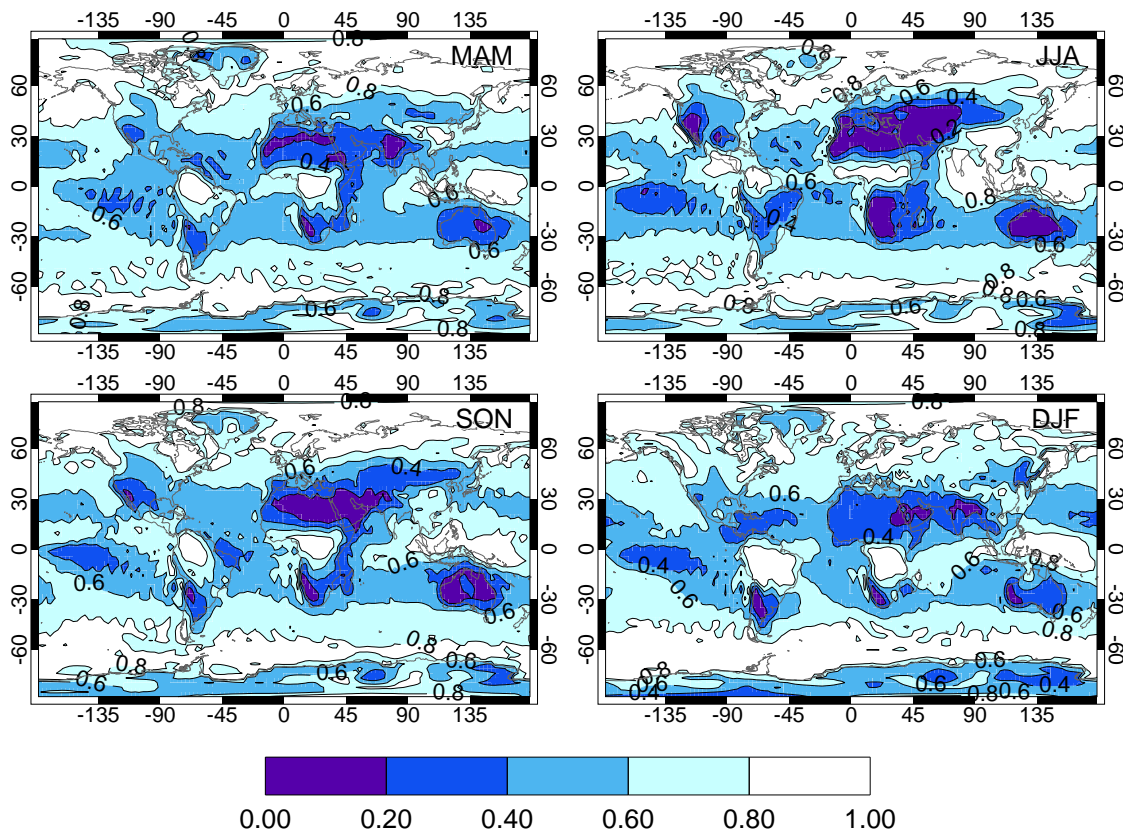
Figure 5.1: Seasonal averages of simulated total cloud cover.

cloud fraction. In the following section the climatology of these properties is presented as seasonal averages over the five years of model simulation described above; the corresponding values for the sensitivity experiments are given in Section 5.5.2. Furthermore, the solar radiation fluxes will be characterized by the albedo and net flux at the top of atmosphere, while the influence of clouds on radiation is shown by means of cloud radiative forcing concept (defined later).

Figure 5.1 shows the seasonal averages of total cloud cover. One can clearly identify some striking structures (Barrett, 1974): A belt of enhanced cloudiness aligned generally along $0°$–$10°$ N, which is related to the equatorial trough. Clearer skies stretch across the tropical oceans strongly oriented from east to west. They can be associated with the Hadley cell subsidence regions, as are the very clear skies over the tropical and subtropical continental land masses. Those areas of nearly zero clouds lucidly identify the desert regions. The tongues of heavy cloud cover extending equatorward through low latitudes off the west coasts of the continents are mostly comprised of cloud sheets beneath the low-level inversions of the stratocumulus regime. Cloud cover in these regions is systematically underestimated by current climate models, including ECHAM5, although simulations have been improved by use of the statistical cloud scheme of Tompkins (2002). In the mid-latitudes, similarly strong cloudiness is associated mainly with belts of extra-tropical
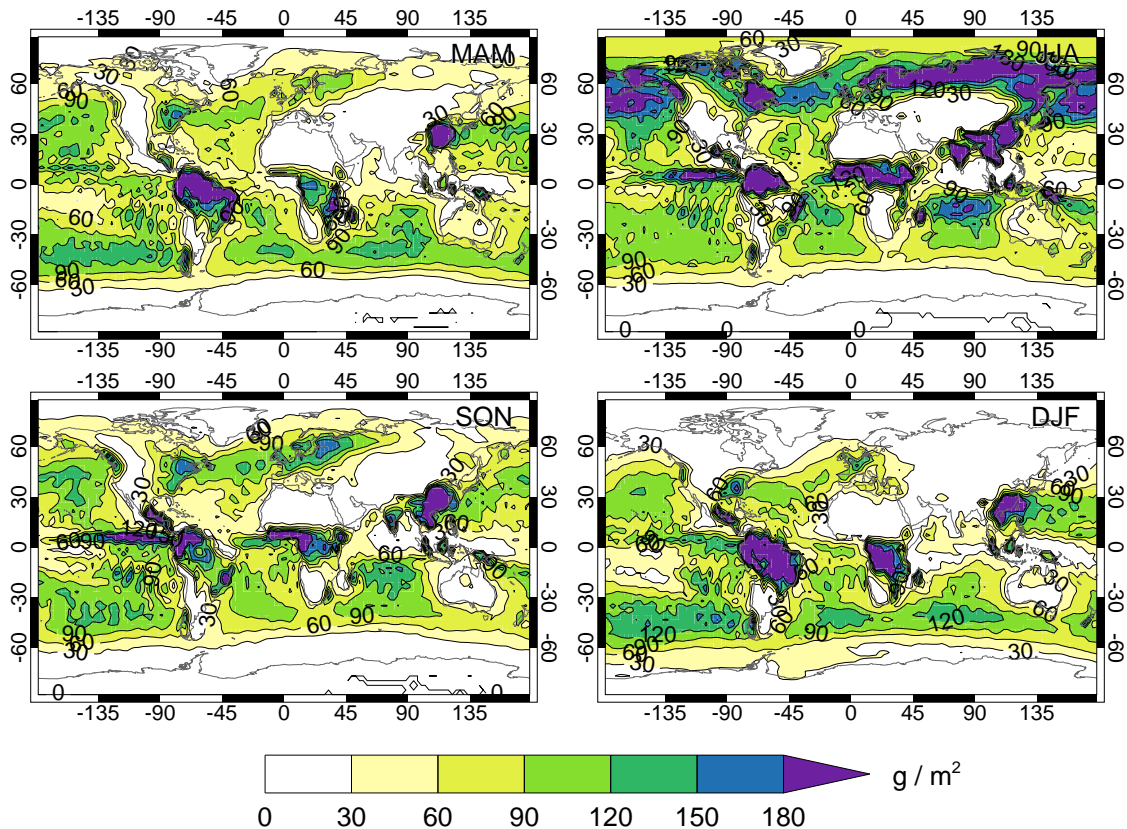
Figure 5.2: Seasonal averages of simulated liquid water path (LWP).

depressions, while the relatively clearer skies across parts of the northern continental interiors, particularly in the local summer seasons, are due to the drier conditions than those prevailing across the oceans.

Column integrated cloud liquid water or liquid water path (LWP) is illustrated in Figure 5.2. Strong tropical convection, especially over the continental land masses in the Inter Tropical Convergence Zone (ITCZ), are responsible for the maxima close to the equator, while in the extra-tropics the increased cloud liquid water marks regions of strong cyclonic activity. Belts of reduced liquid water path can be seen in the subtropics, which are associated with drying in the sinking branch of the Hadley circulation (Lohmann, 1996).

In the tropics the ice water path (IWP) exhibits similar behavior (see Figure 5.3). The freezing level there is located at high altitudes so ice clouds only can form, when humidity is transported high enough by strong convective events, which were already identified by the maxima of the liquid water path. Over the Pacific warm pool a pronounced maximum prevails throughout the whole year. Extra-tropical maxima however are prominent in the winter hemisphere, while in local summer secondary maxima appear. In contrast to the liquid clouds, not only the supply with humidity is important, which is especially governed by surface temperature, but also the altitude of the freezing level plays a dominant
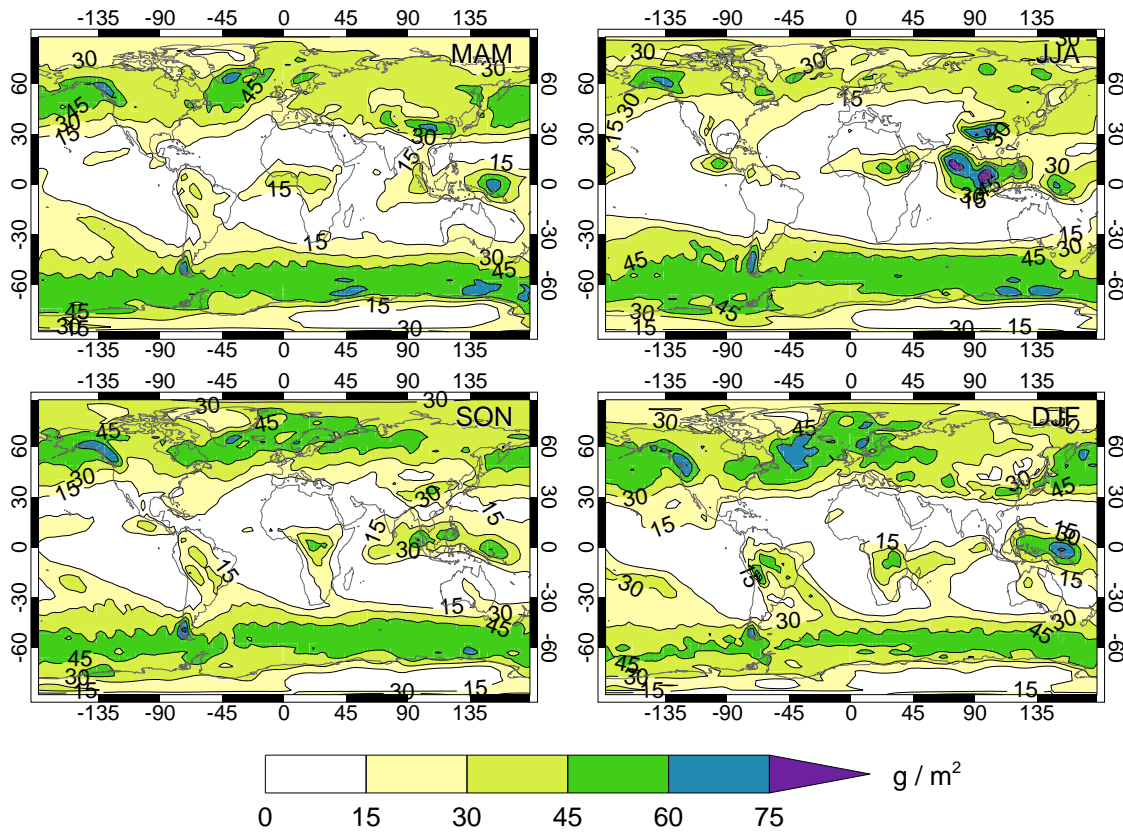
Figure 5.3: Seasonal averages of simulated ice water path (IWP).

role. The seasonal and annual global means of cloud cover, liquid and ice water path are compiled in Table 5.1.

The planetary albedo is strongly influenced by the distributions of cloud water and ice and the surface albedo, especially in the clear sky regions. The seasonal averages are shown in Figure 5.4. In large parts they are similar to the patterns of the cloud cover (see Figure 5.1), since clouds are the most important modulator. For northern Africa the albedo values are high despite a low cloud cover throughout the year, caused by the high surface reflectivity of the Saharan sand; green vegetation lowers the surface albedo substantially. Similarly the ice covered polar regions reveal high reflectivity due to surface

	DJF	MAM	JJA	SON	ANN
cloud fraction	0.63	0.63	0.63	0.62	0.62
LWP / $\mathrm{g\,m^{-2}}$	65	66	83	68	70
IWP / $\mathrm{g\,m^{-2}}$	24	24	23	24	24

Table 5.1: Cloud climatology in ECHAM5: Seasonal and annual global mean values of cloud cover, liquid (LWP) and ice (IWP) water path.
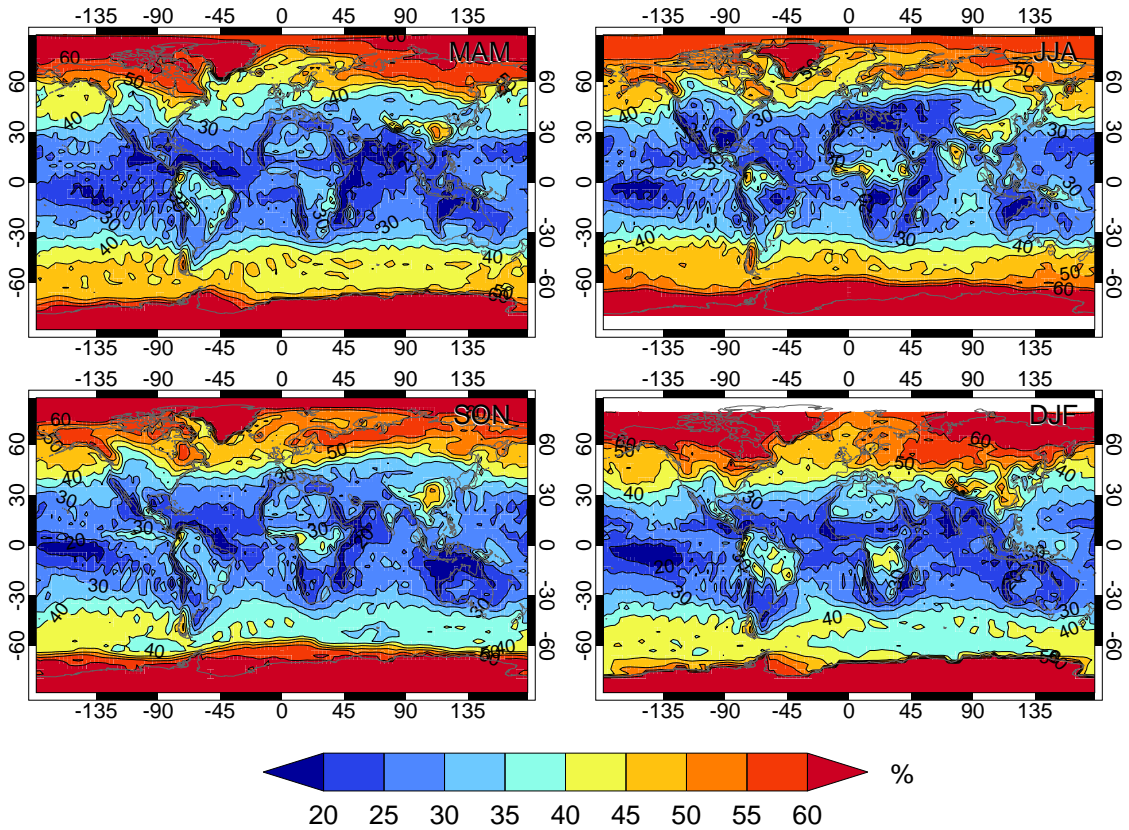
Figure 5.4: Seasonal averages of simulated planetary albedo.

reflectance independently of the cloudiness. In addition to cloud cover cloud thickness, i.e. the amount of condensate they carry, also influences the albedo. Over the northern part of South America for example it is modulated by the varying liquid water content, when cloud cover is nearly constant over the year. The seasonal and annual mean values are listed in Table 5.2.

The energy fluxes absorbed in the atmosphere or at the surface are important for the dynamics of the climate system. One can derive these fluxes from the albedo values by simply multiplying with the incoming fluxes at the TOA. Figure 5.5 illustrates the annual mean net shortwave radiation at the TOA. The net shortwave radiation is the difference between incoming and outgoing radiation, getting absorbed in the system,

$$F^{\text{net}} = F^{\downarrow} - F^{\uparrow}. \tag{5.1}$$

In the long term annual and global mean it is balanced by the thermal radiation emitted by the earth. The effect of clouds on the energy budget can be more clearly depicted by the concept of *cloud radiative forcing (CRF)* (Ramanathan, 1987)

$$\text{CRF} = |F_{\text{clr}}^{\uparrow}| - |F_{\text{tot}}^{\uparrow}|, \tag{5.2}$$

where $F_{\text{tot}}^{\uparrow}$ is the upward directed flux and $F_{\text{clr}}^{\uparrow}$ is the upward flux for a hypothetical

	DJF	MAM	JJA	SON	ANN
albedo / %	33	32	33	32	32
$F_{\mathrm{TOA}}^{\mathrm{net}}/\mathrm{W\,m^{-2}}$	236	231	223	233	231
$F_{\mathrm{TOA}}^{\uparrow}/\mathrm{W\,m^{-2}}$	115	108	108	110	110
CRF / $\mathrm{W\,m^{-2}}$	58	53	58	55	56

Table 5.2: Radiation Climatology in ECHAM5: Seasonal and annual global mean values of albedo, net flux (TOA), upward flux (TOA) and cloud radiative forcing.

atmosphere, which is identical with the true one, except that clouds are removed. The CRF is the radiative energy which is absorbed by the earth-atmosphere system due to the presence of clouds. Generally, clouds increase the reflectivity and thus the upward directed radiation at the TOA. The SW CRF therefore is negative and cools the earth. In contrast, the clouds reduce the emitted radiation in the thermal spectral region, so the LW CRF is positive, thus warming the earth. The annual mean distribution of the SW CRF is displayed in Figure 5.6, its seasonal and annual mean values are also listed in Table 5.2.

5.4 Effective Thickness Approach

The ECHAM5 standard radiation scheme uses a variant of the ETA, developed by Roeckner et al. (2003). In the following section various other ETA realizations are tested. The reference is always the diagnostics, where radiation has been computed using the PPH approximation with no further corrections. As described in Section 5.1 this has been implemented as an additional diagnostic along with the other ETA schemes, so the same cloud properties are used for all radiation algorithms. A brief overview is given in Table 5.3.

5.4.1 Fixed Reduction Factor

The simplest implementation of the ETA follows Cahalan et al. (1994): All cloud properties (single scattering albedo, asymmetry factor and optical depth) are calculated from the grid mean cloud properties. For the radiation a smaller value of the optical thickness $\tau_{\mathit{eff}} = 0.7\tau$ is used everywhere. The results obtained by this scheme are labeled "CS" (Cahalan-Scaling). Seasonal mean values of the albedo differences between NO and CS are plotted in Figure 5.7. Since CS simply reduces the optical thickness and therefore the reflectivity of clouds, the differences are positive, the earth becomes darker. For the seasonal and annual global means refer to Table 5.4.

The albedo corrections follow in parts the patterns of cloud fraction in Figure 5.1, because only the radiative transfer through clouds has been altered, while the clear-sky
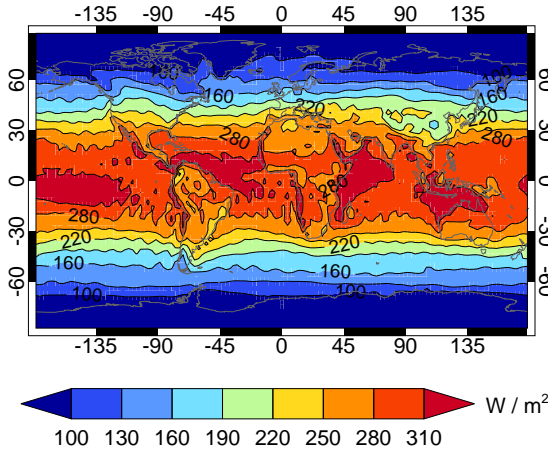
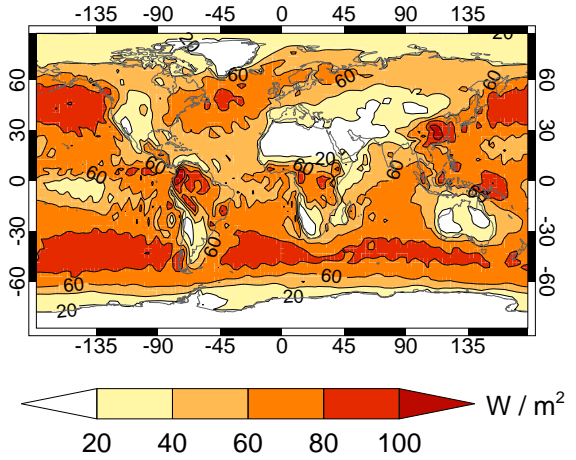**Figure 5.5:** Annual average of simulated net shortwave flux at the TOA.

Figure 5.6: Annual average of simulated SW CRF.

label	reduction factor
NO	$\chi \equiv 1$, i.e. PPH, no correction
CS	$\chi \equiv 0.7$
BS	$\chi_{\text{liq}} = 0.7$ for liquid water clouds $\chi_{\text{ice}} = 1.0$ for ice clouds
TS	$\chi_{\text{conv}} = 0.4$ for convective clouds $\chi_{\text{strat}} = 0.9$ for stratiform clouds
RS	$\chi_{\text{liq}}(W) = 1 - 0.06\,\tilde{W}^{1/3}$ with $\tilde{W} = \min(W, 1000\,\text{g/m}^2)$ for water clouds $\chi_{\text{ice}} = 0.9$ for ice clouds

Table 5.3: Overview of ETA implementations.

	DJF	MAM	JJA	SON	ANN
NO-RS	1.8	1.6	1.9	1.7	1.8
NO-CS	2.2	2.1	2.2	2.1	2.2
NO-BS	1.2	1.0	1.2	1.1	1.1
NO-TS	4.6	4.3	4.4	4.5	4.4
NO-BW	0.9	0.9	0.9	0.9	0.9

Table 5.4: Seasonal and annual global means of albedo differences for various radiation schemes in %.
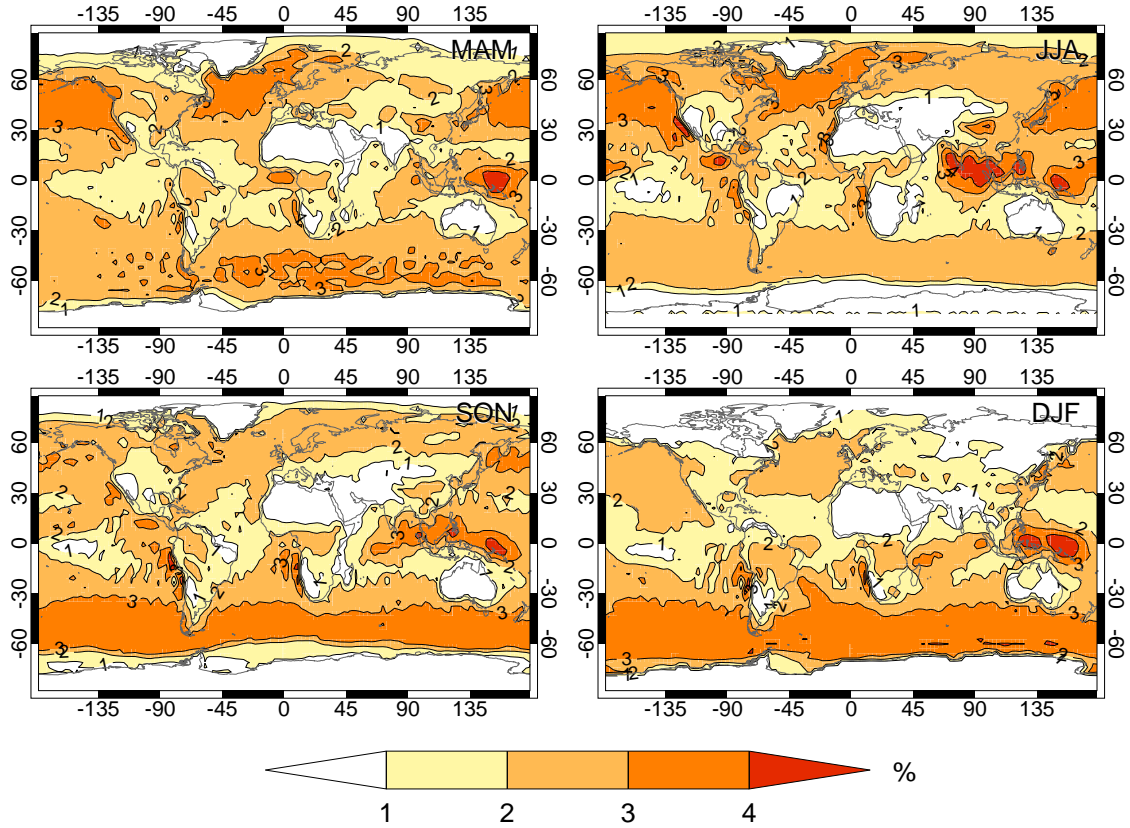
Figure 5.7: Seasonal averages of albedo differences NO − CS.

fluxes are not modified (e.g. over North Africa, Australia and the Antarctic regions).
Secondly, as optical thickness is decreased linearly by CS, the albedo changes most, where
the absolute reduction of optical thickness is largest and the relation between reflectivity
and optical thickness is steep

$$\Delta R \approx \frac{\partial R}{\partial \tau} \Delta \tau. \tag{5.3}$$

Setting $\Delta \tau = (\chi - 1)\tau$ and using the simplified expression (3.7) yields

$$\Delta R = \frac{(\chi - 1)\gamma \tau}{(1 + \gamma \tau)^2}, \tag{5.4}$$

with a maximum for ΔR at $\tau \approx 10$ for $\gamma \approx 0.1$. This means that the absolute albedo
correction is highest for thin stratus or thick cirrus clouds, which have optical thickness
values of around 10. The latter is the reason for the similarities of the patterns of albedo
correction in Figure 5.7 and ice water path in Figure 5.3. Especially the maxima in the
warm pool region and its eastward shift between JJA and DJF can clearly be seen in both
figures. The effects of the higher ice water content in the winter hemisphere is partially
hidden behind an increased cloud fraction in the summer hemisphere.

In order to identify the effect of ice clouds a sensitivity experiment (with two years
integration time) is set up: The ETA is only applied to the liquid part of the clouds,
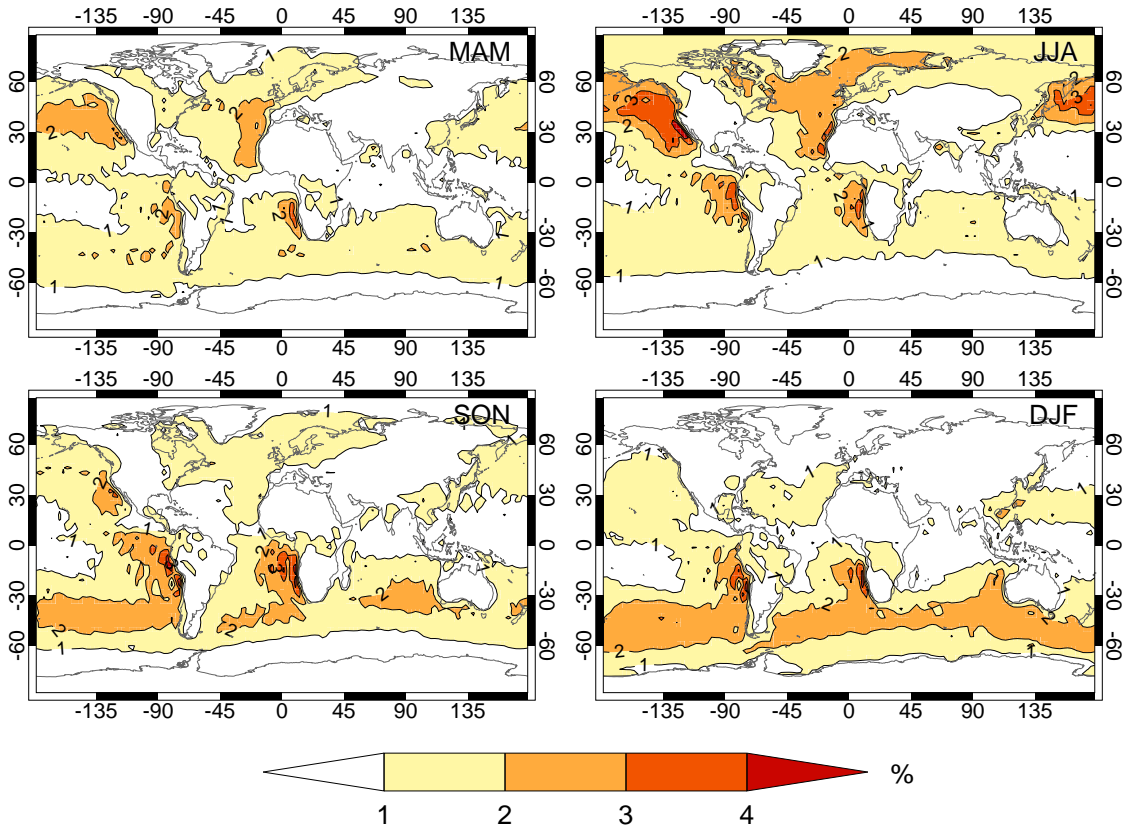
Figure 5.8: Seasonal averages of albedo differences NO − BS.

while the optical thickness of the ice fraction remains unchanged: $\chi_{\mathrm{liq}} = 0.7$, $\chi_{\mathrm{ice}} = 1.0$. Figure 5.8 shows the albedo change compared to NO for this scheme labeled "BS" (Bäuml-scaling). The large changes in the warm pool and in the regions of high ice amount in the winter hemispheres are strongly reduced, while the stratocumulus regimes now are the dominant feature. One thus has to be careful when applying the ETA to cirrus clouds, where sensitivity to the ETA is especially high.

5.4.2 Reduction Factor Depending on Cloud Type

From the experiments with the cloud resolving model data in Chapter 4 we have already seen that using a single reduction factor χ is only a first order approximation. Most climate models do not prognose the variability of clouds, but distinguish between stratiform and convective cloudiness. Convective clouds are more variable than stratiform ones and therefore a smaller reduction factor (i.e. larger correction) has to be applied for them. This refinement has been proposed and implemented into the ECMWF model by Tiedtke (1996). The prognostic cloud scheme of this model distinguishes between convective and stratiform cloudiness (Tiedtke, 1993). For both cloud contributions distinct reduction factors are defined: $\chi_{\mathrm{conv}} = 0.5$ for convective clouds, following Kogan et al. (1995) and
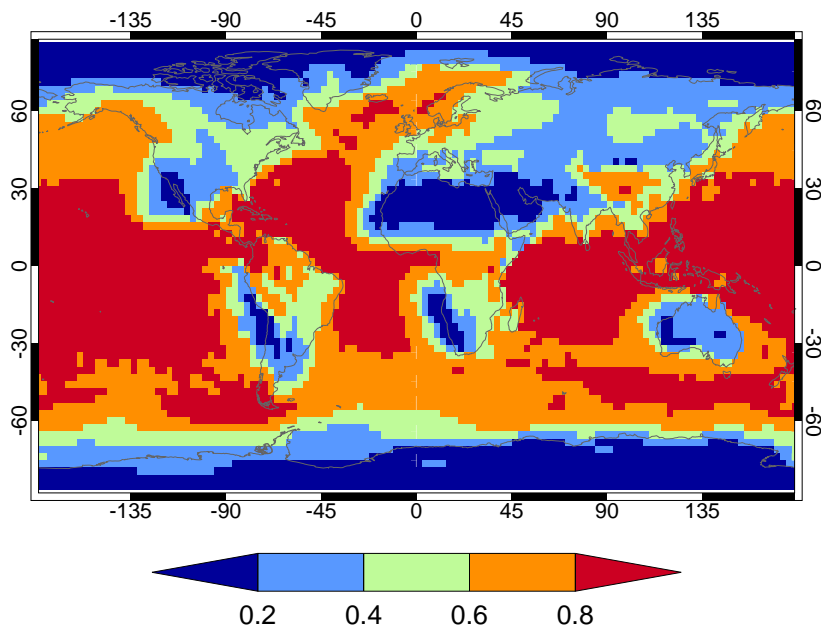
Figure 5.9: Annual mean fraction of convective conditions in ECHAM5.

$\chi_{\mathrm{strat}} = 0.7$ after Cahalan et al. (1994).

The ECHAM5 model uses a different cloud scheme, but nevertheless the convection scheme recognizes four different convection types: no convection (i.e. stratiform clouds or clear-sky), shallow, mid-level and deep convection. We use this information and apply a reduction factor of $\chi_{\mathrm{strat}} = 0.9$, when no convection is diagnosed, and $\chi_{\mathrm{conv}} = 0.4$ else. The values for χ are directly taken from the CRM results of Chapter 4. This approach is labeled "TS" (Tiedtke-scaling). Figure 5.9 shows the annual mean fraction of convective conditions, i.e. the number of time-steps, when shallow, mid-level or deep convection was present, divided by the total number of integration steps; there are only slight seasonal variations. While in the tropical and subtropical oceanic regions convective conditions prevail, they are reduced towards the poles. Remarkable are the relatively low values in the stratus regimes off the west coasts of the continents. Also, over dessert regions convective cloud formation breaks down due to lacking supply of water vapor from the surface.

The albedo correction for stratiform clouds for the TS scheme is smaller than for the CS that we have discussed before, since a reduction factor of 0.9 instead of 0.7 is used. In the stratus regimes off the continental west coasts this can be clearly identified in Figure 5.10, which shows the seasonal mean albedo correction, similar to Figure 5.7. For differences $\Delta\alpha > 7\%$ a new color has been added. All other regions experience higher corrections because of the smaller reduction factor of 0.4. Especially the ice clouds in the warm pool cause large albedo corrections of over 7%. It is important to note that the convection type is only defined for the whole column and thus also is used for the cirrus
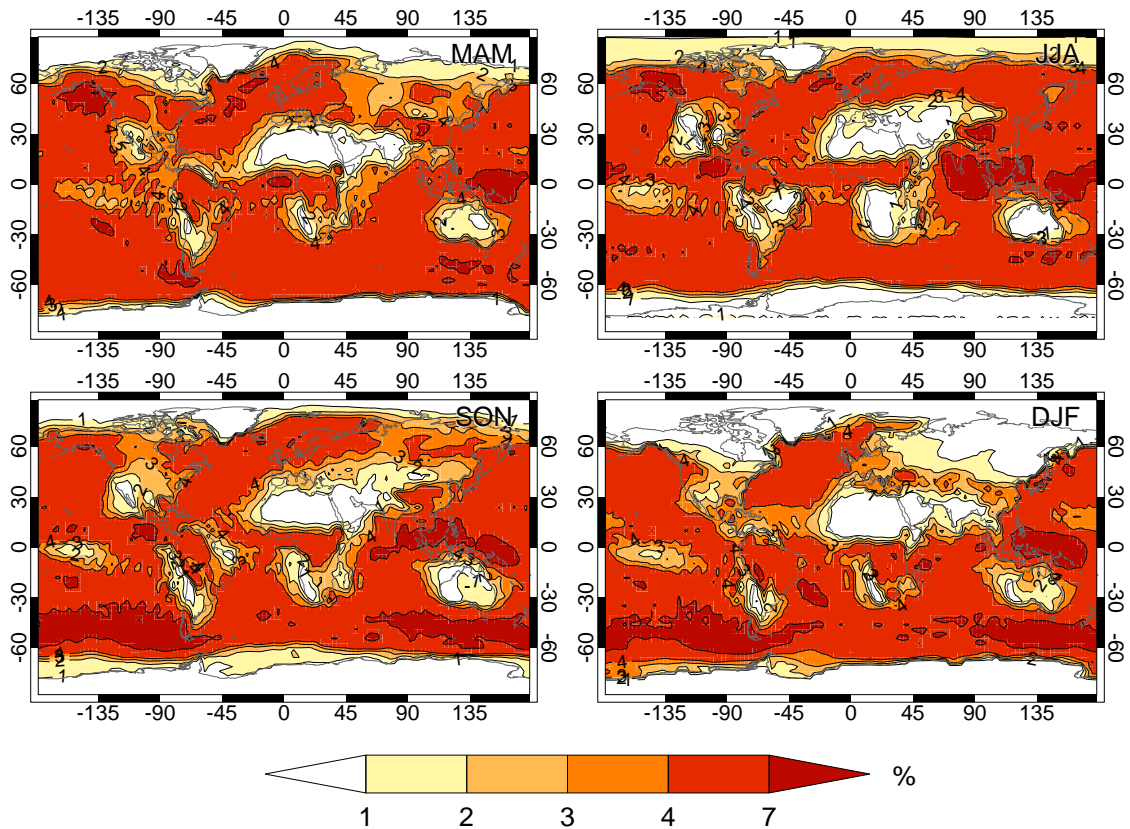
Figure 5.10: Seasonal averages of albedo differences NO − TS.

clouds. The seasonal and annual mean values are again listed in Table 5.4.

5.4.3   Reduction Factor Depending on Liquid and Ice Water Path

The standard radiation parameterization of the ECHAM5 model also uses an ETA variant, here labeled "RS", which combines some of the ideas developed above (Roeckner et al., 2003). In general, deep convective clouds, bearing a large amount of liquid water, are more turbulent than the thinner shallow convective or stratiform clouds. The reduction factor for thick clouds therefore has to be smaller than for thin clouds, because they are more inhomogeneous. Secondly, we have seen in the derivation of the ETA in Section 3.1

label	NO	CS	TS	BS	RS	BW
$F^{\mathrm{abs}}/\mathrm{Wm}^{-2}$	77.7	77.0	76.4	76.9	76.9	77.2
SW CRF $/\mathrm{Wm}^{-2}$	62	55	47	58	56	59

Table 5.5: Annual mean of globally averaged atmospheric absorption and cloud radiative forcing for various ETA variants and the BWTSA scheme.
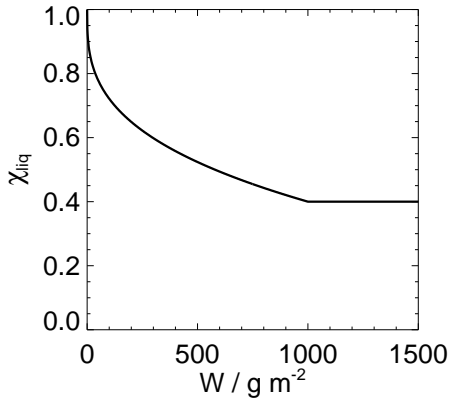
Figure 5.11: Reduction factor for liquid water clouds, χ_{liq}, as a function of liquid water path, W, as implemented in the RS scheme according to (5.5), (5.6).

that the approximation is good only for optical thicknesses between approximately 1.5 and 15; for smaller optical thickness a larger reduction factor has to be chosen, while for larger thickness a smaller χ is adequate. Both effects are accounted for by expressing the reduction factor χ_{liq} for liquid water clouds as a function of liquid water path W and thus optical thickness as

$$\chi_{\text{liq}} = \begin{cases} 1 - c_0 W^{c_1} & \text{for } W < W_{\text{max}} \\ 1 - c_0 W_{\text{max}}^{c_1} & \text{else.} \end{cases} \tag{5.5}$$

The constants c_0, c_1 and W_{max} are tuning parameters which are set to

$$c_0 = 0.06$$
$$c_1 = \frac{1}{3} \tag{5.6}$$
$$W_{\text{max}} = 1000 \, \text{g/m}^2$$

so that χ_{liq} varies between 1 for thin clouds and 0.4 for thick clouds in accordance with the CRM results. The same reduction factor is also used for the longwave radiation transfer computation, following Rossow et al. (2002). The shape of the function is empirically chosen in order to optimize the longwave and shortwave fluxes compared to satellite data simultaneously (Roeckner et al., 2003). For the given parameter settings the function is plotted in Figure 5.11.

Ice clouds are treated separately. Buschmann (2001) investigated the radiation fluxes through cirrus cloud fields, derived from aircraft measurements, by Monte Carlo techniques. She found a PPH-bias between the three-dimensional computation and the PPH analogue, which could be removed by using an effective optical thickness for the PPH computation. From these effective optical thicknesses and their corresponding true mean values for the various cloud sets one can easily derive a reduction factor $\chi = \tau_{eff}/\overline{\tau}$. The latter varies between the extreme values of 0.6 and 1.0, and is typically around 0.9. This value is implemented in the ECHAM5 albedo correction as a constant reduction factor for ice clouds,

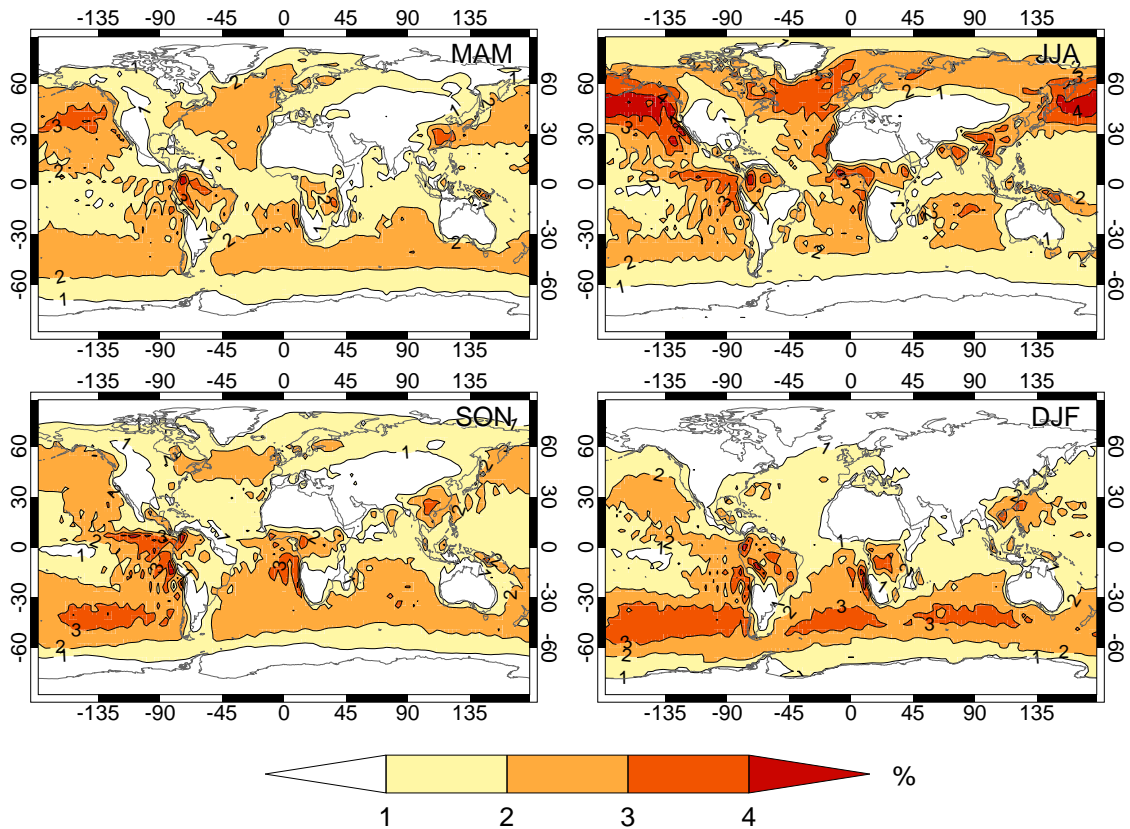$$\chi_{\text{ice}} = 0.9. \tag{5.7}$$

Figure 5.12: Seasonal averages of albedo differences NO − RS.

The albedo changes NO−RS in Figure 5.12 have a similar structure as in the BS case, in as much as the regions with high ice cloud amount are not emphasized. For the liquid clouds however the corrections are of course higher due to the reduction factor reaching values as low as 0.4 compared to the 0.7 in the BS implementation. Especially the thick clouds in the convective regions, which can be identified in Figure 5.9 and more directly from high LWP values in Figure 5.2, are emphasized in comparison to BS, but are closer to the patterns in TS. Nevertheless, the corrections there are higher, since the extreme value $\chi = 0.4$ is used throughout the convective regions, while now it is only applied as an extreme for the thickest clouds.

As for the CRM experiments the influence of the ETA on absorption will be briefly discussed. For all of the ETA variants introduced above the changes in atmospheric absorption are listed in Table 5.5. The effective reduction of cloud optical thickness results in a slightly lower absorption by less than $1\,\mathrm{Wm^{-2}}$. We can compare this to the uncertainty of the radiation simulation, discussed in the debate about excess absorption. Measurements suggest absorption being up to $10\,\mathrm{Wm^{-2}}$ higher than simulated. The ETA enlarges this difference, but is clearly of minor importance.
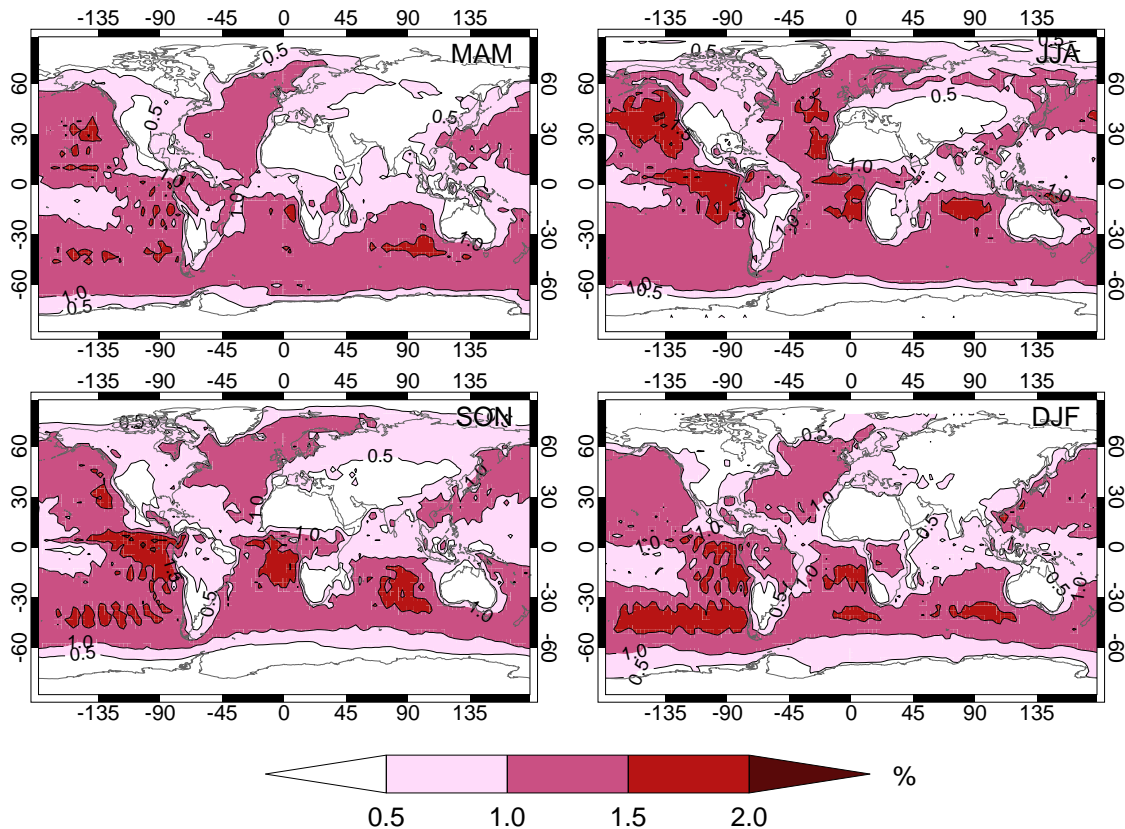
Figure 5.13: Seasonal averages of albedo differences NO − BW.

5.5 Beta Weighted Two Stream Approximation

In contrast to the ETA approach the statistical BWTSA scheme does not need to parameterize the variability of clouds in terms of convection type, condensate phase or liquid water path, because it obtains this information directly from the cloud scheme. The model thus becomes more consistent and less subjected to tuning. Nevertheless, the cloud scheme itself contains a couple of tuning parameters. In the following section, first the results of the BWTSA scheme in the standard resolution T42 will be introduced. Then various sensitivity experiments are discussed, evaluating the influence of increasing the resolution and modifying the tuning parameters of the cloud scheme.

5.5.1 Standard Configuration

Parallel to the ETA variants radiative fluxes are also computed by the BWTSA code and written as an additional diagnostic output, while the fluxes driving the dynamics of the simulation are still calculated by the ECHAM5 standard scheme (RS). The changes in albedo for this "BW"-parameterization against the NO case are depicted Figure 5.13. It should be emphasized that the contour levels are halved compared to the analogous

plots in the ETA section. The global mean values of albedo and flux changes are smaller than in all ETA variants (see Table 5.4) and are only roughly half of the RS changes. Nevertheless the general structure is similar to the RS scheme: The amplitude follows in large parts the cloud cover in Figure 5.1. Especially the seasonal variations of the stratus decks off the continental west coasts can clearly be identified by larger corrections, as is the increased cloudiness in the cyclone paths in local summer. In contrast to the CS study the regions with high ice water path are not emphasized. This is a remarkable similarity to the BS and RS simulation, where the optical thickness of ice clouds is corrected not at all or only little with $\chi_{ice} = 0.9$, respectively. In the BW experiment cirrus clouds are *not* treated specially, but also only exploit the variability as prognosed by the cloud scheme. Apparently, this seems to be consistent with the ETA parameterization RS, which was based on various CRM and measurement results. But there is of course a major advantage of the statistical scheme compared to the ETA: The cloud inhomogeneity is not coupled to some grid mean cloud property like liquid water path. Local deviations from such average relationships, used for the ETA parameterization, are therefore resolved in the BWTSA. Variations in the aerosol loading could, for example, influence the cloud microphysics and finally the variability of clouds (Barker, 2000). Orography or dynamical features like gravity waves could also be thought of. Obviously, they only affect the radiative transfer if they are accounted for in the statistical cloud scheme prognosing the PDF. Secondly, statistical schemes like the BWTSA do not suffer from a limited range of applicability as it is the case in the ETA, which is strictly valid only in the linear regime of $R(\log \tau)$ (see Figure 3.1). No empirical thresholds or switches like the ice/liquid cloud distinction or the functional dependency of χ on W therefore have to be introduced.

Both the BWTSA and the ETA schemes cannot be directly evaluated with satellite measurements, since any error in the underlying cloud parameterizations immediately changes the radiative fluxes. Therefore it is difficult to decide which correction has the proper amplitude. From the analysis of high resolution satellite images the necessary correction for the stratus regions have been carefully estimated and correspond to an reduction factor of roughly 0.7 in the ETA (Oreopoulos and Davies, 1998a,b); the BWTSA corrections are smaller. On the other hand, the satellite pictures only represent a small area. The CRM experiments in Chapter 4 showed that reduction factors as high as 0.9 may also be found in stratus decks. Therefore the RS values are not suitable as a reference to test other schemes. Nevertheless, the smaller albedo corrections of BW are consistent with the results from Section 4.2.3, where the effects of the correlation assumption for multilayer clouds was qualitatively studied. Assuming perfect correlation in the vertically highly resolved CRM data lead to approximately doubled albedo correction. Correlation can be expected to be less important for the comparably thick levels of the GCM and when relaxing the perfect correlation assumption. On the other hand, since the current BWTSA implementation does not account for any correlation effects, the albedo corrections are underestimated, but are unlikely to reach the RS values. This means that either the RS

label	A_c	LWP $\mathrm{g\,m^{-2}}$	IWP $\mathrm{g\,m^{-2}}$	$\Delta\alpha$ %	$\Delta F_{\mathrm{TOA}}^{\mathrm{net}}$ $\mathrm{Wm^{-2}}$	description
BW	0.62	70	24	0.92	3.1	standard BWTSA
HR	0.62	71	29	0.80	2.7	high resolution
DS	0.60	62	24	0.87	3.0	doubling skewness
CK	0.62	69	24	0.90	3.1	changing convection parameter K
FT	0.58	77	24	1.00	3.4	fixed relaxation time

Table 5.6: BWTSA sensitivity studies. All values are global annual means. Differences are compared to NO.

overestimates the PPH-bias or the probability distributions prognosed by the cloud scheme are too homogeneous and BW underestimates the bias. Currently, there are no satellite measurements available to test these hypotheses. Rossow et al. (2002) started to produce climatologies of cloud variability from ISCCP data sets, which they express as a correction factor ϵ, which can be rewritten as $\epsilon = 1 - \chi$. In contrast to the reduction factors in the ETA, this ϵ describes the albedo correction for the *whole* atmospheric column, including clear sky regions and vertical inhomogeneities. The former is resolved explicitly by the model, while the latter is parameterized in parts by the maximum-random cloud overlap assumption, so the correction found by Rossow et al. (2002) are higher than those of the ECHAM5 scheme. In fact, they find albedo biases up to 10% (seasonal mean) in contrast to the 5% and 3% for RS and BW, respectively.

5.5.2 Sensitivity Studies

In contrast to the ETA approaches discussed earlier, the BWTSA correction directly depends on prognostic variables of the ECHAM5 cloud scheme, describing the probability distribution of the total water mixing ratio. Since the cloud scheme was developed and tuned in order to diagnose the *cloud fraction* correctly, it is necessary to test how sensitive the derived radiation correction reacts on changes of model resolution and the cloud scheme tuning parameters. A high resolution experiment (T106) is made in the same way as the previous simulation, i.e. the model dynamics is forced by the standard radiation scheme, while the corresponding BW and NO fluxes are computed only diagnostically. When testing the sensitivity due to changes in the cloud scheme tuning parameters, on the other hand, also the cloud cover and thus the model dynamics is affected. These results are therefore not quantitatively comparable to the previous studies. For an overview of the sensitivity studies refer to Table 5.6.
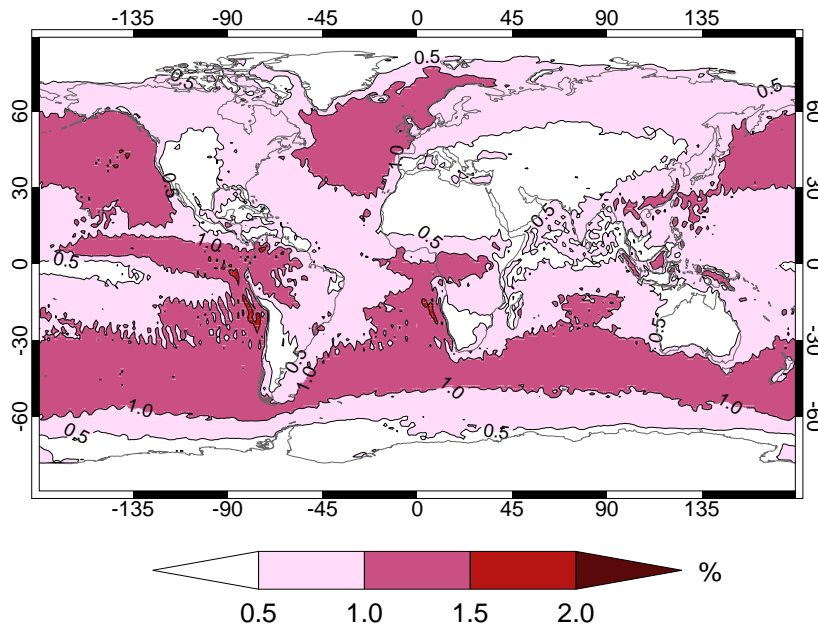
Figure 5.14: Annual average of albedo differences NO(T106) − HR.

Increased Horizontal Resolution

Sub-grid scale properties like cloud fraction and mixing ratio PDF are less important for smaller grid spacing of the climate model. The albedo correction for the ECHAM5 simulation with a spectral resolution of T106 ($\approx 1.1°$, integration time-step 720 s), i.e., grid-spacing is only one third of the previous T42 experiments, are consistently smaller: The global annual flux difference compared to the uncorrected scheme $\Delta F_{\text{TOA}}^{\text{net}}$ is $2.7\,\text{Wm}^{-2}$, while it is $3.1\,\text{Wm}^{-2}$ for T42 (see Table 5.6). Cloud fraction, liquid and ice water content are comparable. The patterns of the albedo change in Figure 5.14 are similar to that of the lower resolution simulation. Here only the annual mean is shown; the seasonal cycle is similar to the T42 results in Figure 5.13.

Doubling skewness parameter

Two parameters determine the shape of the Beta-distribution. While one is held constant the second, skewness, is prognosed by the cloud scheme. In the DS experiment the value of the shape parameter $\tilde{v}$ is doubled by simply changing the initial value $\tilde{v}_0 = 2$ to $\tilde{v}_0 = 4$ and multiplying all tendency equations for $\tilde{v}$ by a factor of 2. The distributions thus are more skewed, the tail towards high mixing ratios becomes longer and thus, variability rises. At the same time cloud fraction of course is affected: For two distributions with the same condensate amount but different skewness, the more skewed one produces smaller cloud fraction, because there is a relatively larger fraction within the cloudy part with high mixing ratios (long tail of the distribution), which has to be compensated by a

reduced cloud cover. For DS the globally averaged cloud fraction decreases by 0.02 to $A_c = 0.60$. Simultaneously the liquid water path is reduced due to feedback processes between cloud fraction and cloud microphysics. Therefore, two counteracting processes influence the albedo correction: Larger skewness increases variability, which means the reflectivity becomes smaller in the BWTSA computation. On the other hand, clouds become less important in favor of clear sky parts due to the decreased cloud fraction. On global average the annual mean flux correction for the DS case is $\Delta F_{\mathrm{TOA}}^{\mathrm{net}} = 3.0\,\mathrm{Wm}^{-2}$ compared to $3.1\,\mathrm{Wm}^{-2}$ in the original BW simulation.

Changing K

Convection, expressed by the mass flux, explicitly changes the skewness in the cloud scheme following (3.43). A dimensionless constant K was introduced. In the standard ECHAM5 parameterization it is set to $K = 10$ based on model tuning. In the CK experiment, $K = 20$ is used. This means convective detrainment leads to larger skewness of the total water mixing ratio PDF. The net effect of this change is relatively small (see Table 5.6): Cloud fraction, liquid and ice water paths remain the same and also the flux changes at TOA are identical to BW.

Changing relaxation time

While convection increases the skewness, turbulence homogenizes the distribution, which is formulated as a Newtonian relaxation in (3.42). The relaxation times t_h and t_v are of the order of $10\,\mathrm{d}$ and a few hours, respectively, and are functions of wind shear and turbulent kinetic energy. For the FT experiment $t_v^{-1} + t_h^{-1}$ in (3.42) is set constantly to $1/20\,\mathrm{d}$. The skewed distributions, caused e.g. by convective events, relax two times slower to their symmetric initial state than in the original scheme. The increased skewness is clearly seen in the decreased cloud fraction of $A_c = 0.58$ compared to the original 0.62 for the same reasons as discussed in the DS experiment. Although clouds thus become less important for the planetary albedo the flux correction due to the BWTSA is even higher by $0.3\,\mathrm{Wm}^{-2}$ than for BW, cf. Table 5.6. The increased variability over-weighs the reduced cloud cover. The balance between source and sinks of skewness therefore has to be tuned carefully.

5.6   Comparison to Satellite Measurements

The comparisons between the ETA or statistical correction approaches for the cloud inhomogeneity bias with an uncorrected analogue reveal global shortwave net flux differences at the TOA of $\sim 5\,\mathrm{Wm}^{-2}$. All schemes are consistently implemented into the same GCM, so the differences are solely caused by accounting for the cloud variability. The general

patterns of total albedo and cloud radiative forcing, however, especially depend on cloud cover and mean condensate mixing ratio. While the former is well known from satellite observations, the latter still only may be guessed. Cloud parameterizations therefore have to be tuned against radiation observations in order to yield realistic fluxes at the TOA in the solar and thermal spectra. Due to model deficiencies, like simplified parameterizations or limited horizontal or vertical resolution, or lack of adequate observational data or precision, as we will discuss for the Earth Radiation Budget Experiment (ERBE) data (Barkstrom, 1984), this tuning is not perfect for all properties. In the following section we will compare the radiation climatology from the ERBE project with the ECHAM5 fluxes for different correction parameterizations.

5.6.1   ERBE Data Set

First we will briefly describe the data of the Earth Radiation Budget Experiment (ERBE) following Chen and Roeckner (1996).

The ERBE observation provide monthly data on a 2.5° by 2.5° grid, which are interpolated to the T42 resolution of the ECHAM5 model. We will use planetary albedo, clear sky albedo, outgoing longwave radiation (OLR) and clear sky OLR. A detailed description of the data processing and products is given by Barkstrom (1984). The estimated uncertainty in the monthly averaged fluxes is $\sim 10\,\mathrm{Wm}^{-2}$. There is a bias between shortwave and longwave fluxes: The annual global mean OLR is $6\,\mathrm{Wm}^{-2}$ smaller than the net shortwave radiation, i.e., the energy budget according to ERBE is not balanced, the earth would heat substantially (Hartmann, 1993). The ISCCP data set, where different observations were used, also shows an unbalanced state, but with the OLR being larger than the net shortwave radiation (Rossow and Zhang, 1995). Kiehl and Trenberth (1997) assumed the OLR data to be more confident than the albedo measurements and created an interpolated dataset such that the longwave and shortwave energy fluxes are balanced. The corresponding values are listed in Table 5.7.

There are a few regions, where clear sky fluxes are not available in the ERBE dataset. Because of the permanent occurrence of cloud these areas did not meet the cloud-free criteria in the data processing. It should also be noted that there are difficulties in estimating clear sky fluxes over regions covered with sea ice and snow due to the cloud detection problem. Thus, the clear sky data are less reliable poleward of 60° north and south.

5.6.2   Comparison ERBE versus ECHAM5

Before comparing the actual values and geographical patterns of the model fluxes and the ERBE measurements, the tuning strategy applied for the ECHAM5 model (Roeckner et al., 2003) is briefly discussed. For an atmospheric GCM, especially when coupled to an ocean model, it is important to simulate a balanced annual global mean radiation budget at the TOA. Tuning the model to perfect agreement with the ERBE solar and thermal fluxes

	α	F_{net}	OLR	SW CRF
	%	Wm^{-2}	Wm^{-2}	Wm^{-2}
ERBE	29.8	240	234	-48
ISCCP	32.6	230	234	-54
Kiehl and Trenberth (1997)	31.2	235	235	
RS	32.4	230	229	-56
BW	33.3	227		-59
NO	34.2	224		-62

Table 5.7: Global annual averages of planetary albedo, net SW flux at TOA and SW CRF of ERBE (Hartmann, 1993), ISCCP (Rossow and Zhang, 1995) data and according to Kiehl and Trenberth (1997) and ECHAM5 simulation using RS, BW and NO radiation parameterization.

is not possible, because a net flux of $6\,\text{Wm}^{-2}$ would remain (Hartmann, 1993). In accordance with Kiehl and Trenberth (1997) it was decided to trust more in the longwave observations and tune the model such that the LW CRF is similar to the ERBE data, while deviations in the SW CRF are allowed for in order to achieve a balanced radiation budget. The planetary albedo of the tuned ECHAM5 therefore is higher than that of ERBE — $\alpha_{\text{ECHAM5}} = 32.4$ vs. $\alpha_{\text{ERBE}} = 29.8$ — yielding a balanced radiative budget with a net gain of $< 1\,\text{Wm}^{-2}$.

In the following we will compare the fluxes (global means and geographical patterns) of various ECHAM5 radiation schemes with the ERBE data similarly to Chen and Roeckner (1996), who evaluated the predecessor version ECHAM4 against the ERBE data.

The global annual mean values for the ECHAM5 standard (RS) and the diagnostically computed BWTSA (BW) and uncorrected PPH schemes (NO) are also listed in Table 5.7. The difference between the uncorrected scheme NO and the standard RS is of the same order of magnitude as the difference of RS compared to ERBE, the BWTSA variant is in between theses two. Figure 5.15 shows the meridional distribution of the zonal mean albedo values. In January the model overestimates albedo only slightly in the tropics and more strongly in the subtropics, while it underestimates the albedo in the southern hemisphere mid-latitudes. In the northern hemisphere the correspondence is comparably good. Agreement for July is only found in the northern hemisphere higher latitudes. At all other latitudes the albedo is overestimated, especially in the northern mid-latitudes.

The geographic distributions of the albedo are shown in Figure 5.18. In January the model overestimates the albedo in regions of deep convection in the tropics. The cloud regimes off the west coasts of California and South America are underrepresented. In July, the albedo is too high along the ITCZ and in the southern oceans. These deviations
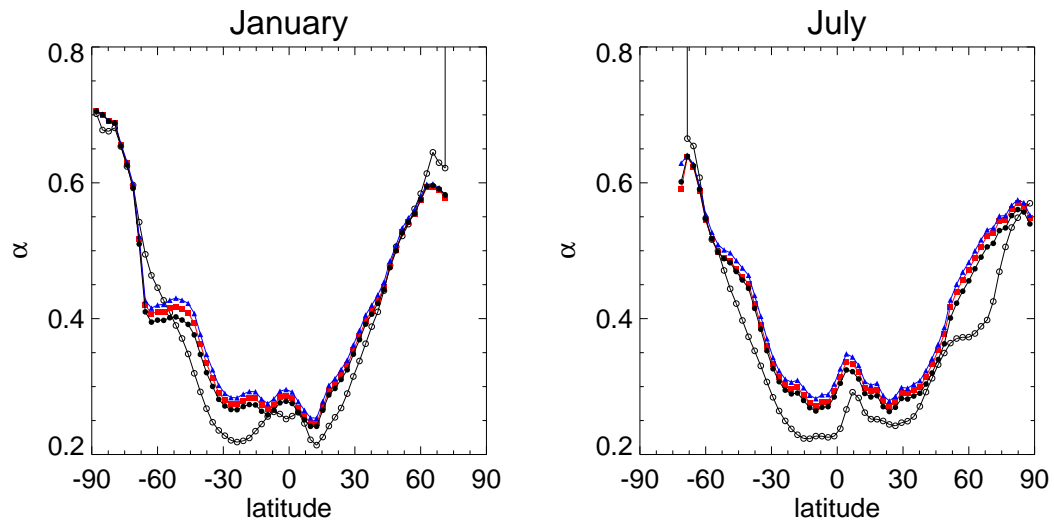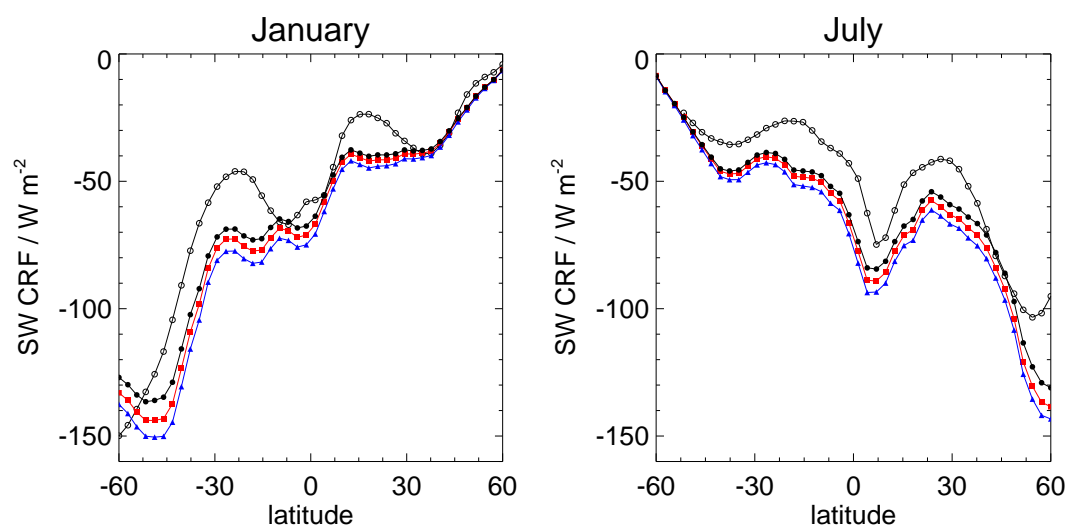
Figure 5.15: Zonally averaged planetary albedo from ERBE (open circles), and various ECHAM5 parameterizations: RS (black circles), BW (red squares) and NO (blue triangles).

are mostly caused by discrepancies between the prognosed and observed cloud cover (see Tompkins, 2002).

As to be expected from the respective distributions of planetary albedo, the zonally averaged SW CRF in Figure 5.16 is overestimated almost everywhere. Note that the SW CRF is only plotted equatorwards of $60°$, because for higher latitudes the ERBE data have large uncertainties. The differences between the various schemes are smaller than their differences to the ERBE values. The geographical distribution of the SW CRF is displayed in Figure 5.19. The pattern of large SW CRF associated with the ITCZ, the South Pacific Convergence Zone (SPCZ) and the convection centers over equatorial Africa and Central-South America as well as the large SW CRF over the summer hemisphere oceanic regions are captured by the model. However, in the tropics it is generally overestimated. Chen and Roeckner (1996) interpret the overestimation in the tropical regions as an effect of neglected cloud variability in the ECHAM4 model, since cloud cover and liquid water path are reasonable, when compared to satellite data or other estimates. They are still present in the new model using the RS correction, so these maxima seem more to be a matter of erroneous cloud characteristics than an inhomogeneity effect. As a second confirmation of their conclusion, Chen and Roeckner (1996) plot the LW CRF vs. SW CRF for the tropical Pacific and Indian Ocean. They find nearly balanced radiative budget in the ERBE data, as depicted in Figure 5.17 (left side), while in the ECHAM4 model the SW CRF is larger than the LW CRF. On the right hand side of Figure 5.17 we see the corresponding plot for the ECHAM5 RS simulation, where cloud inhomogeneities have been accounted for in both, the LW and the SW part. Again the SW CRF is larger than

Figure 5.16: Zonally averaged SW CRF from ERBE (open circles), and various ECHAM5 parameterizations: RS (black circles), BW (red squares) and NO (blue triangles).

the LW CRF, but to a lesser extent than in the ECHAM4 version. This reduction may in part be due to the PPH-bias correction. The remaining differences are probably caused by dissimilarities in the vertical cloud distributions between ERBE and ECHAM5 as, for example, a larger population of low and mid-level clouds in ECHAM5 with relatively small amounts of LW CRF (Hartmann, 1993; Kiehl, 1994), but may not be attributed to cloud variability.
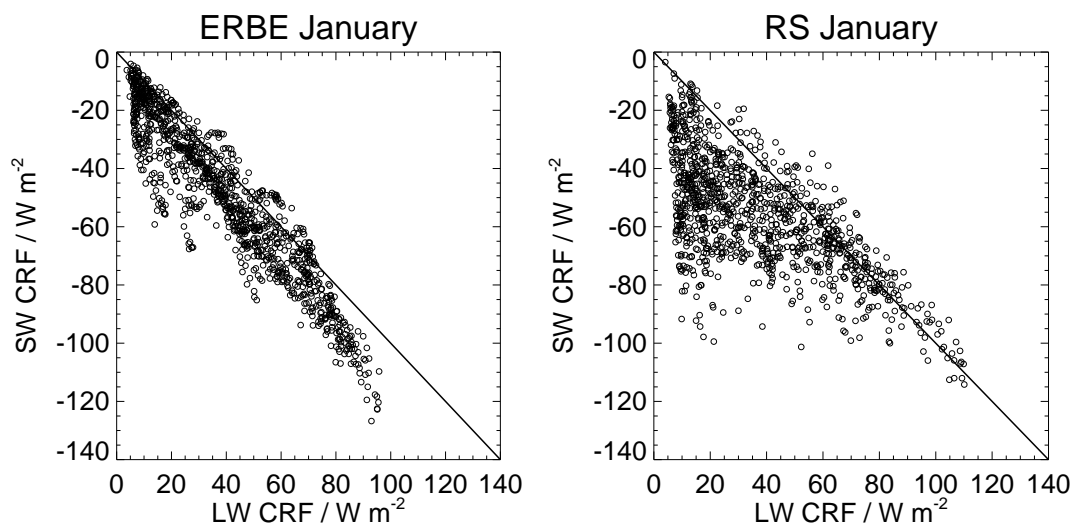
Figure 5.17: January shortwave cloud radiative forcing versus longwave cloud radiative forcing for the tropical Pacific and Indian Ocean region (20°S–20°N, 50°E–90°W) from ERBE (left) and ECHAM5 RS (right).
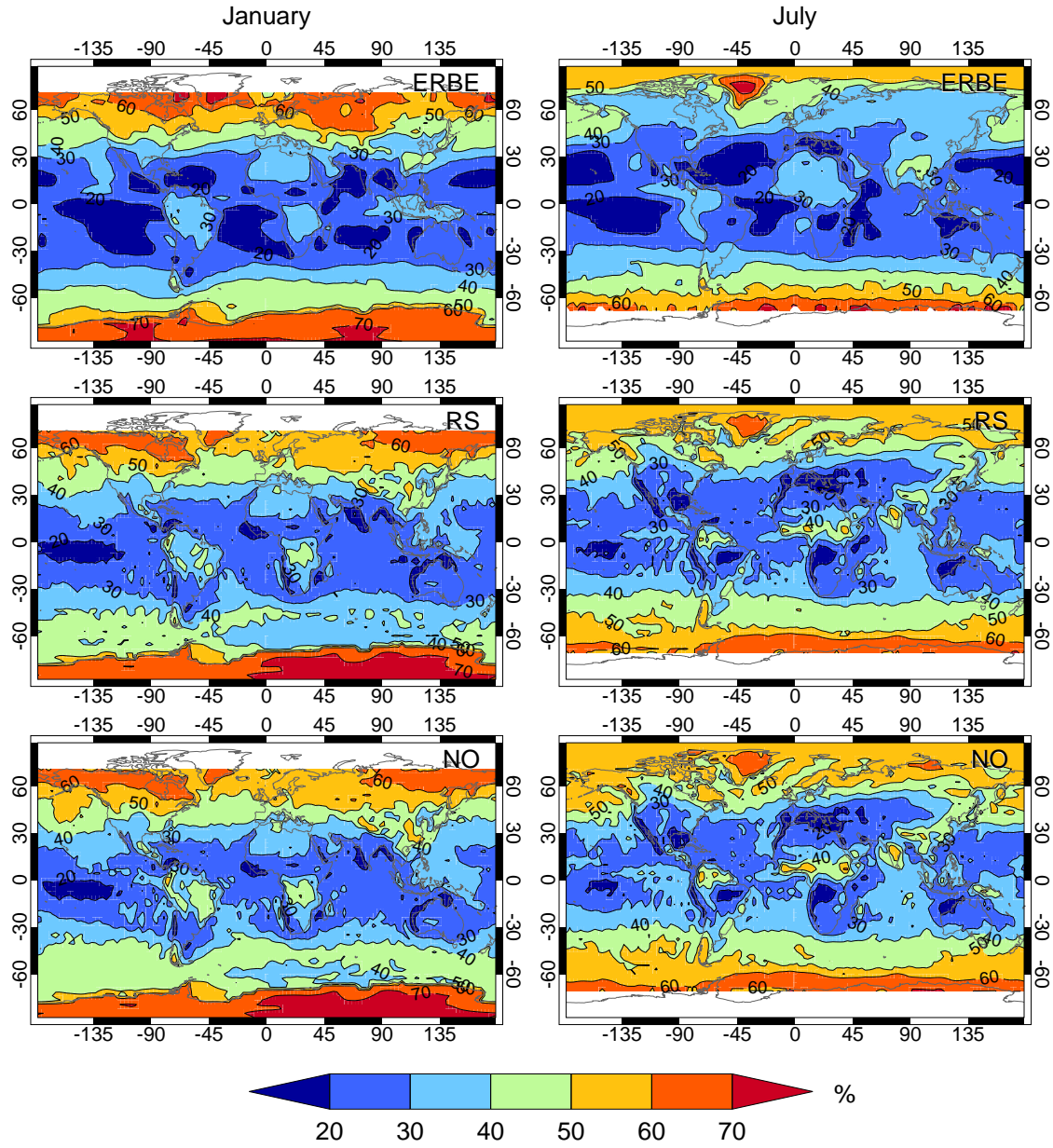
Figure 5.18: Albedo from ERBE (top), ECHAM5 RS (middle) and ECHAM5 NO (bottom) parameterization for January (left) and July (right).
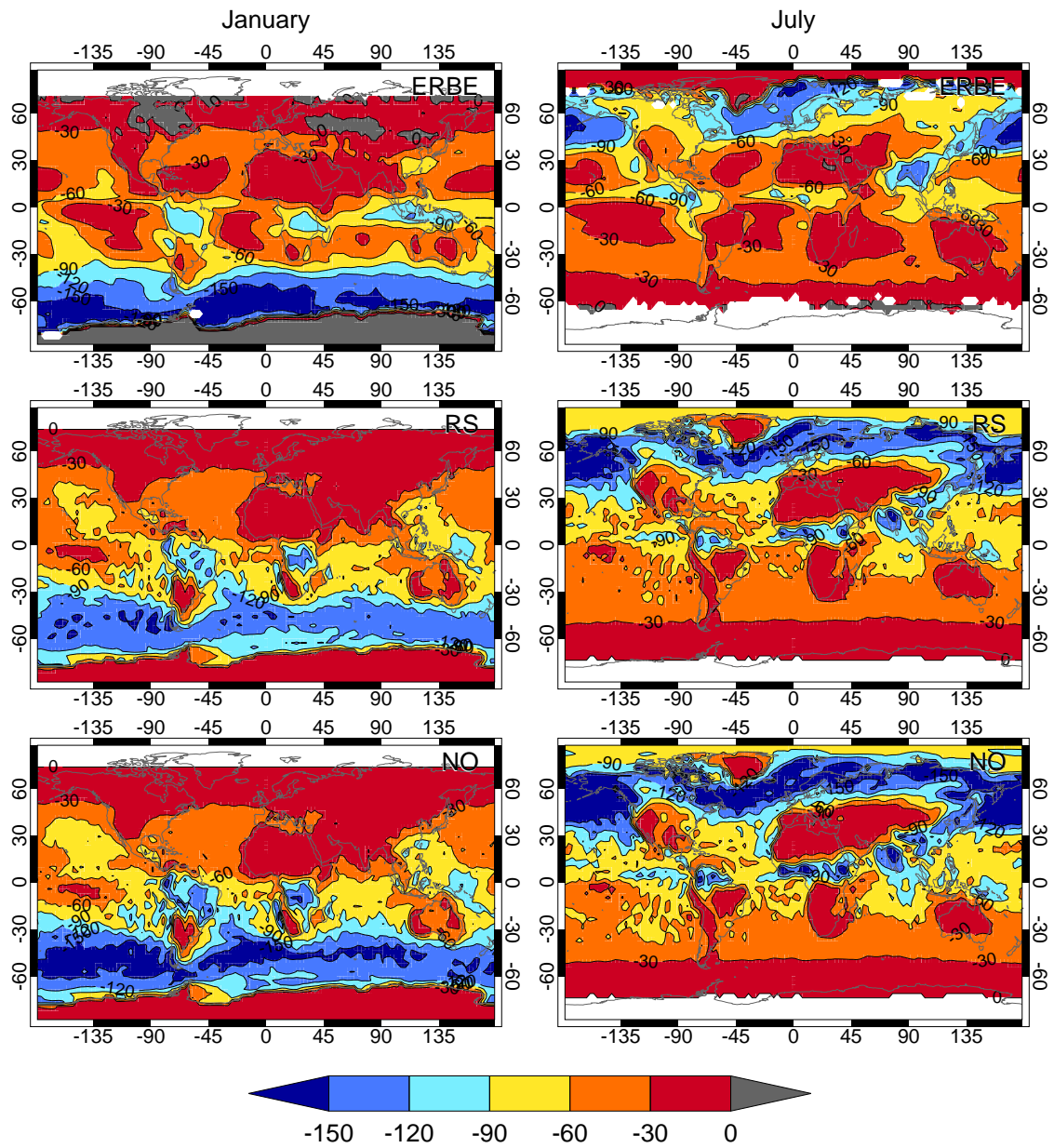
Figure 5.19: SW CRF from ERBE (top), ECHAM5 RS (middle) and ECHAM5 NO (bottom) parameterization for January (left) and July (right).

Chapter 6

Conclusions and Outlook

In this study the PPH-bias was investigated, i.e. the systematic error which is introduced by assuming clouds as plane parallel and homogenous layers in the radiative transfer computations. This work concentrated on the solar spectrum, for which albedo is overestimated, while transmittance is underestimated by the PPH approximation; systematic errors can also be expected for the longwave part (Fu et al., 2000a).

In the first part of this work the PPH-bias for two cloud simulations was calculated. For a homogenous nocturnal stratocumulus cloud, deviations of the PPH approximation from the reference computation, using the Independent Column Approximation, are relatively small ($< 5\%$ relative overestimation of albedo). Whereas, for a broken trade cumulus field this bias is substantial (up to 100% relative albedo error).

Two different approaches for correcting the PPH-bias were applied to the model clouds:

Effective Thickness Approach (ETA) In this approach an effective optical thickness is used for the radiative computation, reducing the true thickness by a factor χ. For overcast conditions the reduction factor may be deduced from the cloud variability. The latter is expressed as the mean logarithm of optical thickness. A value of $\chi = 0.9$ was calculated for the stratus clouds. However, this approach is not possible for broken clouds, where the thin cloud edges govern the mean logarithm. Instead, a reduction factor of $\chi = 0.4$ was deduced empirically for the trade wind cumuli. The second order effect of the solar zenith angle dependency of the reduction factor was not explicitly resolved, but an average angle of $45°$ was used.

Statistical Approach From the first and second moments of the distribution of cloud condensate a PDF can be constructed. In this approach the radiative fluxes are computed by weighting the two-stream results with this PDF. Different shapes have been proposed to describe the distribution, like Gamma- or Beta-distribution. For the cloud model data, the Gamma-distribution was chosen here, since it fits the data in the model's small domain better than the Beta distribution and enables

the use of the elaborate Gamma Weighted Two-Stream Approximation (GWTSA). In contrast to the findings from satellite measurements, the GWTSA fluxes did not resemble the ICA reference values precisely, but underestimated albedo, especially for cumulus clouds. This may have been due to misfits of the PDF to the original data. Nevertheless, the correction was of the right order of magnitude. Larger domain sizes are likely to reduce these misfits. Furthermore, the effect of correcting for correlation among the PDFs in adjacent layers was studied. In the highly vertically resolved model data the correction, when perfect correlation was assumed, further reduced albedo by nearly the same amount as the difference between the PPH and the uncorrected GWTSA. For climate models, with their relatively thick layers, this effect can be expected to be smaller. Relaxing the assumption of perfect correlation would further reduce the influence of the correlation correction.

The ETA offers an approach which is easy to implement into existing two-stream radiation schemes, as they are used in most climate models. If no information about sub-grid scale cloud variability can be derived, a constant reduction factor may be set, yielding the right correction on global scale, while locally the albedo is overestimated for inhomogeneous convective clouds and underestimated for homogenous stratus decks or cirrus. If apart from the mean cloud condensate amount also higher moments of the sub-grid scale distribution are prognosed by the climate model, a statistical approach like the GWTSA offers the possibility to treat inhomogeneities consistently within the model. No further tuning, like empirically deriving reduction factors, is necessary.

In the second part of this work various bias corrections were implemented into the ECHAM5 model: One statistical scheme, the Beta Weighted Two-Stream Approximation, and four variants of the Effective Thickness Approach. A single model simulation was performed with the original ECHAM5 code, using an ETA scheme, to force the model. The other schemes were run simultaneously, but produced only diagnostic output. Thus, the fluxes from all schemes were computed on the same model time-steps, all with the same input parameters from the General Circulation Model (GCM).

The ETA implementation using only a single, unique reduction factor of $\chi = 0.7$ showed seasonally averaged albedo corrections over 4% locally. The most striking were some patterns over the Pacific warm pool, which were almost identical to those of high ice amounts. Similar spatial and temporal distributions of albedo corrections were obtained for an ETA scheme, where different reduction factors were applied for clouds in GCM grid columns, where convection was active ($\chi_{conv} = 0.4$) or only stratiform clouds were present ($\chi_{strat} = 0.9$). In an accompanying experiment, the ETA with $\chi = 0.7$ was only applied to liquid water clouds, while ice clouds were left unchanged. The patterns with maximum albedo correction disappeared and could thus clearly be connected with ice clouds. Roeckner et al. (2003) accounted for these effects in the ETA as it is realized in the ECHAM5 standard model: liquid water clouds are scaled between 0.4 for thick and 1.0 for thin clouds, while for ice clouds $\chi = 0.9$ is used in accordance with Buschmann

(2001). Compared to the uncorrected PPH scheme, the albedo is globally reduced by 1.8% corresponding to $6\,\mathrm{Wm^{-2}}$ in the reflected flux.

The ECHAM5 model offers the opportunity to implement a statistical scheme consistently, since the cloud scheme prognoses the sub-grid scale variability as a Beta-distribution. Similar to the GWTSA, a Beta Weighted Two-Stream Approximation (BWTSA), weighting the two-stream radiative properties according to the Beta-shaped PDF, was added to the ECHAM5 model as part of this work. Compared to the uncorrected PPH scheme, the albedo reduces globally by 0.9%, corresponding to $3.1\,\mathrm{Wm^{-2}}$ less radiation reflected back to space. The albedo modification due to the BWTSA is highest in the stratocumulus regimes off the continental west coasts, reaching over 2% in the seasonal mean. While the general patterns are similar to the ECHAM5 standard ETA implementation, the amplitude is only roughly half. It has to be noted that cirrus clouds were not treated any special way, as in the standard ECHAM5 code. The albedo modification results solely from the weighting according to the Beta-distribution as prognosed by the cloud scheme. Accounting for the correlation effect would increase the albedo change, as was shown in the experiments using the cloud resolving model data.

In the comparison of the albedo and cloud radiative forcing from the miscellaneous radiation schemes to satellite measurements from the ERBE data set, it was shown that the deviation of the modeled fluxes from the measurements were larger than those between the different model schemes, with the PPH-bias corrected schemes being closer to the observation. This indicates that the uncertainty of the cloud microphysical parameterizations is dominating the radiative fluxes, while the PPH-bias is a second order effect. It also emphasizes the need for accurate and consistent radiation calculations: Lacking a precise global climatology of liquid and ice water amounts, cloud schemes are tuned such that the global radiative budget is balanced. Errors in the radiative fluxes can result from erroneous cloud parameterizations, but also from deficiencies in the parameterization of the cloud-radiation interactions. Removing an uncertainty in the radiation parameterization, like the PPH-bias, limits the possible sources for the flux discrepancies. Statistical schemes, which are consistently implemented in a model, reduce the number of tuning parameters (in contrast to the ETA scheme) and thus help to adjust the remaining constants in the cloud parameterizations.

For this study, a rather straightforward realization of the BWTSA was used, where no further approximations were added in order to unambiguously show the effect of accounting for the sub-grid scale variability of clouds consistently in the cloud scheme and radiation model. In future versions some computational optimizations and physical refinements could be included:

- Currently the weighted two-stream functions are numerically integrated by Gaussian quadrature. The shortwave radiation code has to be called several times, requiring additional computing time. The GWTSA on the other hand can be solved analytically with only a minor increase in compute cost. One could fit a Gamma-distribution

to the tail of the Beta-distribution that describes the condensate amount, and use that in the GWTSA algorithm. However, this would introduce some inconsistency through changing the distribution shape, and therefore one would first need to show that the general structure of the bias correction is preserved.

- The correlation correction becomes more important the higher the vertical resolution. Perfect correlation, as described in Section 3.2.1, might serve as a first approximation, but a more elaborate parameterization has to be worked out from cloud model simulations and observations, similar to the problem of cloud overlap (Hogan and Illingworth, 2001).

- Cloud variability is not only important for the solar part of the spectrum, although most studies have only dealt with this, but also for thermal radiation. A consistent treatment for both spectral intervals therefore is desirable. Currently the ECHAM5 standard radiation scheme applies the same reduction factors to the shortwave and longwave radiation computations, which is supported by findings of Rossow et al. (2002). However experiments like those presented in Chapter 4 need also to be performed for longwave radiation. Statistical schemes for thermal radiation already exist for the Gamma-distribution (Fu et al., 2000a), which could be adjusted to work with the Beta-distribution prognosed by the ECHAM5 cloud scheme.

- Satellite climatologies of cloud variability are needed on a global scale, in order to evaluate the model results. Rossow et al. (2002) started to create such data sets, but currently both horizontal and vertical inhomogeneity cannot be separated. So for the models to be compared to this data, the satellite measurements need to be simulated for the model atmosphere, including the prognosed cloud overlap and horizontal inhomogeneity. Satellites resolving the cloud vertical structure, like the planned CLOUDSAT mission (Stephens et al., 2000), could improve the validation substantially.

Bibliography

Arking, A., 1996. Absorption of solar energy in the atmosphere — discrepancy between model and observations. Science 273 (5276), 779–782.

Arking, A., Chou, M.-D., Ridgway, W. L., 1996. The accuracy of shortwave radiative transfer codes in climate models. In: Smith, W. L., Stammes, K. (Eds.), IRS '96: Current problems in atmospheric radiation. International Radiation Symposium, A. DEEPAK Publishing, Hampton, Virginia, USA, pp. 257–261.

Bakan, S., Quenzel, H., 1976. Path length distribution of photons scattered in turbid atmospheres. Beitr. Phys. Atmosph. 49, 272–284.

Barker, H. W., 1996. A parameterization for computing grid-averaged solar fluxes for inhomogeneous marine boundary layer clouds. Part I: Methodology and homogeneous biases. J. Atmos. Sci. 53 (16), 2289–2303.

Barker, H. W., 2000. Indirect aerosol forcing by homogeneous and inhomogeneous clouds. J. Climate 13 (11), 4042–4049.

Barker, H. W., Fu, Q., 1999. Modelling domain-averaged solar fluxes for an evolving tropical cloud system. Atmos. Oceanic Opt. 12 (3), 211–217.

Barker, H. W., Fu, Q., 2000. Assessment and optimization of the Gamma-weighted two-stream approximation. J. Atmos. Sci. 57 (8), 1181–1188.

Barker, H. W., Li, Z., 1997. Interpreting shortwave albedo-transmittance plots: True or apparent anomalous absorption? Geoph. Res. Lett. 24 (16), 2023–2026.

Barker, H. W., Marshak, A., Szyrmer, W., Blanchet, J.-P., Trishchenko, A., Li, Z., 2002. Inference of cloud optical depth from aircraft-based solar radiometric measurements. J. Atmos. Sci. 59 (13), 2093–2111.

Barker, H. W., Morcrette, J.-J., Alexander, G. D., 1998. Broadband solar fluxes and heating rates for atmospheres with 3D broken clouds. Quart. J. Roy. Meteorol. Soc. 124 (548 Part B), 1245–1271.

Barker, H. W., Stephens, G. L., Fu, Q., 1999. The sensitivity of domain-averaged solar fluxes to assumptions about cloud geometry. Quart. J. Roy. Meteorol. Soc. 125 (558), 2127–2152.

Barker, H. W., Wielicki, B. A., Parker, L., 1996. A parameterization for computing grid-averaged solar fluxes for inhomogeneous marine boundary layer clouds. Part II: Validation using satellite data. J. Atmos. Sci. 53 (16), 2304–2316.

Barkstrom, B. R., 1984. The Earth Radiation Budget Experiment (ERBE). Bull. Am. Meteorol. Soc. 65, 1170–1185.

Barrett, E. C., 1974. Climatology from Satellites. Methuen & Co. Ltd.

Bergman, J. W., Hendon, H. H., 1998. Calculating monthly radiative fluxes and heating rates from monthly cloud observations. J. Atmos. Sci. 55 (23), 3471–3491.

Brinkop, S., Roeckner, E., 1995. Sensitivity of a general circulation model to parameterizations of cloud-turbulence interactions in the atmospheric boundary layer. Tellus 47A, 197–220.

Bronstein, I. N., Semendjajew, K. A., 1991. Taschenbuch der Mathematik, 25th Edition. B. G. Teubner Verlagsgesellschaft.

Brümmer, B., Augstein, E., Riehl, H., 1974. Low-level wind structure in atlantic trade. Q. J. R. Meteorol. Soc. 100 (423), 109–121.

Buschmann, N., 2001. Inhomogenitäten in Cirren und ihre Auswirkungen auf den solaren Strahlungstransport. Berichte der GKSS 2001/22, GKSS-Forschungszentrum Geesthacht, GmbH, GKSS Forschungszentrum Geesthacht GmbH, Postfach 1160, 21494 Geesthacht, Germany, PhD thesis.

Byrne, R. N., Somerville, R. C. J., Subasilar, B., 1996. Broken-cloud enhancement of solar radiation absorption. J. Atmos. Sci. 53 (6), 878–86.

Cahalan, R. F., Ridgway, W., Wiscombe, W. J., Bell, T. L., Snider, J. B., 1994. The albedo of fractal stratocumulus clouds. J. Atmos. Sci. 51 (16), 2434–55.

Cahalan, R. F., Ridgway, W., Wiscombe, W. J., Gollmer, S., Harshvardhan, 1994. Independent pixel and monte carlo estimates of stratocumulus albedo. J. Atmos. Sci. 51 (24), 3776–90.

Cairns, B., Lacis, A. A., Carlson, B. E., 2000. Absorption within inhomogeneous clouds and its parameterization in general circulation models. J. Atmos. Sci. 57 (5), 700–14.

Cess, R. D., Zhang, M. H., Minnis, P., Corsetti, L., Dutton, E. G., Forgan, B. W., Garber, D. P., Gates, W. L., Hack, J. J., Harrison, E. F., Jing, X., Kiehl, J. T., Long, C. N., Morcrette, J.-J., Potter, G. L., Ramanathan, V., Subasilar, B., Whitlock, C. H., Young, D. F., Zhou, Y., 1995. Absorption of solar radiation by clouds: observations versus models. Science 267 (5197), 496–499.

Chambers, L. H., 1997. Computation of the effects of inhomogeneous clouds on retrieval of remotely sensed properties. In: Ninth Conference on Atmospheric Radiation. American Meteorological Society, pp. 378–82.

Chambers, L. H., Wielicki, B. A., Evans, K. F., 1997. Accuracy of the independent pixel approximation for satellite estimates of oceanic boundary layer cloud optical depth. J. Geophys. Res. 102 (D2), 1779–1794.

Chambers, L. H., Wielicki, B. A., Evans, K. F., 1997. Independent pixel and two-dimensional estimates of LANDSAT-derived cloud field albedo. J. Atmos. Sci. 54 (11), 1525–1532.

Chambers, L. H., Wielicki, B. A., Loeb, N. G., 2001. Shortwave flux from satellite-measured radiance: A theoretical study over marine boundary layer clouds. J. Appl. Meteorol. 40 (12), 2144–2161.

Chen, C.-T., Roeckner, E., 1996. Validation of the earth radiation budget as simulated by the Max Planck Institute for Meteorology general circulation model ECHAM4 using satellite observations of the Earth Radiation Budget Experiment. J. Geophys. Res. 101 (D2), 4269–4287.

Chlond, A., 1992. Three-dimensional simulation of cloud street development during a cold air outbreak. Boundary-Layer Meteorol. 58, 161–200.

Chlond, A., 1994. Locally modified version of Bott's advection scheme. Mon. Wea. Rev. 122, 111–125.

Chlond, A., Wolkau, A., 2000. Large-eddy simulation of a nocturnal strtocumulus-topped marine atmospheric boundary layer: an uncertainty analysis. Boundary-Layer Meteorol. 95, 31–55.

Chou, M.-D., Suarez, M. J., Ho, C.-H., Yan, M. M.-H., Lee, K.-T., 1998. Parametrizations for cloud overlapping and shortwave single-scattering properties for use in general circulation and cloud ensemble models. J. Climate 11 (2), 203–214.

Coakley Jr, J. A., Chylek, P., 1975. Two-stream approximation in radiative transfer: including the angle of the incident radiation. J. Atmos. Sci. 32 (2), 409–418.

Coley, P. F., Jonas, P. R., 1997. The contribution of cloud inhomogeneities and droplet concentration to the albedo of broken-cloud fields. Quart. J. Roy. Meteorol. Soc. 123 (543), 1931–1944.

Collins, W., 2001. Parameterization of generalized cloud overlap for radiative calculations in general circulation models. J. Atmos. Sci. 58 (21), 3224–3242.

Collins, W. D., 2001. Effects of enhanced shortwave absorption on coupled simulations of the tropical climate system. J. Climate 14 (6), 1147–1165.

Davis, A., Gabriel, P., Lovejoy, S., Schertzer, D., Austin, G. L., 1990. Discrete angle radiative-transfer. 3. Numerical results and meteorological applications. J. Geophys. Res.-Atmos. 95 (D8), 11729–11742.

de Roode, S. P., Duynkerke, P. G., 1997. Observed langrangian transition of stratocumulus into a cumulus during ASTEX: Mean state and turbulence structure. J. Atmos. Sci. 54, 2157–2173.

DKRZ, 1993. The ECHAM3 atmospheric general circulation model. Report 6, Deutsches Klimarechenzentrum, Bundesstr. 55, 20146 Hamburg, Germany.

Duda, D. P., Spinhirne, J. D., 1997. Near infrared and thermal infrared retrievals of cloud particle size in horizontally inhomogeneous clouds. In: Ninth Conference on Atmospheric Radiation. American Meteorological Society, pp. 436–440.

Duynkerke, P. G., Jonker, P. J., Chlond, A., van Zanten, M. C., Cuxart, J., Clark, P., Sanchez, E., Martin, G., Lenderink, G., Teixeira, J., 1999. Intercomparison of three- and one-dimensional model simulations and aircraft observations of stratocumulus. Boundary-Layer Meteorol. 92, 453–487.

Essenwanger, O., 1967. Applied Statistics in Atmospheric Sciences. Elsvier.

Evans, K. F., 1998. The spherical harmonics discrete ordinate method for three-dimensional atmospheric radiative transfer. J. Amtos. Ocean. Sci. 55 (3), 429–446.

Fouquart, Y., 1974. Utilisation des approximants de padé pour l'etude des largeurs équivalentes des raies formées en atmosphère diffusante. J. Quant. Spectrosc. Radiat. Transfer 14, 497–508.

Fouquart, Y., Bonnel, B., 1980. Computations of solar heating of the earth's atmosphere: A new parameterization. Contr. Atmos. Phys. 53 (1), 35–62.

Francis, P. N., Jones, A., Saunders, R. W., Shine, K. P., Slingo, A., Sun, Z., 1994. An observational and theoretical-study of the radiative properties of cirrus — some results from ICE89. Quart. J. Roy. Meteorol. Soc. 120 (518), 809–848.

Francis, P. N., Taylor, J. P., Hignett, P., Slingo, A., 1996. Measurements from the U.K. Meteorological Office C-130 aircraft relating to the question of enhanced absorption of solar radiation by clouds. In: Smith, W. L., Stammes, K. (Eds.), IRS '96: Current problems in atmospheric radiation. International Radiation Symposium, A. DEEPAK Publishing, Hampton, Virginia, USA, pp. 117–20.

Francis, P. N., Taylor, J. P., Hignett, P., Slingo, A., 1997. On the question of enhanced absorption of solar radiation by clouds. Quart. J. Roy. Meteorol. Soc. 123 (538 Part B), 419–434.

Fu, Q., Carlin, B., Mace, G., 2000a. Cirrus horizontal inhomogeneity and OLR bias. Geophys. Res. Lett. 27 (20), 3341–3344.

Fu, Q., Cribb, M. C., Barker, H. W., Krueger, S. K., Grossman, A., 2000b. Cloud geometry effects on atmospheric solar absorption. J. Atmos. Sci. 57 (8), 1156–1168.

Geleyn, J.-F., Hollingsworth, A., 1979. An economical analytical method for the computation of the interaction between scattering and line absorption of radiation. Beitr. Phys. Atmosph. 52, 1–16.

Goody, R. M., 1964. Atmospheric Radiation, I. Theoretical Basis. Clarendon Press.

Goody, R. M., Yung, Y. L., 1989. Atmospheric radiation. Oxford University Press.

Gregory, D., Morcrette, J.-J., Jakob, C., Beljaars, A., 1998. Introduction of revised radiation, convection, cloud and vertical diffusion schemes into Cy18r3 of the ECMWF integrated forecasting system. Technical Memomrandum 254, ECMWF, Shinfield Park, Reading, RG2 9AX, UK.

Hagemann, S., 2002. An improved land surface parameter dataset for global and regional climate models. Report 336, Max-Planck-Institut für Meteorologie, Bundesstr. 55, 20146 Hamburg, Germany.

Harshvardhan, Randall, D. A., 1985. The parameterization of radiation for numerical weather prediction and climate models — comment. Mon. Weather Rev. 113 (10), 1832–1833.

Hartmann, D. L., 1993. Radiative effects of clouds on earth's climate. In: Hobbs, P. V. (Ed.), Aerosol-Cloud-Climate Interactions. Vol. 54 of International Geophysics Series. Academic Press Inc., Ch. 6, pp. 151–173.

Hartmann, D. L., Feb 2002. Climate change — tropical surprises. Science 295 (5556), 811–812.

Hogan, R. J., Illingworth, A. J., 2001. Deriving cloud overlap statistics from radar. Internal Report 125, Met. Office Joint Center for Mesoscale Meteorology, Meteorology Building, University of Reading, P O Box 243, Reading, Bershire, RG6 6BB, UK.

Houghton, J. T., Filho, L. G. M., Callander, B. A., N. Harris, A. K., Maskell, K. (Eds.), 1996. Climate Change 1995 — The Science of Climate Change: Contribution of Working Group I to the Second Assesment Report of the Intergovermental Panel on Climate Change. Cambridge University Press.

Houze, R. A., 1993. Cloud Dynamics. Vol. 53 of International Geophysics Series. Academic Press Inc.

Imre, D. G., Abramson, E. H., Daum, P. H., 1996. Quantifying cloud-induced shortwave absorption: an examination of uncertainties and of recent arguments for large excess absorption. J. Appl. Meteor. 35 (11), 1991–2010.

Jensen, J. L. W. V., 1906. Sur les fonctions convexes et les inégalitiés entre les valeurs moyennes. Acta Math. 30, 175–193.

Johnson, D. W., 1993. Parameterization of the cloud topped boundary layer: Aircraft measurements. In: ECMWF Workshop Proceedings 'Parameterization of the cloud topped boundary layer',Reading. pp. 77–117.

Johnson, N. L., Kotz, S., 1970. Continuous Univariate Distributions—2. John Wiley and Sons.

Joseph, J. H., Wiscombe, W. J., Weinman, J. A., 1976. Delta-Eddington approximation for radiative flux transfer. J. Atmos. Sci. 33 (12), 2452–2459.

Kato, S., Smith, G. L., Barker, H. W., 2001. Gamma-weighted discrete ordinate two-stream approximation for computation of domain-averaged solar irradiance. J. Atmos. Sci. 58 (24), 3797–3803.

Kiehl, J., 1994. On the observed near cancellation between longwave and shortwave cloud forcing in tropical regions. J. Clim. 7 (4), 559–565.

Kiehl, J., Trenberth, K., 1997. Earth's annual global mean energy budget. Bull. Amer. Meteorol. Soc. 78 (2), 197–208.

King, M. D., Harshvardhan, 1986. Comparative accuracy of selected multiple-scattering approximations. J. Atmos. Sci. 43 (8), 784–801.

Kinne, S., 1996. The 30-stream method — a discrete angle radiative transfer method for anisotropic scattering in inhomogeneous media. In: Smith, W. L., Stammes, K. (Eds.), IRS '96: Current problems in atmospheric radiation. International Radiation Symposium, A. DEEPAK Publishing, Hampton, Virginia, USA, pp. 135–138.

Kogan, Z. N., Lilly, D. K., Kogan, Y. L., Filyushkin, V., 1995. Evaluation of radiative parameterizations using an explicit cloud microphysical model. Atmos. Res. 35 (2–4), 157–172.

Kondratyev, K. Y., Binenko, V. I., Melnikova, I. N., 1998. Absorption of solar radiation by clouds and aerosols in the visible wavelength region. Meteorol. Atmos. Phys. 65, 1–10.

Lenoble, J., 1985. Radiative transfer in scattering and absorbing atmospheres: standard computational procedures. Geophysical Optics and Remote Sensing. A. Deepak Publishing, Hampton, Virginia USA.

Levkov, L., Rockel, B., Schiller, H., Kornblueh, L., 1998. 3-D simulation of clouds with subgrid fluctuations of temperature and humidity. Atmos. Res. 48, 327–341.

Li, J., Fu, Q., 2000. Absorption approximation with scattering effect for infrared radiation. J. Atmos. Sci. 57 (17), 2905–2914.

Li, Z., 1997. Inference of the impact of absorbing aerosols on the studies of ssrb retrieval and cloud absorption anomaly. In: Ninth Conference on Atmospheric Radiation. American Meteorological Society, pp. 41–44.

Li, Z., Moreau, L., Arking, A., 1998. On solar energy disposition: a perspective from observation and modeling. Bull. Am. Meteorol. Soc. 78 (1), 53–70.

Lin, S., Rood, R., 1996. Multidimensional flux-form semi-lagrangian transport schemes. Mon. Weather Rev. 124 (9), 2046–2070.

Lindzen, R., Chou, M., Hou, A., 2001. Does the earth have an adaptive infrared iris? Bull. Amer. Meteorol. Soc. 82 (3), 417–432.

Liou, K.-N., 1980. An introduction to atmospheric radiation. Academic Press, New York.

Liou, K. N., Rao, N., 1996. Radiative transfer in cirrus clouds. Part IV: On the cloud geometry, inhomogeneity, and absorption. J. Atmos. Sci. 53 (21), 3046–65.

Lohmann, U., 1996. Sensitivität des Modellklimas eines globalen Zirkulationsmodells der Atmosphäre gegenüber Änderungen der Wolkenmikrophysik. Examensarbeit 41, Max-Planck-Institut für Meteorologie, Bundesstr. 55, 20146 Hamburg, Germany, PhD thesis.

Lohmann, U., Roeckner, E., 1996. Design and performance of a new cloud microphysics scheme developed for the ECHAM general circulation model. Clim. Dyn. 12, 557–72.

Los, A., Duynkerke, P. G., 2000. Microphysical and radiative properties of inhomogenous stratocumulus: observations and model simulations. Quart. J. Roy. Meteorol. Soc. 126 (570 Part B), 3287–3307.

Lott, F., Miller, M., 1997. A new subgrid-scale orographic drag parametrization: Its formulation and testing. Q. J. R. Meteorol. Soc. 123 (537), 101–127.

Macke, A., Miller, J., Raschke, E., 1996. Single scattering properties of atmospheric ice crystals. J. Atmos. Sci. 53, 2813–2825.

Marshak, A., Davis, A., Cahalan, R., Wiscombe, W., 1996. The "nonlocal independent pixel approximation" for computing radiation fields of inhomogeneous clouds. In: Smith, W. L., Stammes, K. (Eds.), IRS '96: current problems in atmospheric radiation. International Radiation Symposium, A. DEEPAK Publishing, Hampton, Virginia, USA, pp. 139–42.

Marshak, A., Davis, A., Wiscombe, W., Cahalan, R., 1997. Inhomogeneity effects on cloud shortwave absorption measurements: two-aircraft simulations. J. Geophys. Res. 102 (D14), 16619–16637.

Marshak, A., Davis, A., Wiscombe, W., Ridgway, W., Cahalan, R., 1998. Biases in shortwave column absorption in the presence of fractal clouds. J. Climate 11 (3), 431–446.

Marshak, A., Davis, A., Wiscombe, W., Titov, G., 1995. The verisimilitude of the independent pixel approximation used in cloud remote sensing. Remote Sens. Environ. 52 (1), 71–78.

Mayer, B., 1999. I3RC phase 1 results from the MYSTIC Monte Carlo model. In: I3RC workshop. Tuscon, Arizona.

McFarlane, N. A., Boer, G. J., Blanchet, J.-P., Lazare, M., 1992. The canadia climate centre second-generation general circulation model and its equilibrium climate. J. Climate 44, 1775–1800.

Meador, W. E., Weaver, W. R., 1980. Two-stream approximations to radiative transfer in planetary atmospheres: a unified description of existing methods and a new improvement. J. Atmos. Sci. 37 (3), 630–643.

Minnis, P., Heck, P. W., Young, D. F., Fairall, C. W., Snider, J. B., 1992. Stratocumulus cloud properties derived from simultaneous satellite and island-based instrumentation during FIRE. J. Appl. Meteorol. 31 (4), 317–339.

Mlawer, E., Taubman, S., Brown, P., Iacono, M., Clough, S., 1997. Radiative transfer for inhomogeneous atmospheres: RRTM, a validated correlated-k model for the longwave. J. Geophys. Res.-Atmos. 102 (D14), 16663–16682.

Morcrette, J.-J., 1989a. Description of the radiation model in the ECMWF model. Technical Memorandum 165, ECMWF, Shinfield Park, Reading, RG2 9AX, UK.

Morcrette, J.-J., 1989b. Impact of changes to the radiation scheme in the ECMWF model. Technical Report 64, ECMWF, Shinfield Park, Reading, RG2 9AX, UK.

Morcrette, J.-J., 1991. Radiation and cloud radiative properties in the European Centre for Medium Range Weather Forecasts forecasting system. J. Geophys. Res. 96 (D5), 9121–9132.

Morcrette, J.-J., Jakob, C., 2000. The response of the ECMWF model to changes in the cloud overlap assumption. Mon. Weather Rev. 128 (6), 1707–1732.

Müller, G., Chlond, A., 1996. Three-dimensional numerical study of cell broadening during cold-air outbreaks. Boundary-Layer Meteorol. 81, 289–323.

Nordeng, T.-E., 1994. Extended versions of the convective parametrization scheme at ECMWF and their impact on the mean and transient activity of the model in the tropics. Technical Memorandum 206, ECMWF, Shinfield Park, Reading, RG2 9AX, UK.

O'Hirok, W., Gautier, C., 1997. Spectral aspects of three-dimensional atmospheric absorption. In: Ninth Conference on Atmospheric Radiation. American Meteorological Society, pp. 19–21.

O'Hirok, W., Gautier, C., 1998. A three-dimensional radiative transfer model to investigate the solar radiation within a cloudy atmosphere. Part I: Spatial effects. J. Atmos. Sci. 55 (12), 2162–2179.

Oreopoulos, L., Barker, H. W., 1999. Accounting for subgrid-scale cloud variability in a multi-layer 1D solar radiative transfer algorithm. Quart. J. Roy. Meteorol. Soc. 125 (553 Part A), 301–330.

Oreopoulos, L., Davies, R., 1998a. Plane parallel albedo biases from satellite observations. Part I: Dependence on resolution and other factors. J. Climate 11 (5), 919–932.

Oreopoulos, L., Davies, R., 1998b. Plane parallel albedo biases from satellite observations. Part II: Parametrizations for bias removal. J. Climate 11 (5), 933–944.

Petch, J. C., Cusack, S., Edwards, J. M., 1999. Off-line radiation calculations using an LEM simulation of TOGA-COARE. Part 2: Investigations of cloud water and ice inhomogeneities. Met O (APR) Turbulence and Diffusion Note 257, Met. Office, London Road, Bracknell, Berks, RG12 2SZ, UK.

Petch, J. C., Edwards, J. M., 1999. Off-line radiation calculations using an LEM simulation of TOGA-COARE. Part 1: Investigation of the cloud overlap assumption in the UM. Met O (APR) Turbulence and Diffusion Note 254, Met. Office, London Road, Bracknell, Berks, RG12 2SZ, UK.

Pilewskie, P., Valero, F. P. J., 1995. Direct observations of excess solar absorption by clouds. Science 267 (5204), 1626–1629.

Pincus, R., Klein, S. A., 2000. Unresolved spatial variability and microphysical process rates in large-scale models. J. Geophys. Res. 105 (D22), 27059–27065.

Pincus, R., McFarlane, S. A., Klein, S. A., 1999. Albedo bias and the horizontal variability of clouds in subtropical marine boundary layers: Observations from ships and satellites. J. Geophys. Res.-Atmos. 104 (D6), 6183–6191.

Podgorny, I. A., Vogelmann, A. M., Ramanathan, V., 1998. Effects of cloud shape and water vapor distribution on solar absorption in the near infrared. Geophys. Res. Lett. 25 (11), 1899–1902.

Ramanathan, V., 1987. The role of earth radiation budget studies in climate and general circulation research. J. Geophys. Res. 92, 4075–4095.

Ramanathan, V., Cess, R. D., Harrison, E. F., Minnis, P., Barkstrom, B. R., Ahmad, E., Hartmann, D., 1989. Cloud-radiative forcing and climate: Insights from the Earth Radiation Budget Experiment. Science 243, 57–63.

Ramanathan, V., Subasilar, B., Zhang, G. J., Conant, W., Cess, R. D., Kiehl, J. T., Graßl, H., Shi, L., 1995. Warm pool heat budget and shortwave cloud forcing: A missing physics? Science 267 (5197), 499–503.

Rockel, B., Raschke, E., Weyres, B., 1991. A parameterization of broad band radiative transfer properties of water, ice, and mixed clouds. Beitr. Phys. Atmosph. 42, 1–12.

Roeckner, E., 1995. Parameterization of cloud-radiative properties in the ECHAM4 model. In: Proceedings of the WCRP Workshop on "Cloud Microphysics Parameterizations in Global Atmospheric Circulation Models, May 23–25, 1995, Kananaskis, Alberta, Canada. Vol. 90 of WCRP-Report. pp. 105–116.

Roeckner, E., Arpe, K., Bengtsson, L., Brinkop, S., Dümenil, L., Esch, M., Kirk, E., Lunkeit, F., Ponater, M., Rockel, B., Sausen, R., Schlese, U., Schubert, S., Windelband, M., 1992. Simulation of the present-day climate with the ECHAM model: Impact of model physics and resolution. Report 93, Max-Planck-Institut für Meteorologie, Bundesstr. 55, 20146 Hamburg, Germany.

Roeckner, E., Arpe, K., Bengtsson, L., Christoph, M., Claussen, M., Dümenil, L., Esch, M., Giorgetta, M., Schlese, U., Schulzweida, U., Schlese, U., 1996. The atmospheric general circulation model ECHAM-4: Model description and simulation of present-day climate. Report 213, Max-Planck-Institut für Meteorologie, Bundesstr. 55, 20146 Hamburg, Germany.

Roeckner, E., Bäuml, G., Brokopf, R., Esch, M., Giorgetta, M., Hagemann, S., Kirchner, I., Kornblueh, L., Manzini, E., Rhodin, A., Schlese, U., Schulzweida, U., Tompkins, A., 2003. MPI-ECHAM5: Resolution dependence of systematic errors. In: Research Activities in Atmospheric and Oceanic Modelling. WGNE Report. WMO, to be published.

Rossow, W., Zhang, Y., 1995. Calculation of surface and top of atmosphere radiative fluxes from physical quantities based on ISCCP data sets — 2. validation and first results. J. Geophys. Res.-Atmos. 100 (D1), 1167–1197.

Rossow, W. B., Delo, C., Cairns, B., 2002. Implications of the observed mesoscale variations of clouds for the earth's radiation budget. J. Clim. 15 (6), 557–585.

Scheirer, R., 2000. GRIMALDI User Manual, Version 0.9. Institut für Meereskunde, Universität Kiel, Düsternbrooker Weg 20, 24105 Kiel, Germany.

Scheirer, R., 2001. Solarer Strahlungstransport in der inhomogenen Atmosphäre. Berichte aus dem Institut für Meereskunde an der Christian-Albrechts-Universität Kiel 332, Christian-Albrechts-Universität Kiel, Düsternbrooker Weg 20, 24105 Kiel, Germany, PhD thesis.

Scheirer, R., Macke, A., 2002. Cloud-inhomogeneity and broadband solar fluxes. J. Geophys. Res. submitted.

Schulz, J., 1998. On the effect of cloud inhomogeneity an area averaged radiative properties of contrails. Geophys. Res. Lett. 25 (9), 1427–1430.

Stamnes, K., Swanson, R. A., 1981. A new look at the discrete ordinate method for radiative- transfer calculations in anisotropically scattering atmospheres. J. Atmos. Sci. 38 (2), 387–399.

Stephens, G. L., 1985. The parameterization of radiation for numerical weather prediction and climate models — reply. Mon. Weather Rev. 113 (10), 1834–1835.

Stephens, G. L., 1988a. Radiative-transfer through arbitrarily shaped optical media. Part I: A general method of solution. J. Atmos. Sci. 45 (12), 1818–1836.

Stephens, G. L., 1988b. Radiative-transfer through arbitrarily shaped optical media. Part II: Group-theory and simple closures. J. Atmos. Sci. 45 (12), 1837–1848.

Stephens, G. L., Gabriel, P. M., Tsay, S.-C., 1991. Statistical radiative transport in one-dimensional media and its application to the terrestrial atmosphere. Trans. Theor. Stat. Phys. 20 (2&3), 139–175.

Stephens, G. L., Tsay, S.-C., 1990. On the cloud absorption anomaly. Quart. J. Roy. Meteorol. Soc. 116 (493), 671–704.

Stephens, G. L., Vane, D. G., Walter, S. J., 2000. The CLOUDSAT mission: a new dimension to space-based observations of cloud in the coming millenium. In: Workshop on cloud processes and cloud feedbacks in large-scale models. Vol. 110 of World Climate Research Programme. World Meteorological Organization, pp. 143–160.

Stevens, B., Ackerman, A. S., Albrecht, B. A., Brown, A. R., Chlond, A., Cuxart, J., Duynkerke, P. G., Lewellen, D. C., Macvean, M. K., Neggers, R. A. J., Sànchez, E., Siebesma, A. P., Stevens, D. E., 2001. Simulations of trade wind cumuli under a strong inversion. J. Atmos. Sci. 58 (14), 1870–1891.

Sundqvist, H., 1978. Parameterization scheme for nonconvective condensation, including prediction of cloud water content. Quart. J. Roy. Meteorol. Soc. 104 (441), 677–90.

Szczap, F., Isaka, H., Saute, M., Guillemet, B., Gour, Y., 2000a. Inhomogeneity effects of 1D and 2D bounded cascade model clouds on their effective radiative properties. Phys. Chem. Earth (B) 25 (2), 83–89.

Szczap, F., Isaka, H., Saute, M., Guillemet, B., Ioltukhovski, A., 2000b. Effective radiative properties of bounded cascade absorbing clouds: Definition of an effective single-scattering albedo. J. Geophys. Res.-Atmos. 105 (D16), 20635–20648.

Szczap, F., Isaka, H., Saute, M., Guillemet, B., Ioltukhovski, A., 2000c. Effective radiative properties of bounded cascade nonabsorbing clouds: Definition of the equivalent homogeneous cloud approximation. J. Geophys. Res.-Atmos. 105 (D16), 20617–20633.

Tiedtke, M., 1989. A comprehensive mass flux scheme for cumulus parameterization in large-scale models. Mon. Weather Rev. 117 (8), 1779–1800.

Tiedtke, M., 1993. Representation of clouds in large-scale models. Mon. Weather Rev. 121 (11), 3040–3061.

Tiedtke, M., 1996. An extension of cloud-radiation parameterization in the ECMWF model: The representation of subgrid-scale variations of optical depth. Mon. Wea. Rev. 124 (4), 745–750.

Titov, G. A., Kasjanov, E. I., 1996. Radiative effects of inhomogeneous stratocumulus clouds. In: Smith, W. L., Stammes, K. (Eds.), IRS '96: Current problems in atmospheric radiation. International Radiation Symposium, A. DEEPAK Publishing, Hampton, Virginia, USA, pp. 78–81.

Titov, G. A., Zhuravleva, T. B., Zuev, V. E., 1997. Mean radiation fluxes in the near-IR spectral range: algorithms for calculation. J. Geophys. Res. 102 (D2), 1819–1832.

Tompkins, A. M., 2002. A prognostic parameterization for the subgrid-scale variability of water vapor and clouds in large-scale models and its use to diagnose cloud cover. J. Atmos. Sci. 59 (12), 1917–1942.

Várnai, T., 2000. Influence of three-dimensional radiative effects on the spatial distribution of shortwave cloud reflection. J. Atmos. Sci. 57 (2), 216–229.

Várnai, T., Davies, R., 1996. Quantitative analysis of radiative inhomogeneity effects. In: Smith, W. L., Stammes, K. (Eds.), IRS '96: Current problems in atmospheric radiation. International Radiation Symposium, A. DEEPAK Publishing, Hampton, Virginia, USA, pp. 155–8.

von Bremen, L., 2001. Mikrowellenfernerkundung bei inhomogener Bewölkung. Berichte aus dem Institut für Meereskunde an der Christian-Albrechts-Universität Kiel 321, Christian-Albrechts-Universität Kiel, Düsternbrooker Weg 20, 24105 Kiel, Germany, PhD thesis.

Wang, J. H., Rossow, W. B., Zhang, Y. C., 2000. Cloud vertical structure and its variations from a 20-yr global rawinsonde dataset. J. Clim. 13 (17), 3041–3056.

Wielicki, B. A., Wong, T., Allan, R. P., Slingo, A., Kiehl, J. T., Soden, B. J., Gordon, C. T., Miller, A. J., Yang, S.-K., Randall, D. A., Robertson, F., Susskind, J., Jacobowitz, H., Feb 2002. Evidence for large decadal variability in the tropical mean radiative energy budget. Science 295 (5556), 841–844.

Wild, M., Ohmura, A., Cubasch, U., 1997. GCM-simulated surface energy fluxes in climate change experiments. J. Climate 10 (12), 3093–3110.

Wilks, D. S., Mar 1995. Statistical Methods in the Atmospheric Sciences. Academic Press.

Wiscombe, W. J., Welch, R. M., Hall, W. D., 1984. The effects of very large drops on cloud absorption. J. Atmos. Sci. 41, 1336–1355.

Zdunkowski, W. G., Korb, G., 1974. An approximative method for the determination of short-wave radiative fluxes in scattering and absorbing media. Contrib. Atmos. Phys. 47, 129–144.

Zuidema, P., Evans, K. F., 1998. On the validity of the independent pixel approximation for boundary layer clouds observed during ASTEX. J. Geoph. Res. 103 (D6), 6059–6074.

Danksagung

Das Wettergeschehen ist ein chaotisches Phänomen. Der berühmte Flügelschlag eines Schmetterlings, der einen Hurrkian auslöst, möge als Beispiel dienen. Dabei ist zu vermuten, dass dem Schmetterling die Auswirkung seiner Tat gar nicht unmittelbar bewusst ist und ihn somit keine direkte Schuld an den Verwüstungen des Wirbelsturms trifft. Um niemanden zu kompromittieren verwahre ich mich davor, die unvorhersagbare Natur des Wetters auf die Menschheit im allgemeinen zu übertragen, sondern beschränke mich hier auf mich und die vorliegende Arbeit. Viele Menschen waren — ihres Tuns mehr oder minder bewusst — gleich insektischen Großflüglern und ihre Aktivitäten verursachten vermittels meiner chaotischen Denkprozesse schließlich den als Dissertation betitelten Prozess.

Da sei zuerst mein Betreuer Erich Roeckner genannt, der Licht (genauer: solare Strahlung) in das Dunkel meiner Promotionsgedanken brachte und mir große Freiheiten beim Erhellen der inhomogenen Wolken gewährte. Für die stete Bereitschaft, mit mir über meine neuesten Geistesblitze zu diskutieren und mich in die Geheimnisse der Klimasimulation einzuweihen gilt ihm mein herzlicher Dank.

Prof. Graßl erklärte sich sofort bereit, als Gutachter zu fungieren. Für das Interesse, das er meiner Arbeit entgegenbrachte, mein Dank. Ebenso an die weiteren Mitglieder des Promotionsausschusses, Prof. Zahel, Frank Lunkeit und Andreas Macke. An letzteren ein besonderer Dank für die zahlreichen Diskussionen und Einladungen nach Kiel im Laufe meiner Promotion. Seine aufmunternden Worte ließen mich immer wieder daran glauben, dass auch *meine* Dissertation noch zu einem guten Ende kommen wird.

Was auf den vorhergehenden Seiten würde übrig bleiben ohne die Daten von Andreas Chlond und das Bedeckungsgradschema von Adrian Tompkins? Antwort: Einleitung, Theorie und Danksagung. Beiden meinen aufrichtigen Dank für die Unterstützung und die (zumindest nach aussen gezeigte) Ruhe, mit der sie mir meteorologisch Unbedarftem die flacheren und tieferen Einblicke in die Welt der Wolken erklärten. Marco Giorgetta und Stephan Bakan mühten sich redlich damit ab, mir die Grundlagen der Strahlungsberechnung nahe zu bringen.

MPI-Examensarbeit-Referenz:

Examensarbeit Nr. 1-67 bei Bedarf bitte Anfragen:
MPI für Meteorologie, Abtlg.: PR, Bundesstr. 55, 20146 Hamburg

Examensarbeit Nr. 68 Februar 2000	**Die direkte Strahlungswirkung von Aerosolteilchen auf ein Klimamodell** Anke Maria Allner
Examensarbeit Nr. 69 Februar 2000	**Räumliche und zeitliche Variabilität von Wasserisotopen im polaren Niederschlag** (Spatial and Temporal Variability of Water Isotopes in Polar Precipitation) Martin Werner
Examensarbeit Nr. 70 März 2000	**Bestimmung des turbulenten Impulsflusses mit Hilfe von Doppler- und Interferometriemessungen eines Radar-RASS-Systems** Lutz Hirsch
Examensarbeit Nr. 71 Mai 2000	**Entwicklung und Test eines massenerhaltenden semi-Lagrangschen Transportverfahrens auf einer Kugel** Markus Peter Olk
Examensarbeit Nr. 72 Mai 2000	**Quantification of Natural Climate Variability in Paleoclimatic Proxy Data Using General Circulation Models: Application to Glacier Systems** Bernhard K. Reichert
Examensarbeit Nr. 73 Mai 2000	**Validation of Clouds in the ECHAM4 Model Using a Dynamical Adjustment Technique** Hans-Stefan Bauer
Examensarbeit Nr. 74 Juni 2000	**The Dynamical Link Between the Troposphere and Stratosphere and its Potential to Affect Climate** Judith Perlwitz
Examensarbeit Nr. 75 Juli 2000	**Fernerkundung von Eis- und Mehrschichtbewölkung über Meeresuntergrund aus Messungen rückgestreuter Solarstrahlung** Claudio Costanzo
Examensarbeit Nr. 76 Juli 2000	**Large-scale SST variability in the midlatitudes and in the tropical Atlantic** Dietmar Dommenget
Examensarbeit Nr. 77 Juli 2000	**HOAPS: Eine neue Klimatologie des Süßwasserflusses an der Meeresoberfläche abgeleitet aus Satellitendaten** Volker Jost
Examensarbeit Nr. 78 September 2000	**The potential influence of natural climate variability and uncertainty in the design of optimal greenhouse gas emission policies** Victor Ocaña